© 2008 Mengning Liang

X-RAY DIFFRACTION ROTATIONAL MICRORHEOLOGY

BY

MENGNING LIANG

B.S., North Carolina State University, 2002
M.S., University of Illinois at Urbana-Champaign, 2004

DISSERTATION

Submitted in partial fulfillment of the requirements
for the degree of Doctor of Philosophy in physics
in the Graduate College of the
University of Illinois at Urbana-Champaign, 2008

Urbana, Illinois

Abstract

insert abstract here

to mom

Acknowledgments

people

Table of Contents

1

Chapter 1

Introduction

1.1 Microrheology

Rheology is the study of the response of matter under an applied stress. There are two mechanisms by which a material responds to an applied stress: an elastic response which stores energy in a spring like manner, or a viscous response which leads to dissipation in the system [1]. Simple solids respond elastically, storing elastic free energy as strain in the material. Simple fluids have a dissipative, viscous response which may be described by the dissipative generalization of Euler's equation [2] which incorporates entropy production into the conservation equations which describe the hydrodynamics of simple, one-component fluids. More complex, viscoelastic materials have both an elastic and viscous response which depends on the timescale or frequency of the applied stress.

Traditionally, the shear viscosity is measured with a mechanical rheometer which applies a shear strain to the material at a set frequency, up to the tens of Hertz and measures the resultant stress. At higher frequencies, inertial effects, which cause the shear wave to decay before it can propagate into the entire sample, must be considered and the viscosity can no longer be simply determined. Traditional rheology has limitations due to the need for relatively large quantities of sample which may be difficult to obtain for scarce samples. It also probes the bulk shear response and cannot comprehensively describe fluids which are heterogeneous and which contain microstructure.

More recently, microrheology, which measures the shear response with an embedded, micron sized particle, has transcended some of these limitations. [3] [4] Since microrheology

does not require shear standing waves which extend to the bulk, it can theoretically extend the range accessible frequencies to the MHz regime. By quantifying the particle behavior of an embedded particle with a known external force and taking into account the particle-liquid coupling, one can extract the properties of the media itself. The embedded particle must have some measurable driving force with which to interact with the media and the nature of this driving force segregates microrheology into two types.

One type is active microrheology in which the particle is externally driven by a force such as an electric or magnetic field or micromechanical forces. This method is particularly useful for highly viscous materials in which large forces are required to obtain a measurable response. The other is passive microrheology where the driving force is the thermal energy k_BT which is already in the system. The earliest example of such an experiment was Robert Brown's observation of pollen molecules undergoing the random motion which now bears his name. Einstein's interpretation of the experiment which relates the thermal motion to the viscosity of the material via the diffusion constant is the first and simplest example of passive microrheology.

1.2 Complex fluids

Complex fluids include many types of fluids which have interesting and unique behaviors such as colloidal suspensions, micellar solutions, emulsions and other types of soft materials. Far from being esoteric, complex fluids are an integral part of daily life. The majority of biological and geological fluids are colloidal suspensions of which blood, milk, mud and cell cytoplasm are just a few examples. Micellar structures are used to tune the properties of surfactants and lubricants in many commercial products such as personal care products.

The common theme of all these materials, and thus the defining characteristic of a complex fluid is the presence of a mesoscopic length scale which determines the properties of the material.[5] This intermediate length scale between the microscopic constituents and the

macroscopic bulk is typically between the tens of nanometers and microns. These length scales are the characteristic sizes of the colloids, the length or diameter of the micelles and the pore size in emulsions and foams. Complex fluids almost always have complex, nonlinear rheological behavior due to this intermediate length scale because the torques on these intermediate sized constituents are large.

Viscoelastic fluids are a subset of complex fluids and much of the theory was developed to understand the physical properties of polymers which, like solids completely recover from an applied stress but creep under the application of a continuous stress [7] They cannot be described by the direct stress-strain relationship of a solid or the hydrodynamic, viscous response of a fluid. Viscoelastic fluids can be described by some intuitive models which illustrate the time dependence of the relaxation behavior which has components of both types of response. The models are analagous to electrical circuit components of capacitance which is elastic in character and resistance, which is dissipative. The storage response which manifests itself as a reversible strain γ due to a stress σ in a material can be modeled as a Hookean spring where the spring constant J is analogous to the Young's modulus, thus a constant strain produces a constant stress.

$$\gamma = \sigma J \tag{1.1}$$

The viscous response is modeled as a Newtonian dashpot which depends not the strain but the strain rate of the material. The constant of proportionality is the viscosity of the material and this model describes a system where a constant strain rate produces a constant stress.

$$\sigma = \nu \frac{d\gamma}{dt} \tag{1.2}$$

The ratio of viscosity to modulus gives a time τ which describes the relaxation rate. Putting these two descriptions together, one can produce a model which describes physical

Figure 1.1: Maxwell model

systems with various characteristics.

The simplest is the Maxwell model which describes the fluid with dashpot and spring in series. The differential equation to describe the Maxwell model is

$$\frac{d\gamma}{dt} = \frac{1}{J}\frac{d\sigma}{dt} + \frac{\sigma}{\eta} \tag{1.3}$$

In this model, the liquid has a short time elastic response which stores the effect of the stress as strain, described by the spring, which is reversible when the stress is ceased. If the stress is continuously applied, the dashpot exponentially decreases the strain, leading to dissipation of energy from the system. This model has limitations in that it does not describe the creep in systems under continuous stress which is the effect that the strain rate is time dependent in viscoelastic systems.

Another model is the Klein-Voight model which puts the spring and dashpot in parallel. The short time behavior thus has both components of storage and dissipation. The differential equation describing this model is

$$\sigma = \frac{\gamma}{J} + \eta\frac{d\gamma}{dt} \tag{1.4}$$

This model has the material's strain decrease with time until it approaches a steady state value which is accurate for materials undergoing creep. Its limitations are that it does not model the relaxation very well in that upon cessation of the stress, the model predicts that the system takes a long time to return to its equilibrium state.

A third model, the Standard Linear Solid model, combines the previous models in that it

has a Maxwell model spring and dashpot in parallel with an additional spring. This model incorporates both the immediate short time elastic response and the exponential decay to a steady state strain value and can thus describe both the short and long time response. The Generalized Maxwell model is an even more general form of the Standard Linear Solid model which has various Maxwell spring branches with different spring constants and viscosities that describe the multiple time scales which may be present in a single system.

Along with these intuitive models comes the formalism that describes the viscous and elastic responses for classical liquids and solids. The viscous response follows the formalism of Chaikin and Lubensky[2] and the elastic response follows the treatment of Ferry[4]. The passive rheology derivation is the work of Mason, Weitz and company [3] [4]

1.3 Passive microrheology of viscoelastic fluids

1.3.1 Viscous response

To understand viscoelastic fluids, it is instructive to understand the limiting behaviors of a purely viscous and purely elastic material. For a purely viscous fluid, the viscous force which impedes the motion of a suspended paricle in the dilute limit is described by its diffusion

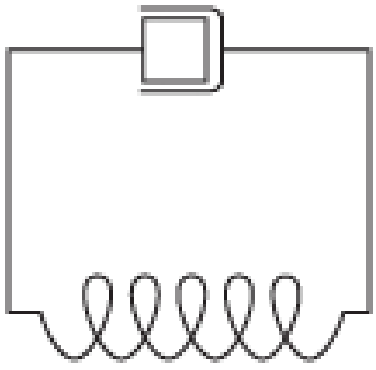

Figure 1.2: Klein-Voigt model

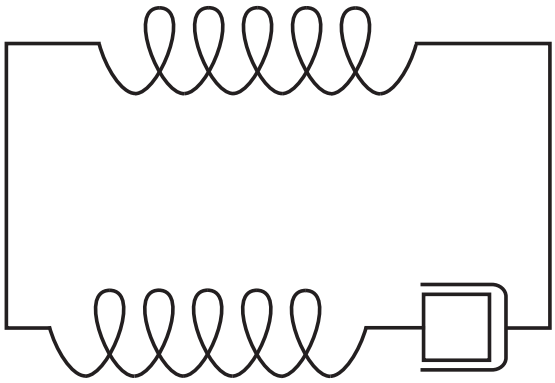

Figure 1.3: Standard Linear model

constant D. Such a system much obey a law of particle conservation

$$\frac{\partial n(\mathbf{x},t)}{\partial t} + \nabla \cdot \mathbf{j}(\mathbf{x},t) = 0 \tag{1.5}$$

where $\mathbf{j}(\mathbf{x},t)$ is the particle current and $n(\mathbf{x},t)$ is the particle number. If the system is not in density equilibrium, the system must diffuse in a manner such that the diffusion rate is proportional to the particle density gradient. This gives Fick's Law which is the simplest relationship between $\mathbf{j}$ and ∇n and introduces the diffusion constant D as the constant of proportionality between the two.

$$\mathbf{j} = -D\nabla n \tag{1.6}$$

Combining Fick's law and particle conservations gives the diffusion equation which governs the diffusive behavior of a variety of systems.

$$\frac{\partial n}{\partial t} = D\nabla^2 n \tag{1.7}$$

The particle density propagates according the to the diffusion Green function which obeys the same diffusion equation as the particle density. Using appropriate boundary conditions

and Laplace and Fourier transforms, the Green function which gives the particle density is

$$G(\mathbf{x},t) = \frac{1}{(4\pi D|t|)^{\frac{d}{2}}} e^{\frac{-|\mathbf{x}|^2}{(4D|t|)}} \tag{1.8}$$

If the particle density is initially localized at the origin and allowed to evolve in time obeying the diffusion Green function, the mean squared radial displayment may be obtained by integrating $|\mathbf{x}|^2 G(\mathbf{x},t)$ over a d dimensional sphere. Thus the density will occupy a region with mean squared radius proportional to the diffusion constant.

$$< |\mathbf{x}|^2 >= 2dD|t| \tag{1.9}$$

For a system not in equilibrium, the means by which energy is transferred so that particle density equilibrium is restored, is by stearic interactions with the molecules and potentials in the fluid. Einstein considered this interaction and observed that in thermodynamic equilibrium, the total particle current in the system must be zero and the density much satisfy the Boltzman relation. These two constraints give the Einstein relation which is the first fluctuation-dissipation relation based on equilibrium average.

$$D = \frac{T}{6\pi\eta a} \tag{1.10}$$

where η is the viscosity and a is the radius of the particle.

In the case of Brownian motion, the jostling of a particle suspended in fluid means that the particle postition is a randomly fluctuating stochastic variable. The probability that the particle is at a specific position can be related to the diffusion Green function mentioned above by taking an ensemble average. Thus the mean-squared displacement (MSD) can be a measure of the diffusion constant and viscosity of a system.

$$< (\Delta\mathbf{x})^2 >= 6Dt = \frac{k_B T}{\pi\eta a} t \tag{1.11}$$

This relationship is the cornerstone of passive microrheology whereby tracking the thermally driven random walk of a particle to obtain its MSD can be used to obtain the viscosity of a simple fluid.

1.3.2 Elastic response

There is no analogy for diffusion of a particle within an elastic solid but the models used to describe a solid under strain will provide the basis for the quantitative description of a viscoelastic fluid. The simplest model for a solid is a linear elastic solid which obeys 3 laws 1) The body is continuous and remains continuous under the application of external forces 2) Hooke's law which states that the displacement u is linearly dependent on the forces $P_1, P_2, ..., P_n$

$$u = a_1 P_1 + a_2 P_2 + ... + a_n P_n \tag{1.12}$$

where $a_1, a_2, ..., a_n$ are constants which depend on the Young's modulus of the solid and 3) There exits a unique unstressed state that the body returns to when all external forces are removed. These laws can be quantitatively expressed in the stress-strain relations involving the strain tensor γ_{ij} and the stress tensor σ_{ij}.

This description of a linear elastic solid is very accurate for infinitesimal strain but for macroscopic systems such as a vibrating rod which dampens to zero even in a vacuum, it is clear that the Hookean description is not comprehensive. To this end, models were developed which maintained the linear relationship between force and displacement but which included a time dependence which considers the history of the material (history in addition to the unstrained state which by definition the strained material must return to). Consider a system where there is a force function $F(t)$ and the displacement $u(t)$ which depends not only on $F(t)$ but on the entire force history of the system. Then, for infinitesimal force increments

of τ at time t, the linear elastic model is accurate, yielding

$$du(t) = c(t-\tau)\frac{dF}{dt}(\tau)d\tau \tag{1.13}$$

where c is a proportionality constant akin to the $a_1, a_2, ..., a_n$ of the linear elastic solid. Integrating over the entire history, we obtain

$$u(t) = \int_0^t c(t-\tau)\frac{dF}{dt}dt \tag{1.14}$$

Alternatively, we can relate elements of the strain and stress tensors, γ_{21} and σ_{21} in a similar fashion yielding the constitutive relation

$$\sigma_{21}(t) = \int_0^t G(t-\tau)\dot{\gamma}_{21}(\tau)d\tau \tag{1.15}$$

where $G(t)$ is the complex shear modulus.

1.3.3 Passive rheology

In order to experimentally determine the viscoelastic response, standard rheological measurements are performed where a periodic shear strain $\gamma_o sin(\omega t)$ is applied and the resultant stress $\sigma(t)$ is measured. The frequency-dependent mechanical response is described by the complex shear modulus $G(\omega) = G'(\omega) + iG''(\omega)$. The real component $G'(\omega)$, which is in phase with the applied shear, describes the storage component and the imaginary component $G''(\omega)$, which is out of phase with the applied shear and in phase with the shear rate, describes the dissipative component.

$$\sigma(t) = \gamma_o[G'(\omega)sin(\omega t) + G''(\omega)cos(\omega t)] \tag{1.16}$$

The real and complex components also can be written as a modulus and phase $G^*(\omega) = |G|e^{-i\delta}$. The phase angle δ tells how much the strain lags the stress and $tan(\delta)$ is a common measure of the internal friction of a viscoelastic material. Alternatively, the material may be described by the frequency dependent complex viscosity

$$\eta(\omega) = \frac{G(\omega)}{\omega} \tag{1.17}$$

$G^*(\omega)$ can be related to the Brownian fluctuations of a material by first describing the motion of the particle in terms of the generalized Langevin equation.

$$m\dot{v}(t) = f_R(t) - \int_0^t \zeta(t-\tau)v(\tau)d\tau \tag{1.18}$$

This equation, first derived formally by Kubo, mirrors the constitutive relation and considers the history of a system to determine the present motion of an embedded particle. The first term on the righthand side $f_R(t)$ describes the random forces that are incident on the particle at the current time t which reflects the instantaneous viscous response. The second term considers the contributions of the elastic response over a time period t via the time dependent memory function $\zeta(t)$. This equation takes into account that the elastic response of the material stores energy which is ultimately released back into the system at some later time τ. This delayed release of energy contributes to the motion of the particle at some later time and by observing the particle's current motion at time t, one can determine the integrated elastic response over t as well as the instantaneous viscous response.

The first step towards relating the motion of this Brownian particle to the complex shear modulus involves relating the mean squared displacement with with memory function ζ. The unilateral Laplace transform of the generalized Langevin equation is taken to obtain the relation in terms of the Laplace frequency s and to reduce the convolution function to a

product.

$$\tilde{v}(s) = \frac{\tilde{f}_R(s) + mv(0)}{ms + \tilde{\zeta}(s)} \tag{1.19}$$

Then a time average is taken and the equipartition theorem

$$m < v(0)v(0) >= m < v(t)v(t) >= k_B T \tag{1.20}$$

is applied to obtain

$$< \tilde{v}(s)v(0) >= \frac{k_B}{ms + \tilde{\zeta}(s)}. \tag{1.21}$$

The first term in the denominator reflects the short time inertial effects and can be ignored for all but the highest frequencies. The autocorrelation of the velocity can be written in terms of the Laplace transform of the MSD based on the Green-Kubo formalism to obtain:

$$\tilde{\zeta}(s) = \frac{6k_B T}{s^2 < \Delta\tilde{r}^2(s) >} \tag{1.22}$$

Assuming the exact relationship between the frequency dependent viscosity and the memory function for a purely viscous fluid can be extended to approximate the viscoelastic regime[3] we obtain

$$\tilde{\eta}(s) = \frac{\tilde{\zeta}(s)}{6\pi a} \tag{1.23}$$

Recalling (1.13), the complex shear modulus can thus be related to the MSD to obtain the Generalized Stokes Einstein Relation (GSER) which now connects the experimentally determined MSD with the complex shear modulus which describes the stress strain relationship in a viscoelastic material.

$$\tilde{G}(s) = \frac{k_B T}{\pi a s < \Delta\tilde{r}^2(s) >} \tag{1.24}$$

$\tilde{G}(s)$ can be related to the frequency dependent $G(\omega)$ by taking the inverse Laplace transform

and then the Fourier transform. In the Fourier domain, the GSER is given by

$$G^*(\omega) = \frac{\eta}{\omega} = \frac{k_B T}{\pi a i \omega F(< \Delta r^2(t) >)} \tag{1.25}$$

which agrees with the MSD vs time relationship given by viscous theory from equation [1.7]. The real and imaginary parts of the Fourier domain complex shear modulus are related by the Kramers Kronig relations and thus both values can be calculated from a single rheology measurement. It is then possible to determine both the storage and dissipative responses of a viscoelastic material simply by determining the MSD of a tracer particle allowed to passively diffuse with thermal energy $k_B T$.

1.4 Rotational Rheology

Rotational Brownian motion is analogous to translational brownian motion in many ways. We know for an classic, rigid particle, the equipartion theorem states that the energy is distributed equally to the 6 degrees of freedom, 3 translation and 3 rotation. Translational Brownian motion is modelled as a random walk with a normal distribution of displacements and rotational Brownian motion can be modelled similarly as a random walk on the surface of a sphere [8] as long as a reference axis can be determined. Particles with an optical, or structural anisotropy are the most accessible to experimental measurements. Many molecules have an optical anisotropy due to the dipole moment of their bonds. As the molecule rotates, the direction of this dipole moment changes and can be an axis to determine the rotational motion experimentally [9].

For classical diffusive rotational diffusion, Debye developed a model to describe how a system of particles with a common orientation goes about reorienting due to random thermal collisions. Assuming that collisions are so frequent that only small rotations are possible, he assumed all particles are initially oriented in some direction and then are constrained to

diffusion only on the surface of a unit sphere. Thus, in terms of the diffusion equation in eqn 1.1, the modulus of x is constrained to be 1. Using spherical coordinates, we can obtain the rotation diffusion equation or Debye equation to be

$$\frac{\partial c(\mathbf{x},\mathbf{t})}{\partial t} = -\Theta \hat{I}^2 c(\mathbf{u},\mathbf{t}) \tag{1.26}$$

where I is the dimensionless orbital angular momentum operator and Θ is the rotational diffusion coefficient.

The former derivation of the Generalized Stokes Einstein Relation (GSER) was for translational rheology which is the most commonly studied due to the relative ease of observing translational motion as opposed to rotational motion. The argument for angular passive microrheology follows the same formalism, starting with the angular generalized Langevin equation of motion

$$I\dot{\theta}(t) = \tau_R(t) - \int_0^t \zeta(t-\tau)\theta(\tau)d\tau \tag{1.27}$$

where I is the rotational intertia and τ_R are the random thermal torques on the particle. This leads to the angular Generalized Stokes Einstein relation

$$\tilde{G}(s) = s\tilde{\eta}(s) = \frac{k_B T}{4\pi a^3 s < \Delta\tilde{\theta}^2(s) >} \tag{1.28}$$

An important advantage to note for angular microrheology is the inverse size cubed dependence of the viscosity and complex shear modulus. This indicates that it is possible to access a much larger range of viscosities with angular motion than linear diffusion with comparably sized partices. One would have to observe significantly smaller particles to probe the same viscosity range which poses experimental difficulties due to signal to noise ratio and accuracy.

1.5 Obtaining $G(\omega)$ from the MSD

Viscoelastic theory has been derived from elastic theory through the Langevin equation of motion and the complex shear modulus to obtain the GSER and it is now possible to obtain the dissipative and storage modulus from a MSD curve which is experimentally obtained. To extract the real and imaginary components of the complex shear modulus from the MSD data, the most direct method is to numerically inverse Laplace transform the data and fit it to an analytic function. This method is likely to introduce errors in the moduli obtained from data at the data extrema for the numerical Laplace transform and it can also be difficult to find an appropriate fitting function.

Mason [6] developed an alternate method to reduce the errors by using a power law expansion about a certain frequency ω. This local power law expansion is valid because power law relationships are scale invariant which reflect the random walk motion of the probe particle as Brownnian motion is a classical scale invariant phenomena. A power law function is any function which has the form $Pr[X \geq x] \sim cx^{-\alpha}$ where $c > 0$ and $\alpha > 0$. Such functions describe phenomena where the likelihood of small events is large and large events are small. A random walk follows a power law because the the probability of the particle to have undergone a displacement Δx is inversely proportional to a power of x. Due to this power law dependency, the MSD may be approximated as

$$\langle \Delta \vec{r}^2(t) \rangle \approx \langle \Delta \vec{r}^2(1/\omega) \rangle (\omega t)^{\alpha(\omega)} \tag{1.29}$$

where $\langle \Delta \vec{r}^2(1/\omega) \rangle$ is the value of the MSD at $t = 1/\omega$ and

$$\alpha(\omega) = \left. \frac{dln\langle \Delta \vec{r}(2)(t) \rangle}{dlnt} \right|_{t=1/\omega} \tag{1.30}$$

The log-log plot of the function versus time is called the complementary cumulative distribution function or signature of the power law and reflects the scale invariance of the function.

The slope of this line is the power law exponent at the particular frequency or time delay of interest which describes how quickly the power law tail drops off. For a purely diffusive systems, α approaches 1 whereas a subdiffusive system with a strong elastic component would result in an α less than 1.

Once a power law expansion has been taken, the Fourier transform is taken directly using the gamma function and the derivative property of Fourier transforms to obtain

$$i\omega F\langle\Delta r^2(t)\rangle \approx \langle\Delta r^2(1/\omega)\Gamma[1+\alpha(\omega)]i^{-\alpha(\omega)} \tag{1.31}$$

With this relationship and the Fourier representation of the GSER, we obtain

$$G^*(\omega) \approx \frac{k_BT}{\pi a\langle\Delta r^2(1/\omega)\Gamma[1+\alpha(\omega)]i^{-\alpha(\omega)}} \tag{1.32}$$

Then using Euler's equation and $i = e^{i\frac{\pi}{2}}$, we obtain

$$G'(\omega) = |G^*(\omega)|cos(\pi\alpha(\omega)/2) \tag{1.33}$$

$$G''(\omega) = |G^*(\omega)|sin(\pi\alpha(\omega)/2) \tag{1.34}$$

for the storage and dissipative modulus respectively where

$$|G^*(\omega)| = \frac{k_BT}{\pi a\langle\Delta r^2(1/\omega)\rangle\Gamma[1+\alpha(\omega)]} \tag{1.35}$$

From this form of the complex shear modulus as a function of MSD and real time, we can recover the standard diffusion equation for a purely viscous fluid without any frequency dependence in the viscosity. $\alpha(\omega) = 1$ for a linear MSD vs time dependence giving $\Gamma[2] = 1$. We then remove the frequency dependence of the complex shear modulus which yields $G' = 0$ for the storage modulus and

$$G'' = \frac{k_BT}{\pi a\langle\Delta r^2\rangle} \tag{1.36}$$

For systems where the MSD is not a smooth curve, this method introduces large errors and an alternative method has been developed for these potentially very interesting systems.

The derivation for rotational motion follows the same general form with the linear MSD replaced by angular MSD, the particle size replaced by the particle size cubed and a factor of 4 in the denominator yielding [32]

$$|G^*(\omega)| = \frac{k_B T}{4\pi a^3 \langle \Delta r^2(1/\omega) \rangle \Gamma[1+\alpha(\omega)]} \tag{1.37}$$

where the real and imaginary are given as in [1.27] and [1.28]. This gives the proper units for the complex shear modulus and viscosity and explicitly shows the increase in viscosity range accessible to rotational microrheology.

1.6 Dynamic and Kinematic Viscosity

The most common characterization of the response of a fluid to a shear stress is given by the viscosity of the fluid, not the complex shear modulus. The viscosity measured by common viscometry techniques can be related to the more general complex shear modulous. There are two types of viscosity, the first is dynamic or absolute viscosity which are generally synonymous. It is the proportionality constant between shear stress and strain rate and has units of $N \cdot s/m^2$, $Pa \cdot s$ or $kg/m \cdot s$ and in CGS units is described by the poise (p) where $1 poise = g/cm \cdot s = 1/10 Pa \cdot s$. The other is kinematic viscosity which is normalized by the inertial force of the liquid which is kinematic viscosity. Kinematic viscosity is thus dynamic viscosity divided by the density of the fluid and has units of m^2/s and in CGS units is described by Stokes or more commonly Centistokes (cSt).

Both the dynamic and kinematic viscosities are frequency dependent for viscoelastic systems but the steady state viscosity is the value generally generally attributed to the material in literature. The dynamic and kinematic are related to the complex shear modulus

through the frequency and the real, in phase component of the viscosity approaches the steady state dynamic viscosity as the frequency approaches zero. The steady flow viscosity is measured by simple viscometry techniques such as measuring the time it takes a set amount of liquid to flow a certain distance or falling sphere viscometry which measures the time it takes a sphere to fall a set distance.

For systems which cannot be described by a single value, rheological techniques are then applied. Mechanical rheometers, as opposed to viscometers, are able to vary the shear rate of a liquid. Usually using two plates or concentric cylinders, they are able to apply a controlled shear rate and then they measure the shear force the liquid applies in response via a torque, change in pressure or some other means. In this way, a frequency dependent response can be measured which can by analyzed to obtain the complex shear modulus.

1.7 Viscosity and Temperature

All values of the viscosity of a fluid: dynamic, kinematic, frequency dependent or independent, can depend strongly on the temperature of the fluid. In general, the viscosity of a liquid decreases and the temperature increases. Several models have been proposed to describe this dependence and all of them are applicable in some regime though none describe the wide variety of fluids comprehensively over all temperatures.[10] Among them are the exponential model by Reynolds [11] given by

$$\nu(T) = Ce^{-fT} \tag{1.38}$$

where C and f are constants. It is the simplest model of temperature dependence of viscosity and is an empirical based on the Reynold's studies of the temperature dependence of oil.

Another empirical model was proposed by Andrade[12] who observed that the Arrhenius

form given by

$$\nu(T) = Be^{\frac{E}{RT}} \tag{1.39}$$

where B is a constant, E is the activation energy and R is the gas constant can also describe the viscosity temperature dependence. The Arrhenius model was first proposed to describe the rate of chemical reactions but has been applied to many systems including viscocity. This still widely used model best decribes low molecular weight fluids and polymers above their melting point but is inaccurate below the glass transition where the viscosity diverges abruptly.

For the viscosity of polymers over a larger range of temperatures, the Williams, Landel and Ferry (WLF) [13] model is more commonly used and can describe polymers from the glass transition to approximately 100^oC above. The WLF model is given by

$$\nu(T) = \nu_o \frac{-C_1(T - T_o)}{C_2 + (T - T_o)} \tag{1.40}$$

where C_1, C_2 and T_o can be fit to data if available but can also take on universal values to model general liquids when data is not available. A majority of fluids can be described by these three models or variations of them.

1.8 Current Microrheology Techniques

1.8.1 Ensemble techniques

The most common methods of doing microrheology involve looking at large ensembles of particles with light scattering techniques. Dynamic Light Scattering(DLS) also known as Quasi Elastic Light scattering(QELS) and Photon Correlation Spectroscopy (PCS) or Diffusing Wave Scattering(DWS) [8][14][15][16][3][32] are techniques where the scattering from a coherent light source causes constructive and destructive interference which can provide

information about the distance between particles as a function of time. DWS is the extension of DLS to strongly scattering and optically diffusive media where multiple scattering effects must be considered.

There are two types of DLS and DWS, polarized and depolarized. The polarized looks at the correlation functions between light which has the same polarization before and after scattering while depolarized looks at the correlation between light of different polarizations. Polarized has components from the scattering due to translational and rotational motion although the rotational component is small and hard to detect. Depolarized light scattering can be used to look at rotational motion at small angles though experimentally, the signal is also weak. Ensemble techniques have the advantage of averaging over many particles, resulting in good statistics over the bulk fluid. It is not as suitable for materials which are not homogeneous or have microscopic or mesoscopic structure. For such systems, single particle tracking can provide information about local viscosities and their variations.

1.8.2 Single Particle Tracking

Single particle tracking (SPT) can be done with microscopes of many types, from standard light microscopes to confocal microscopes for studying fluids in three dimensions. The limits of SPT concern the resolution of the microscope used, the time resolution of the recording device, and the diffraction limit of the light which provides a fundamental limit for the size of particle able to be tracked. Since particle size is inversely proportional to viscosity, the diffraction limit also limits the viscosity which can be measured by translational SPT. Current limits set by the resolution of imaging cameras and the 1 micron particles most commonly used in single particle tracking is $10^4 poise$.

Rotational single particle tracking can increase this viscosity range by two orders of magnitude for the particles currently used allow for the study for a wider variety of materials such as highly viscous polymers which cannot currently be studied using passive microrheology. An additional advantage of rotational microrheology is the ability to probe materials

which microstructure such as voids and networks which may hinder translational motion. In such systems, there is the viscosity within the voids and the also a separate viscosity which describes the bulk sample. Due to the difficulty of observing the rotations of an isotropic particle, many other techniques have been developed to overcome this obstacle. It is possible to use anisotropic particles but that neccesitates consideration of the moment of inertia about the various rotation axis and small rotations are still difficult to observe.

One such technique is that of Modulated Optical Nanoprobes(MOONs) [17] which uses an optical anisotropy of a spherical particle to determine orientation. The MOON technique uses fluorescent spherical particles where one hemisphere is coated with an opaque metal such as aluminum or gold. The resulting particles will fluoresce in various crescent shapes which are determined by their orientation. The rotational brownian motion of such a particle can be determined by tracking the shape of the fluorescence of the particle and the resolution is determined by the imaging microscope and is typically of a few degrees.

Another technique is Light Streak Tracking(LST) [18][19] where birefringent thin wax microdisks are used as tracer particles trapped in a laser tweezer system. The trapped disks orient themselves such that their symmetry axis is perpendicular to the beam. This causes the backscattered light to form a streak which is parallel to the faces of the disk and this light can be used to sensitively detect the orientation of the disk. The streak is recorded with a camera giving an angular resolution of a few microradians. The trapping power can be controlled by the polarization and power of the laser and the forces on the particle can be separated into a white noise thermal torque, a viscous drag torque and an optical restoring torque. The data shows that the thermal energy is insufficient for the particle to escape the potential well cause by the optical torque of the laser and thus the particle undergoes harmonically bound Brownian motion.

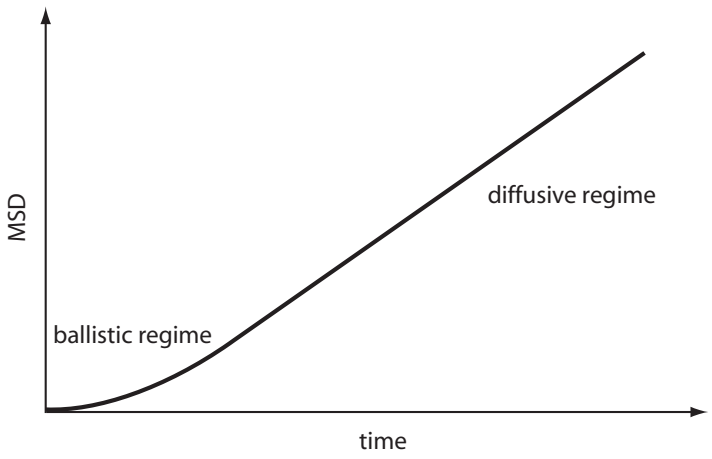

Figure 1.4: MSD vs time for simple Brownian motion according to viscous theory. The slope in the diffusive regime is the diffusion constant from which the viscosity may be determined

1.9 MSD and diffusion

The MSD versus lag time graph shows the diffusive behavior of the embedded particle. The most common MSD vs lag time relationship is that of a Brownian particle. For purely a Brownian, diffusive particle, there should be a linear relationship between the MSD and lag time as described previously with eqns [1.5-1.7]. This is only true at long enough times where the viscous force of the liquid can affect the particle. Einstein's work on Brownian motion proved the existence of molecules due to their collisions with the particles providing this viscous force. At timescales shorter than the average collision time between a liquid molecule and the particle, the particle has a constant velocity which leads to a linear dependence of position on lag time. This gives a quadratic dependence in the MSD vs. lag time graph for short enough times on the order of $10^{-6} sec$ and is referred to as the ballistic regime. Longer times have the linear behavior for a diffusive particle in a simple viscous liquid which can be most easily seen on a log-log plot where the graph has a slope of 1.

1.9.1 Anomalous Diffusion

There are types of diffusion that do not exactly fall into the category of simple diffusion and are called anomalous diffusion. In regular diffusion $MSD \sim t$ but in anamolous diffusion $MSD \sim t^a$ where $a \neq 1$. Ballistic motion is an example where $a = 2$. When $a > 1$, the motion is said to be superdiffusion and can be due to driven motions which are especially relavent in biological systems. $a < 1$ is considered subdiffusive motion and motion of this type can be attributed to complexity in the material from crowding to viscoelasticity and a myriad of other causes. Much effort has been made to theoretically understand and model subdiffusive behavior.

In many systems, there can also be a transition between the different types of diffusive behaviors. For example, van Zanten et al[33] studied the motion of $0.966\mu m$ polysterene latex spheres in a Maxwellian fluid of wormlike micelles composed of cetyltrimethylammonium bromide (CTAB) and potassium bromide (KBr). They modeled this system by the Langevin description and predicted a plateau region where the particle oscillates in an elastic cage while undergoing a very slow viscous dissipation. Wormlike micelles are living polymers, which unlike regular polymers, are breaking and recombining and thus do not provide a quenched length distribution. This breaking and reforming provides another means by which energy may be dissipated and if the timescale is sufficiently short, it is the main pathway for stress relaxation and results in the Maxwellian viscoelastic behavior. The MSD vs. lag time curves taken by diffusing wave spectroscopy averages over thousands of particles show subdiffusive behavior of $MSD \sim t^{0.8}$ and become classically diffusive at longer delay times. The curves were fit to the models described above for times greater than the ballistic regime. At very short lag times, the model deviates and other effects such as Rouse and breathing modes are thought to play a role. The plateau onset time of the data deviated greatly from the Langevin model prediction time and it was found that the Doi-Edwards tube model which predicts subdiffusive behavior with the Mason-Weitz approximation more accurately describe the early

onset time of the MSD plateau. Though the Langevin description did not comprehensively describe the structural fluctuations, microrheology was able to show the timescale at which these structural changes are taking place via the change in diffusive behavior

In an optical light microscope single particle tracking experiment, Valentine et al[34] observed a transition from diffusive behavior to subdiffusive behavior of 500nm polystyrene latex spheres for agarose which forms a polymer network. The network allows the particle to move freely with the pores created by this polymer but hinders the motion across cavity walls, causing the subdiffusive behavior at the long timescales which correspond to longer length scales. They also studied the more complex system of f-actin which creates cages of different sizes, the MSD behavior of this material is even more complex, never reaching simple diffusion due to the ability of particles to explore different size cages at many timescales.

1.10 Microrheology and Transport

Viscosity is an important fundamental property and can be determined via particle mobility or fluid rheology but it also provides information about an object's mobility and diffusion liquid environment. This information is especially important for transport phenomena in biology to understand how important biological materials such as red blood cells diffuse and propogate and how intracellular mobility is effected by external stimuli[22]. For such complex systems with microstructure, it is clear that the bulk viscosity differs from the viscosity value obtained via the motion of a particle which must sample the local environment. For systems with multiple solvents and other solutes, it is more complex still and the bulk viscosity value does not provide information about transport of individual particles. Microrheology is thus a valuable tool for studying the transport properties of systems in addition to determining the fundamental properties of a fluid.

2

Chapter 2

X-ray methods and Facilities

2.1 X-ray Diffraction from micron sized crystals

2.1.1 Crystals

Crystals are regular periodic structures constructed by the repitition some fundamental unit such as an atom, ion, molecule or even protein. These constituents are called the basis and are typically one or more atoms for classic crystals although they can be colloids, nematic molecules or the protiens previously mentioned. There is a well developed method of describing crystals and their diffraction, our description follows the treatment of Ashcroft and Mermin[35] and Warren[36]. Mathematically, this fundamental lattice which describes the periodicity can be described by a set of lattice vectors which describe a Bravais lattice. Each element of the crystal sits at a linear superposition of these lattice vectors.

$$\mathbf{R} = n_1\mathbf{a}_1 + n_2\mathbf{a}_1 + n_3\mathbf{a}_1 \tag{2.1}$$

The lattice in coordination space is referred to as the direct lattice. The volumes of physical space which correlate to each lattice point are called the primitive unit cells. They must have the characteristic that they fill all space with no overlapping components and must contain precisely one lattice point. There is no unique primitive unit cell for a given lattice and it is often more useful to use a conventional unit cell which can be a nonprimitive unit cell which can fill all space with no overlaps by a superposition of a subset of the vectors in

a Bravais lattice.

Another important description of a crystal is the reciprocal lattice for a given Bravais lattice. The reciprocal lattice is defined as the set of wave vectors which yield plane waves with the periodicity of a given Bravais lattice. It can alternatively and equivalently be thought of as the set of lattice planes which contain all the lattice points of the crystal. The reciprocal lattice $\mathbf{K}$ must fill the mathematical condition that for any $\mathbf{r}$

$$e^{i\mathbf{K}\cdot(\mathbf{r}+\mathbf{R})} = e^{i\mathbf{K}\cdot\mathbf{r}} \qquad ie \tag{2.2}$$

$$e^{i\mathbf{K}\cdot\mathbf{R}} = 1 \tag{2.3}$$

A more straighforward definition of the reciprocal lattice can be written as the product of the direct lattice.

$$b_1 = 2\pi\frac{\mathbf{a}_2\times\mathbf{a}_3}{\mathbf{a}_1\cdot(\mathbf{a}_2\times\mathbf{a}_3)} \qquad b_2 = 2\pi\frac{\mathbf{a}_3\times\mathbf{a}_1}{\mathbf{a}_1\cdot(\mathbf{a}_2\times\mathbf{a}_3)} \qquad b_3 = 2\pi\frac{\mathbf{a}_1\times\mathbf{a}_2}{\mathbf{a}_1\cdot(\mathbf{a}_2\times\mathbf{a}_3)} \tag{2.4}$$

The reciprocal lattice vectors are perpendicular to any set of lattice planes and are therefore a convenient way of indicating the directionality of the crystal. The Miller indices h, k, l are the coefficients of the reciprocal lattice vector normal to the set of lattice planes of interest, for example the $(4, \bar{2}, 1)$ planes are the set of lattice planes normal to the $4\mathbf{b}_1 - 2\mathbf{b}_2 + 1\mathbf{b}_3$ direction.

2.1.2 Diffraction

X-ray diffraction, by virtue of the lattice scale wavelengths of x-rays can be used to see the crystal lattice of materials. W. H. and W. L Bragg first observed this phenomena and explained it by treating the crystal as a set of parallel planes which reflect incident x-rays. When the geometry is such that the rays from the planes interfere constructively, there is a point of high intensity called the Bragg peaks. The geometric condition of incidence angle

θ and a crystal with plane spacing d is described by the Bragg condition

$$n\lambda = 2dsin\theta \tag{2.5}$$

An alternative way of understanding diffraction was given by von Laue. He treated the atoms in the lattice not as planes but as individual scatterers. For two scatterers separated by a distance d with x-rays incident at a wavevector k, there will be intensity at an exit wavevector k' when the two scattered waves constructively interfere. The interference condition is given by

$$\mathbf{d} \cdot (\mathbf{k} - \mathbf{k}') = 2\pi m \tag{2.6}$$

for integer m.

In order for there to be intensity for an array of scatterers in a Bravais lattice, all the scattered rays must interfere constructively and that is given by fulfilling the condition for all lattice vectors $\mathbf{R}$

$$\mathbf{R} \cdot (\mathbf{k} - \mathbf{k}') = 2\pi m \tag{2.7}$$

or alternatively

$$e^{i(\mathbf{k}-\mathbf{k}')\cdot R} = 1 \tag{2.8}$$

This says that the scattering vector $\mathbf{K} = \mathbf{k} - \mathbf{k}'$ must be a reciprocal lattice vector of the crystal. The equivalence of the Bragg and von Laue descriptions is based on the reciprocal lattice vectors being defined by both the condition in (3.3) and as the set of planes which include all the lattice points of a Bravais lattice.

The Bragg and von Laue descriptions of Bragg scattering are useful models to understand the basic concept but overlook some of the subtle details of scattering in crystals. It is important to note that the scattering mechanism is due not to reflection from lattice planes or atoms themselves but from the electrons which accelerate by being driven by the incident radiation. These oscillating charges then produce the scattered field at the same wavelength

with a certain polarization. This description does not account for the lower energy Compton scattering but is the process which gives Bragg scattering. Another implicit assumption for both descriptions is the lack of multiple scattering events in the crystal knows as the kinematical assumption.

Now that we know the scattering condition from the lattice itself, we can take into consideration the basis of the crystal. For a monotonic basis, the atoms scatter in same way but from different positions in the unit cell. The phase difference from two different positions $\mathbf{d}_i$ and $\mathbf{d}_j$ follows from the von Laue description as $e^{i\mathbf{K}\cdot(\mathbf{d}_i-\mathbf{d}_j)}$. The scattered amplitude from the individual positions can thus be written as $e^{i\mathbf{K}\cdot\mathbf{d}_1}, ..., e^{i\mathbf{K}\cdot\mathbf{d}_n}$. For an entire basis, the total contribution of the different atomic positions is

$$S_{\mathbf{K}} = \sum_{j=1}^{n} e^{i\mathbf{K}\cdot\mathbf{d}_j} \tag{2.9}$$

$S_{\mathbf{K}}$ is known as the geometric structure factor and can be most dramatically seen in the forbidden reflections for certain basis.

Since it is the electrons which do the scattering, the picture is further complicated by the different electron distributions of different atoms and ions which must be taken into account by the atomic form factor f_j. Assuming an electron distribution $\rho_j(\mathbf{r})$, the atomic form factor is given by the Fourier transform of the electron charge distribution

$$f_j(\mathbf{K}) = -\frac{1}{e}\int d\mathbf{r} e^{i\mathbf{K}\cdot\mathbf{r}}\rho_j(\mathbf{r}) \tag{2.10}$$

Combining the atomic elements, we obtain the complete structure factor

$$S_{\mathbf{K}} = \sum_{j=1}^{n} f_j(\mathbf{K}) e^{i\mathbf{K}\cdot\mathbf{d}_j} \tag{2.11}$$

The actual calculation of the structure factor can be very complex. Simple electron geometries such as spherical distribution can approximate core electrons but are not accurate for

other electrons in the atom. Analysis of the structure and form factor provides important additional information than Bragg scattering alone.

2.1.3 Ewald Construction

An instructive way of graphically interpreting the Bragg scattering off the lattice is by using the Ewald construction. The Ewald construction consists of the reciporcal space lattice whose origin is set by the center of rotation of the crystal. The incident wavevector k is drawn beginning at the origin and a sphere centered at the tip of k. A Bragg diffraction spot can be observed if any reciprocal lattice points fall on this sphere. The direction of the scattered beam k' may be determined by drawing a vector from center of the Ewald sphere to the edge. The scattering vector $K = k - k'$ is then guaranteed to be a reciprocal lattice vector in this geometry.

2.1.4 Diffraction Experiments

X-rays can be used to find the lattice, basis and even the atomic species of a crystalline material. There are many types of diffraction experiments to extract this information depending on the individual sample. The Ewald construction is a useful way of picturing these different methods. The first method is to use a broadband source which would increase and decrease the radius of the Ewald sphere, detecting all the Bragg points which are in that range. Another method is the rotating crystal method which rotates the crystal at a constant wavevector. This corresponds to rotating the reciprocal lattice about the origin and allows the Ewald sphere to intercept any Bragg points along its trajectory. A completely equivalent method is to rotate the source, thereby rotating k. The third method, which is most closely related to the present work, is the powder method. This method involves a crystalline powder sample where the crystals are randomly oriented. The reciprocal lattice is now no longer a set of discrete points but instead each lattice point is now a lattice sphere

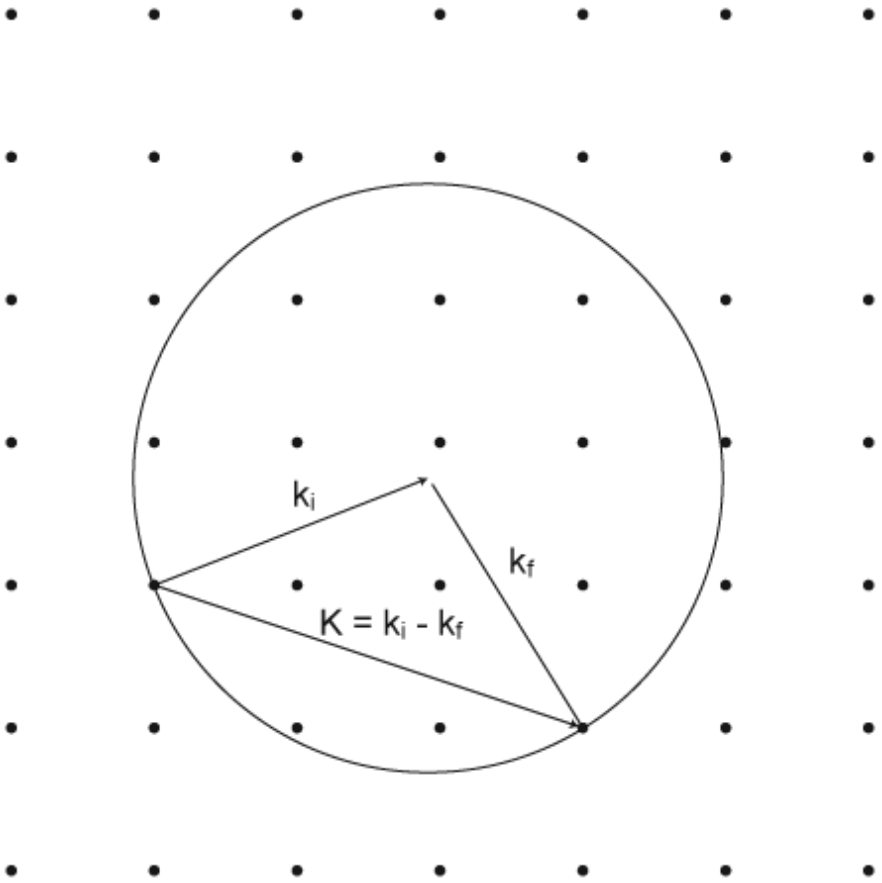

Figure 2.1: Ewald sphere contruction

since the crystals more or less provide a continuous array of orientations. The intersection of the Ewald sphere and the lattice point sphere is a circle and by varying the angle between k and k', one can sample a large portion of the Ewald sphere.

2.1.5 Coherent single particle imaging

The new technique of Coherent X-ray Diffraction Imaging is based in diffraction but utilizes the increased flux and coherence of modern x-ray sources. This techniques uses the long coherence lengths of modern sources to illuminate a compact object smaller than the coherence lengths of the beam. Under these conditions, the diffraction from a perfect lattice $L(r)$ of a three dimensional shape function $s(r)$ is given by the squared modulus of

$$A(\mathbf{q}) = \int s(\mathbf{r})L(\mathbf{r})e^{i\mathbf{q}\cdot\mathbf{r}}dr$$

Using the convolution theorem for Fourier integrals, this equation gives an image of the three dimensional Fourier transform of the electron density of the compact object around every reciprocal lattice point. The intensity observed is the real amplitude of this Fourier Transform. For typical experimental parameters, the length scale of the object is 3-4 orders of magnitude larger than the X-ray wavelength. Thus the k-vectors are large compared to the Fourier transform of the object and the curvature of the Ewald sphere may be neglected. One can estimate that what is observed is a real two dimensional slice through this three dimensional Fourier Transform. This two dimensional slice in reciprocal space corresponds to a single projection of the object in real space.

In an experiment, only the intensity of this two dimensional slice is observed and the phase information is lost. Finding methods to treat this famous Phase Problem is the key to recovering the structural information of the crystal from the diffracted intensity. D. Sayre[23] proposed that by sampling at greater than or equal to the Nyquist frequency, one can create an overdetermined problem which can be solved by iterative methods. It

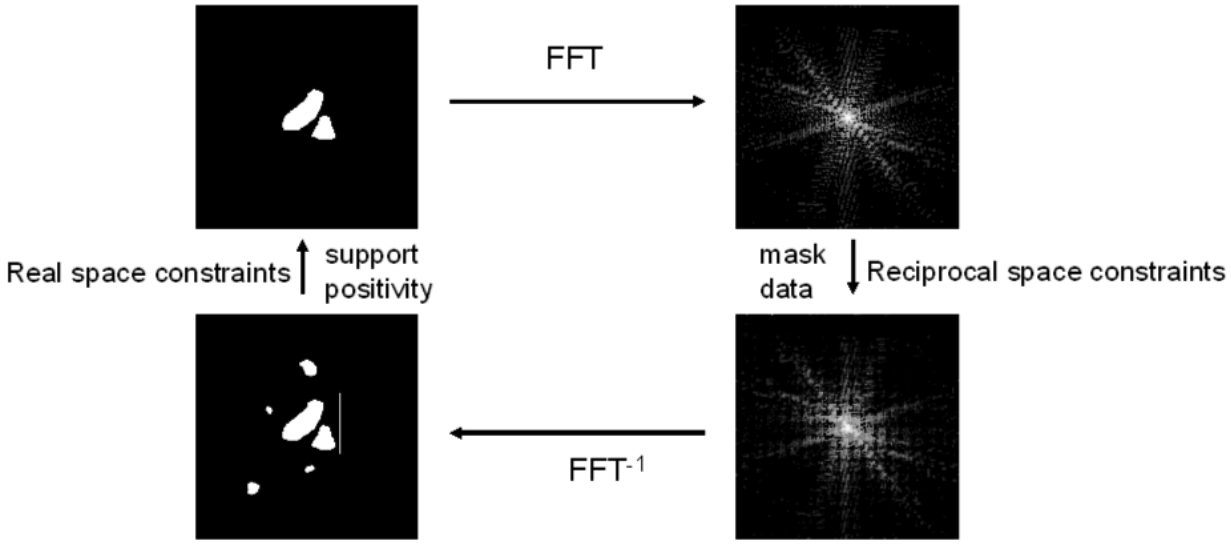

Figure 2.2: Iterative algorithm using real and reciprocal space contraints

built on the phase retrieval algorithms proposed by Gerchberg and Saxton[24] and expanded upon by Fienup[25]. Miao et al.[26] and Robinson et al.[27] showed that these algorithms were applicable to experimentally obtained diffraction patterns to show the structure of prearranged shapes and nanocrystals.

Phase Retrieval Algorithms were introduced by Gerchberg and Saxton in 1972 and consist of utilizing known information in both real and reciprocal space and applying iterative algorithms until a consistent set of phases is found that satisfy both sets of information. Sayre and Fienup expanded upon this idea in the early 1980's by introducing the idea that oversampling the diffraction pattern at twice the Nyquist frequency would lead to an overdetermined analytic problem. This condition corresponds to getting sufficient resolution in the diffraction image which can be obtained with advanced charge coupled devices (CCDs). The most common phase retrieval algorithms are the Hybrid Input-Output (HIO) and Error Reduction (ER) algorithms, both of which have the same basic structure.

These algorithms start with a set of random phases in reciprocal space and a support in real space. The support defines the boundaries in which the object must fit in real space. A good estimate can be calculated from the diffraction pattern itself if no prior information

is known about the sample. A fast fourier transform of the real space intensities which are contained by the support is then taken. The phases are retained, but theintensities are replaced by the experimental data. Then the new intensities and old phases are inverse fourier transformed to obtain an image in real space. Intensities outside the support are set to zero while intensities inside are kept and then the process is repeated. One iterates until a set of phases consistent with both the real space support and reciprocal space diffraction pattern is found and the goodness of fit is quantified by a χ^2 value which compares the calculated intensities with the measured intensities.

2.2 Diffraction and Dynamics

In addition to determining structure, Bragg diffraction can also be used to study the dynamics of crystalline materials. The lattice planes which provide structural information about the crystal also provide an inherent orientational marker. For single crystal Bragg diffraction, finding the Bragg reflections can be used to determine the orientation of a crystal. For powder diffraction, the random orientations of the various cystalites gives Bragg intensity at various positions along the Ewald sphere and the large numbers of crystals gives the rings of continuous intensity. If the concentration of crystals illuminated by the x-ray beam is such that there are a few spots of intensity in the Ewald sphere, the dynamics of those individual crystals can be studied. Boutet, et al studied the destruction of ferritin crystals by looking at invidual crystals in Bragg reflection. One can also determine structural changes such as compression or expansion of crystal lattices due to pressure, interface lattice mismatch, phase changes or radiation damage by looking at how the Bragg intensity changes or moves.

In addition to determining structural changes, Bragg diffraction can also be used to study motion and orientational changes in crystals. For rheology, it provides information about rotational dynamics which has the benefit of increasing the viscosity range which can be accessed due to the third power dependence on particle size but it has the added benefit

of being able to image smaller particles than light microscopes. The shorter wavelengths of x-rays have a much smaller diffraction limit and the high intensity of modern x-ray sources means that the Bragg diffraction from crystals as small as 30nm can be seen. For dynamic studies, the time resolution is limited by the intensity of the beam as a certain number of photons must be diffracted by the crystal in order to get a signal large enough to be recorded on the imaging camera or solid state detector.

2.2.1 Diffracted X-ray Tracking

One of the first to determination the orientational motion using Bragg Diffraction of crystals was Sasaki et al [20] using a technique called Diffracted X-ray Tracking (DXT) to study supercooled water with Si/Mo multilayers which are attached to the substrate with polymer rods. By tracking the Bragg diffraction, Sasaki was able to measure the rotational displacement and MSD of the particle. The motion of the Bragg reflection from these multilayers was tracked using a white beam x-ray synchrotron source and the diffracted intensity was tracked both around and perpendicular to the powder ring. Using purely viscous theory which looks only at the slope of the MSD vs time curve and doesn't consider the separate storage and dissipative components of the liquid, diffusion constants of $1.7 mrad^2/s$ at 293^oC to $7.7 mrad^2/sec$ at 252^oC were extracted from the data and the viscosity of the liquid can be determined and shown to agree with literature values.

In addition to using DXT to measure the viscosity of a liquid medium, nanocrystals can also be used as a tagging mechanism to study the motions of biological systems. Sasaki used [21] Si/Mo multilayers attached to single DNA molecules to determine the dynamics of the DNA in real time. This technique chemically attached 25nm thick Si/Mo multilayers to single DNA strands which were in turn attached to a Au/quartz substrate. The diffusion constant of the system was again determined and from these values, information about structural changes in the DNA can be studied.

2.3 Facility

The diffraction experiments were done at the Advanced Photon Source(APS) at Argonne National Lab. The APS is a third generation x-ray source which means it is a dedicated high energy storage ring optimized for beam emittance. Emittance, along with brightness, is the figure of merit which characterizes an x-ray source. Brightness is defined as

$$Brightness = \frac{Photons/sec}{(mrad)^2(mm^2 sourcearea)(0.1\% bandwidth)} \tag{2.12}$$

and emittance is the product of the source size σ and the divergence σ'. σ and σ' form a phase space for the electron beam and thus, according to Liouville's theorem, the emittance for a synchrotron storage beam is a constant for a storage ring. The ratio of the vertical and horizontal emittances is called the coupling of the beam. The ratio of the source size to the divergence $\frac{\sigma}{\sigma'}$ is called the beta value and different beta values are better suited for different types of experiments. Experiments requiring good coherence benefit from a low beta value because the coherence is related to the source size while experiments requiring good energy resolution are helped by a high beta value.

First generation sources were parasitic sources which operated off high-energy physics facilities on the principle that an accelerating charge radiates. These sources used the accelerated electron or positron beam and injected them into a storage ring which used magnets to maintain a circular trajectory where the radiation is emitted tangent to the beam path.

Synchrotron radiation can be understood by Larmor's formula which describes the energy emitted from a moving charge. The fields from a particle moving at relativistic speeds where retarded times and potentials must be considered are given by the Lienard-Weichert Potentials and the result is that the energy loss has a dipole form. This dipole form has two symmetric lobes in the rest frame of the charged particle. For a beam of charged particles where the acceleration is perpendicular to the velocity, the Lorentz contraction has the effect collapsing the axis to a cone with an opening angle inversely proportional to γ. This gives

a narrow cone of radiation tangent to the path which at relativistic speeds has very little diveregence

Since the stored beams used for high energy physics research were not ideal for producing x-ray beams most suitable for condensed matter, chemistry, and biological research, second generation sources were built which were dedicated for synchrotron radiation production. Shortly after second generation synchrotrons were just coming into operation, it was discovered that insertion devices such as wigglers and undulators could greatly improve the brightness coming from just the stored electron beam itself. This improvement comes from putting insertion devices into the straight sections of the storage ring where the insertion device can reduce the horizontal divergence of the beam. The wigglers and undulators are able to reduce the divergence by oscillating the electron beam in the horizontal plane using an array of magnets with alternating polarities.

The Advanced Photon Source at Argonne National Lab is one of the first of 3 third generation sources built. It is a 1104m circumference storage ring of 40 straight and bent sections with a linear electron accelerator operating at 7GeV with an emittance of 3.1nm-rad and a coupling of 1%. There is typically 102mA of stored beam. The beamline used at 34ID-C is an undulator beamline optimized for coherent difraction, accomplished by minimizing the number of optics in the beam path as all optics effect the coherence of the x-ray beam. The x-rays produced directly from the electron beam in the storage ring is a broad spectrum x-ray beam with a horizontal angular divergence of order $10^{-5} rad$ depending on the ring energy. An undulator insertion device reduces the horizontal divergence by forcing the electron beam to undergo sinusoidal oscillations in the horizontal plane. The intensity is increased due to the addition of the radiated intensity at each of the arcs and thus the intensity enhancement is $2N$ where N is the number of periods. Additionally, the period of the magnets in an undulator is such that the radiation from one period is in phase with subsequent periods. Undulator radiation is quasi-monochromatic with a divergence much smaller than bending magnet radiation. The gap of the undulator may be adjusted to change

the energy spectrum to get the peak intensity at the desired energy.

3

Chapter 3

Experiment

3.1 Beamline components

The beamline at 34ID-C is a parasitic coherent x-ray diffraction beamline which operates in conjunction with 34ID-E. A beam splitting mirror is used to split off a section of the undulator beam in the outboard direction into the 34ID-B hutch. X-ray diffraction experiments typically require monochromatic x-rays and those are produced with a double bounce silicon (111) monochromator. The monochromator at 34ID-B sits 5 meters upstream from the sample position and uses the 111 Bragg reflection from the first crystal silicon block to pick out a set energy at an angle where it will obey the Bragg reflection condition for the second crystal as well. This monochromator has an energy resolution of 1eV at 8keV beam energy. The beam is then reduced in size by two sets of slits, the first of which are a pair of L shaped slits. The second set of slits are a pair of two parallel cylinders who cut the beam by rotating about the axis parallel to the cylinders and perpendicular to the incident beam.

To image crystals less than a micron in size sufficiently quickly that the dynamics can be determined, it is necessary to increase the flux of the undulator x-ray beam. This is accomplished via a Kirkpatrick-Baez elliptical focusing mirror pair. The mirrors are trapezoidal blocks of platinum coated silicon which can be bent individually on either end to form tunable focusing mirrors. They are 10cm in length with a focal distance of 5cm from the end of the second, horizontal focus mirror. The beam is incident at 3mrad which is less than the critical angle of platinum and assures total external reflection. The mirrors in practice focus 63% of the incident intensity to a spot size of 1-3 microns, giving a factor of approximately

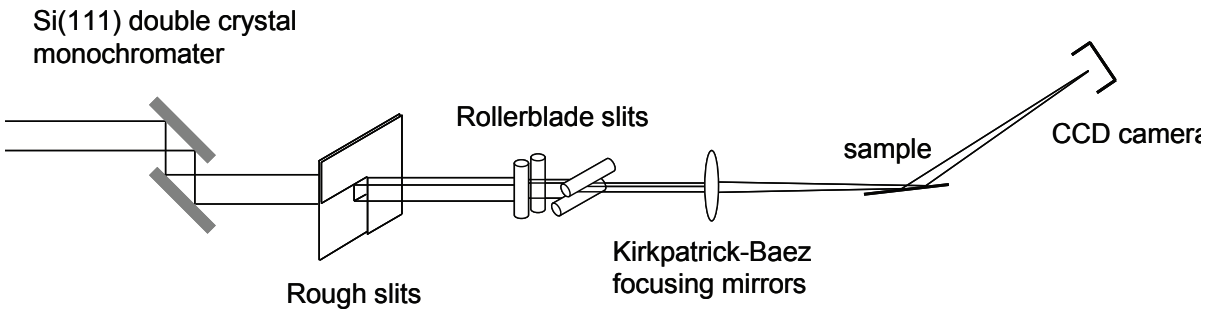

Figure 3.1: Schematic of the beamline at 34ID-C after the undulator and beamsplitting mirror, approximately 52m from the undulator.

2000 if used in both the horizontal and vertical directions with a 100x100 micron incident beam. The usable focusing length is 8cm due to the rollers which bend the mirrors on either end.

3.2 Sample stage

The sample is placed on a water coolled copper stage with a peltier heater. A schematic of the copper stage is shown in figure 3.2. The stage is quick flange compatible with a partially threaded channel which is connected to a constant temperature water source. A peltier heater is attached to the copper stage with a silver nanoparticle/epoxy mixture to increase the thermal conductivity between the peltier and water cooled copper. A thermocouple is similarly attached to one corner of the top face of the peltier. The thermocouple wires are connected to alligator clamps which are used to connect the thermocouple to the feedthrough. A KF-40 O-ring is used to connect the coppper bottom to a tee junction which has two rectangular windows cut out and covered with kapton for the incident and diffracted x-rays. The smaller window is meant for the incident beam due to the need a window just large enough to align the beam with the sample position. The opposite window is larger because of the need for a large range of scattering angles to access several Bragg reflections of a variety of powders. The kapton window is attached to the tee junction using slow curing

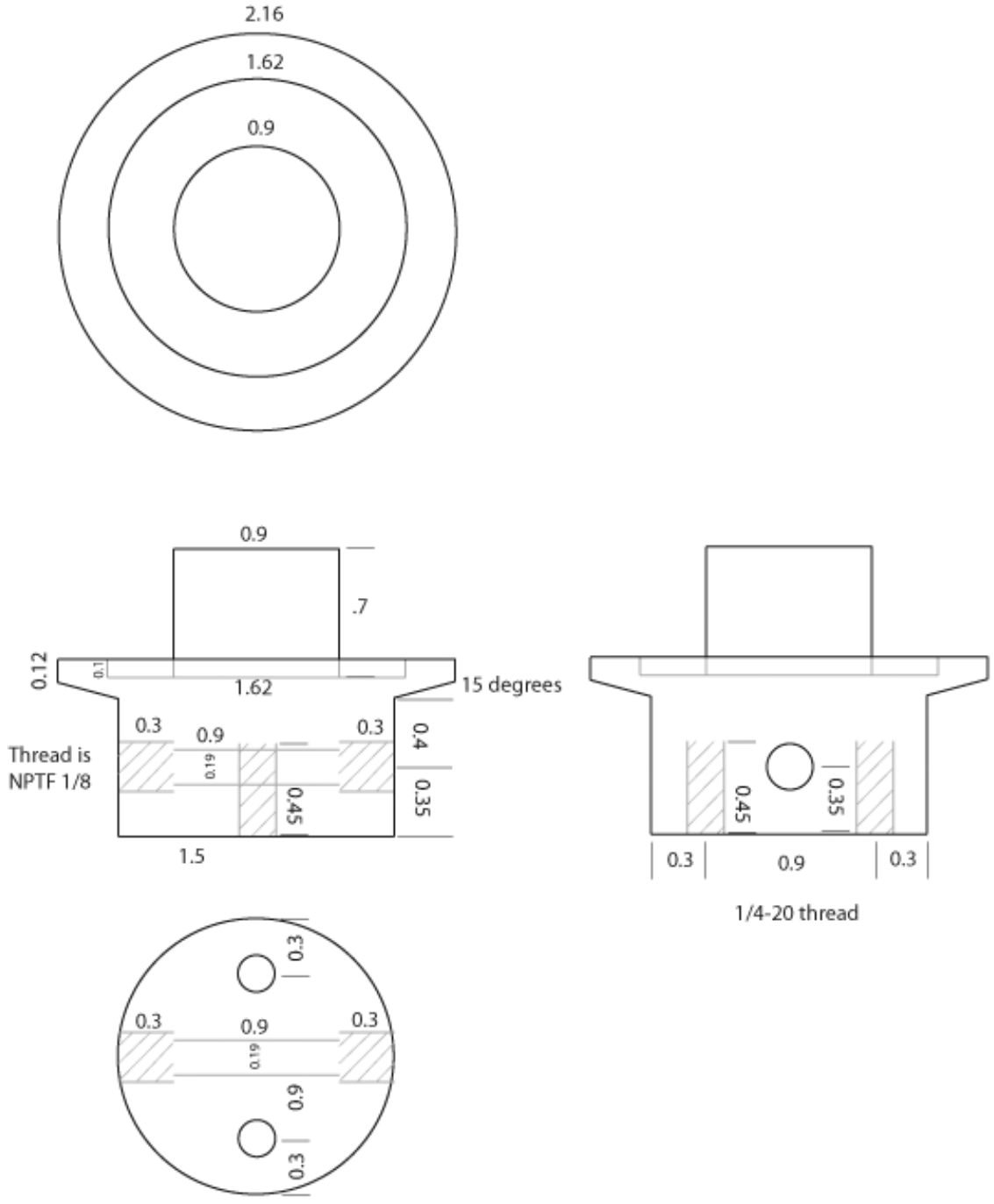

Figure 3.2: Schematic of copper stage with all measurements in inches.

epoxy. To attach the window, a piece of epoxy large enough to cover both widows is cut and the areas which will be in contact with the metal are roughened with sandpaper for better adhesion. The tee junction must be clean of any dirt or previous adhesives and the two are glued according to the curing instructions for the individual epoxy. The four conductor feedthrough is attached to the tee junction via a conflat connector.

To mount the sample, thermal paste is put onto the peltier stage and the substrate is pressed into the thermal paste to ensure good thermal contact. Care must be taken to not allow thermal paste near the incident or diffracted beam as thermal paste contains Alumina crystals which will have diffracted intensity which will confuse the data from the sample itself. The tee junction is then placed on the copper piece with an O-ring and quick flange clamp. From the top view, the feedthrough should be facing inboard to the ring or pointing away. The power conductors are on the right and the thermocouple connects are on the left if facing the storage ring as shown in figure 3.3 where the storage ring is to the left side of the page. To connect the power source to the peltier wires, alligator clips are used to connect the peltier wires to the power feedthrough conductors at the top of the tee. The length of the wires are cut to match the height of the feedthrough connects. Care should be taken to not have any shorts in the circuit as a significant amount of current will be used for the peltier. Figure 3.4 shows the sample stage mounted on the goniometer.

The sample cell is suitable for roughing pump pressures and can be connected using quickflange connectors. To use the cell in vaccum, a reducer is used to connect the cell to a pressure valve. The valve can then be connected to a roughing pump to put the sample under vacuum. Vibrations from a roughing pump will affect the accuracy of a measurement so the best option is to put the system under vacuum and disconect the pump from the sample stage as the experiment is being performed.

The chilled water from the Advanced Photon Source or from the NESLAB chiller is used as the constant temperature water source and is connected to the sample cell. The power feedthrough is connected to a voltage source via an adapter and the power source

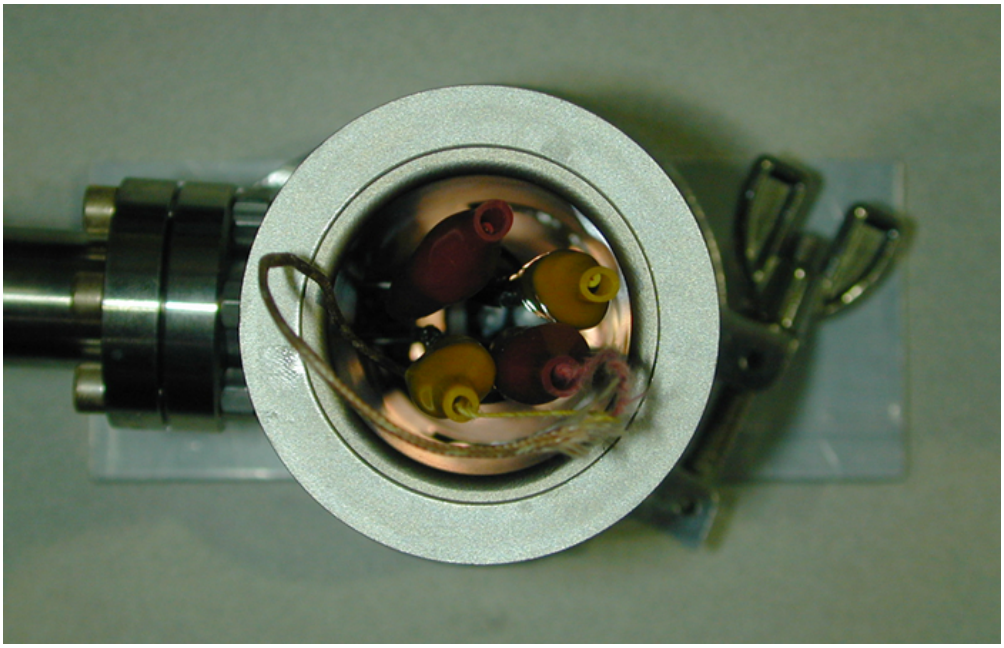

Figure 3.3: Top view of the connected sample cell. The feedthrough of the tee junction is to the left. The two top alligator clips connect the top feedthrough posts to the peltier wires. The bottom alligator clips are permanently connected to the thermocouple wires and are manually connected to the bottom feedthrough posts.

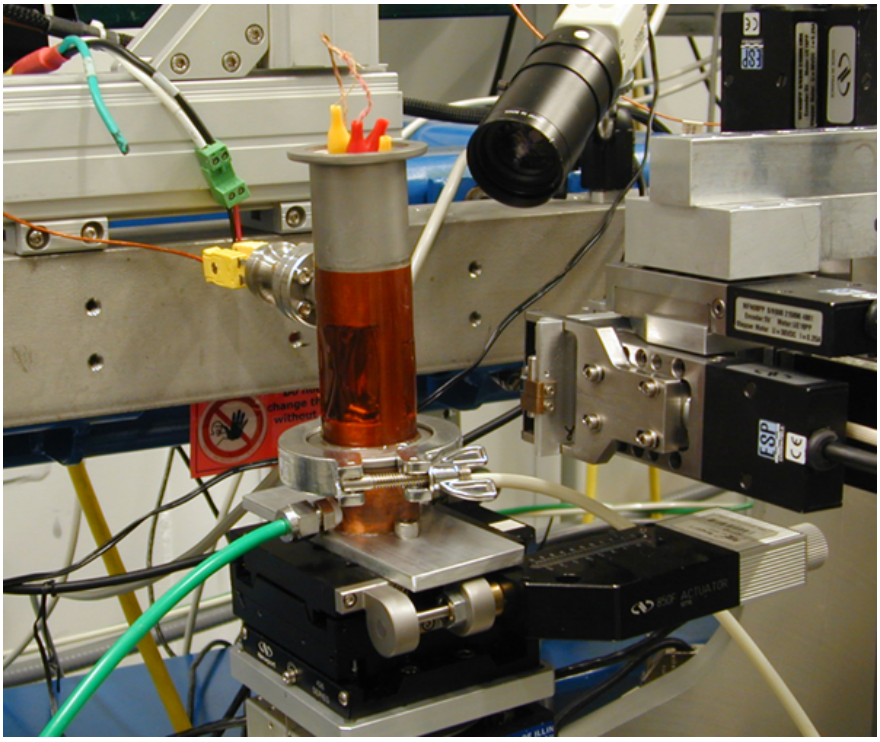

Figure 3.4: Sample cell on the 34ID-C goniometer with power connector (green) and thermocouple connector. The water cooling tubing in white and green are connected to a constant temperature water source. The K-B mirrors are mounted to the right (upstream).

wires can be switched depending on whether the sample needs to be heated or cooled. The power feedthrough wires can sustain a voltage of approximately 3V and 1.5Amps which defines a temperature range of approximately +/- 30C with respect to the copper sample stage temperature, most commonly the temperature of the constant water source which is approximately 10^oC for the chilled water source from Argonne and programmable from 2^oC to 12^oC for the NESLAB chiller due to the need to connect the sample stage in series with the CCD camera. For temperatures below 15^oC, condensation will be a factor and it is important to evacuate the cell to avoid these effects. The temperature read by the thermocouple is not necessarily the sample temperature because the thermocouple is attached to the peltier and thus sits below the sample substrate.

Two different shuttering methods may be used to change the radiation dose imparted to the sample. One is to shutter the camera using the iris that is provided with the detector.

This method ensures that there is a constant radiation dose to the sample. The other method is to put a beam shutter on the incident beam which reduces the total radiation dose to the sample. The beam shutter is synchronized with the detector readout and is important for radiation sensitive samples.

3.3 Detector

The detector used to collect the diffracted intensity is a Princeton Instruments PI-LCX direct detection charge coupled device (CCD) with an ST133 or ST138 controller which interfaces with a software package WinView32 which records the data in a Winview specific data file type called SPE. The CCD chip has 1024x1138 20.5x20.5 micron pixels. There is a camera or beam shutter which is synchronized with the camera and allows the CCD to read out between frames.

The CCD used on 34ID-C is a direct CCD which means that when a photon hits the chip, a cascade of electron-hole pairs is created in a region of the chip. The chip is biased in a way to discourage recombination and the electrons can be read out to determine the number of photons impinging on that pixel of the detector chip. CCDs read out by transfering the charge created by an x-ray by sequentially depleting the charge from one pixel to a neighboring pixel along the register. Once the charge reaches the end of the chip, it goes through an analog to digital converter (ADC) which converts the charge to an intensity.

There are two readout modes which this type of transfer supports. One is a full frame readout in which the entire region of interest (ROI) is read before another image is taken. That mode has a readout time dependent on the size of the image. Another readout mode is Kinetics mode where a portion of the CCD is physically or optically masked. This mode tranfers data from the exposed region underneath the mask. Depending on the width of this region, the tranfer time can be a fast as a few microseconds. The chip must be masked such that the exposed region is at the beginning of the chip with regard to the readout direction.

In WinView, the readout mode is set to Kinetics and parameters are entered for the Kinetics Window size and the vertical shift rate (in units of $\mu sec/pixel$). The window size is the size of the image perpendicular to the read out direction, the other dimension is defined by the ROI in the Experimental setup window. The Vertical shift rate is the time it take to transfer one line of pixels under the mask. The time for one image to be read out is equal to this vertical shift rate multiplied by the Kinetics window size. The number of images that can be taken in one frame is the size of the ROI parallel to the register divided by this Kinetics Window size. The readout time of the entire frame again depends on the size of the ROI. Only the ST138 controller supports Kinetics Mode readout natively, the ST133 controller has a Kinetics package which must be purchased to use this feature.

3.4 Sample

3.4.1 Fatty Acids

Fatty acids are amphiphilic carboxylic acids with a hydrophobic alkyl end as well as the hydrophilic carboxyl end group. Commonly found in nature in a variety of food sources, they come in a saturated (with Hydrogen) form with only single bonds and no functional groups and an unsaturated form with double bonds and/or functional groups. A convenient shorthand notation tells the number of carbon atoms : the number of double bonds, ie C8:1 is a fatty acid with 8 carbon atoms and one double bond. When there is a double bond present, there are two conformations which exist. One is the trans configuration where the carbon atoms are on opposite sides of the double bond. These are straight chain fatty acids similar in structure to saturated fatty acids. The other conformation is the cis where the carbon atoms are on the same side of the double bond. These fatty acids are typically bent which affects the rigidity, packing and melting points. The most common fatty acids in nature are hexadecanoic which comprise 20-30% of the lipids in animal tissue and 10-40% in plant oils. Octadecanoic acid is the second most prevalent fatty acid found in animal tissue,

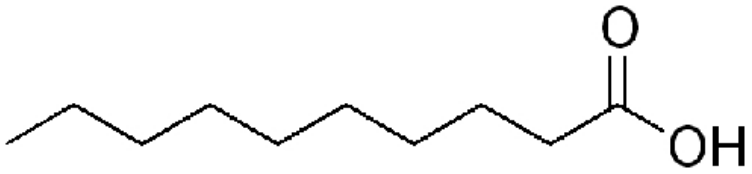

Figure 3.5: Decanoic acid with an alkyl group and carboxyl group.

many milk fats and cocoa butter. The main biological role of fatty acids is understood to provide rigidity to membrane walls though there is still much to be understood about the role of fatty acids in biological funtions.

Due to their amphiphilic character given by their end groups, fatty acids self assemble into micelles, wormlike micelles and lamellar structures in solvent/salt solutions[cmplx-review]. They have a melting temperature which increases with molecular weight but has an even-odd behavior depending on the number of carbon atoms. The more common even numbered fatty acids have a higher melting point than odd numbered carbon acids. Octanoic acid has a density of $0.910 gm/cm^3$ and decanoic acid has a density of $0.893 gm/cm^3$ at 25^oC. Fatty acids have a temperature dependent absolute viscosity that was measured by standard rheological techniques and found to be generally 0.3 to 7 cp for 2-19 carbon chains at temperatures between $20 - 70^oC$[**?**].

The glass transition of a material is defined as the temperature at which the viscosity diverges (ie greater than 10^{13} poise)[2]. It is a second order phase transition that occurs for amorphous materials at which the kinetic energy of the system is less than the bond energy and molecular motion ceases. It differs from melting which is a first order phase transition for crystalline or crystalline portions of materials and generally leads to an abrupt and discontinuous volume change at the melting point where the material forms a crystalline lattice. The glass transition can be very narrow or broad depending on the material. For fatty acids, the glass transition temperature increases with the chain length.

For polymeric materials, the glass transition can be most easily quantified by the thermal expansion coefficient α and the free volume. For most liquids, there is a substantial quan-

tity of free volume or empty space where the molecule may undergo thermal motion and arrangement. Free volume is a poorly defined quantity but is a measure closely related to the mobility of the molecules which change with temperature. At high temperatures, where Brownian motion is very rapid, the free volume decreases very quickly with temperature and at low temperatures, it decreases more slowly until the point where the material cannot contract any longer. At this point, α undergoes a discontinuity and that point where the volume of material no longer depends on temperature is the glass transition temperature. Efforts have been made to define the glass transition in terms of shear deformation, entropy and enthalpy but the former is a far less precise definition because it must sample all the softening, rubberlike and brittle temperatures while the latter two are difficult to determine experimentally.

3.4.2 Hydrocarbons

Hydrocarbons are organic molecules composed entirely of hydrogen and carbon which are hydrophobic. As with fatty acids, they come in a saturated and unsaturated form and can have carbon rings (cycloalkanes) or aromatic rings (aromatic hydrocarbons). They have a glass transition, which, like fatty acids, increases with the length of the chain length. The sample used was soft paraffin, also known as petroleum jelly or petrolatum which is a mixture of saturated hydrocarbons typically with chain lengths longer than 25 carbon atoms. Soft paraffin has a glass transition in the vicinity of 37^oC depending the exact ratio of the different chain lengths. It has a density of $0.92gm/cm^3$ and a viscosity of 6-25cSt at 100^oC.

3.4.3 Alumina

Alumina, Al_2O_3, comes in many forms the most common of which is α-alumina, also known as Corundum. It is commonly used as an abrasive due to its hardness which is 9.0 on the Mohs hardness scale. It is rhombohedral with a space group of R-3c. In the equivalent

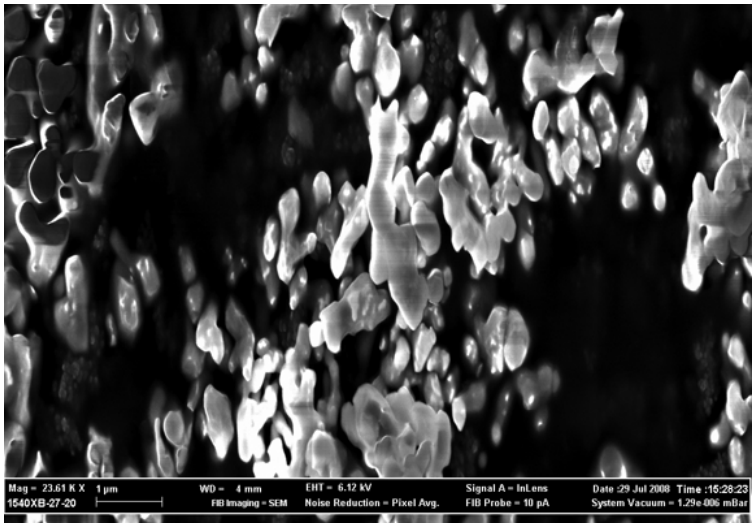

Figure 3.6: SEM image of 300nm alumina nanopowder

hexagonal lattice, the lattice vectors are $a_{hcp} = 4.758\mathring{A}$ and $c_{hcp} = 12.99\mathring{A}$. The primitive lattice vectors are $a = 3.621\mathring{A}$ and $b = 0.257\mathring{A}$ with an angle of 55.5^o between the vectors. The powder diffraction pattern of α-alumina is shown in figure 3.5 [28]

Fatty acids of varying chain lengths have been observed to adsorb onto the surface of Alumina nanoparticles [29]. The nanopowders had a mean radius of 50nm and a range of radii between 10nm and 400nm and the fatty acids studied were propionic (C3:0), heptanoic (C7:0), pentanoic (C5:0), and oleic acid (C18:1 cis-9), the main ingredient in olive oil. Bell et al studied the effects of fatty acid stearic layer thickness on the rheological properites of alumina suspensions. The alumina can therefore be assumed to be sterically stabilized by the fatty acids and aggregation is reduced. In preparation of various fatty acid, alumina, solvent and salt solutions, the alumina was observed to be very soluble in the fatty acid, causing the alumina to phase separate from water due to the insolubility of the fatty acid adsorbates.

Hydrocarbons have also been observed to adsorb onto the surface of alumina [30] [31]. The first study showed chain length ($n-C_{31}-nC_{39}$) and slightly longer chain length ($n-C_{36}-nC_{43}$) hydrocarbons adsorbing onto an alumina catalyst with the longer chain hydrocarbons

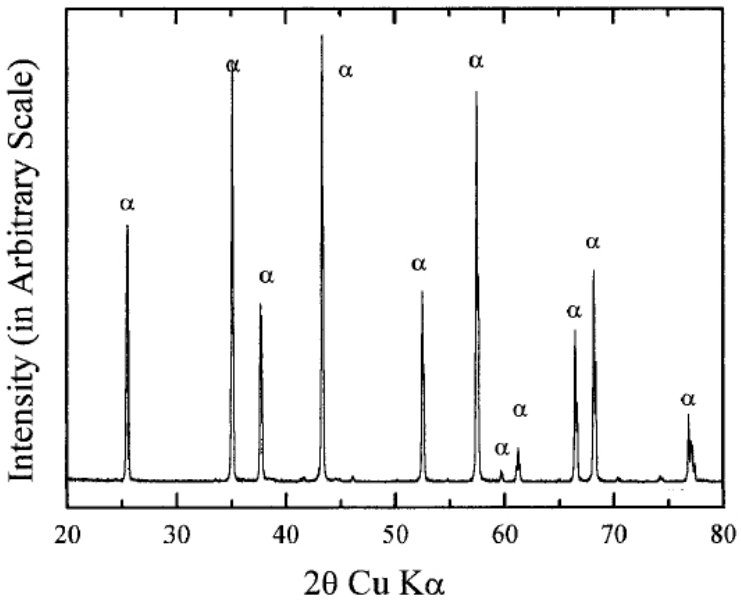

Figure 3.7: X-ray Diffraction powder pattern of $\alpha - alumina$

adsorbing more effectively. The second study showed short chain hydrocarbons such as ethane, butane, hexane and benzene to adsorb onto alumino-chromium catalyst containing 90.8% alumina. This indicates that the alumina in the soft paraffin sample is also sterically stabilized.

Adsorption is a process that arises from the property that atoms on a surface have surface energy requirements that are not filled by surrounding atoms as they are in the bulk. Adsorption is typically driven by weak van Der Waals forces (physisorption) or covalent forces (chemisorption). There are many models of adsorption, the simplest being the Langmuir model which assumes that at most, only one monolayer is adsorbed onto the surface of a adsorbent. There are cases of multilayer adsorption, however, and those can be modelled by the Brunauer Emmet Teller (BET) theory which treats all successive layers equally but differently from the first adsorbed layer. Adsorption is a very temperature dependent process, studies indicate that increasing temperature has the effect of increasing the amount of polyvinyl alcohol (PVA) and polyethylene glycol (PEG) adsorbed onto 496nm alumina nanocyrstals[40] due to increased thermal energy causing less adsorption sites on a single

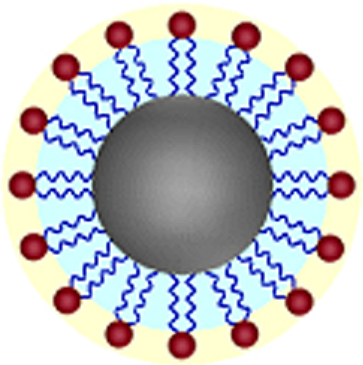

Figure 3.8: Decanoic acid adsorbed onto an alumina crystal with the hydrophobic alkyl end adsorbed onto the surface.

molecule leading to a more stretched adsorption conformation and denser packing of adsorbates. The same study found that the length of the adsorbate was shorter than the species in the bulk because of multiple adsorption sites.

Another factor is the adsorption/desorption rate and the retention time of a adsorbate species. These dynamics can be important if the adsorption has an effect on the dynamics of the alumina particle. Studies of adsorbed polymers on latex spheres shows that the adsorbate density depends on time and can be seen to decrease over minutes[41]. The retention time of species with long chain lengths is longer than that of shorter chain lengths because of the need for the release of many adsorption sites in a single molecule for molecule to completely desorb from the surface.

3.5 Paints

Paints were also studied using X-ray Bragg diffraction because paints are a common and widely used material that contains crystalline nanoparticles in suspension. Paints are typically composed of a polymer or resin binder which is used to protect or seal the surface to which it is applied, a solvent or diluent which aids in the application of the paint, additives which are minor components and are used for a variety of purposes - as catalysts, driers, flow

agents, etc, the primary pigment which provides the opacity/color/other optical effects, and the extender which is used for variety of purposes such as opacity, structural properties[38].

Paints typically dry by two mechanisms, atmospheric oxidation or the evaporation of the solvent and a coalescence of latex particles in the binder. Some paints need the application of heat or radiation to crosslink polymers in the liquid phase into a highly crosslinked solid. The main primary pigment material in modern use is titanium dioxide which is a suitable material to study with x-rays because the need for high quality pigment particles has driven industry to produce titanium dioxide particles with good crystalinity and size distribution.

3.6 Experiment

A mixture of fatty acid (decanoic or octanoic) or hydrocarbons and tracer particles (Alumina Al_2O_3 or Titania TiO_2 or silver) were prepared in a 8% volume fraction ratio. For both fatty acids, the solution was prepared at above the melting point of the fatty acid. Each solution was sonicated for 6 hours minimum at above the melting temperature to ensure a minimum of agreggates. $3\mu l$ of the solution was deposited on a hydrophobic substrate. Depositing decanoic acid onto a substrate involves heating the solution at high enough temperatures such that it stays liquid for a sufficiently long time to be pipetted onto the substrate. It should be pipetted in a timely manner so that it does not cool to lower than its melting point before it is deposited. Some sedimentation will occur due gravitational effects.

As colloids settle due to the force of gravity, there are two regions of interest, one is the sediment which are the particles sitting at or near the substrate. The other is the suspension which are particles free to move via thermal energy in the liquid. For a small particle suspended in a liquid, Stokes law describes the drag force exerted on a particle by a viscous fluid. Stokes law for a spherical particle is

$$F_d = 6\pi r\eta V \tag{3.1}$$

where F_d is the drag force, r is the radius of the particle, η is the fluid's dynamic viscosity and V is the particle's velocity. This equation defines a terminal velocity for a particle settling in a liquid driven by gravitational forces as

$$V_t = \frac{2}{9} r^2 g \frac{(\rho_p - \rho_f)}{\eta} \tag{3.2}$$

where V_t is the terminal velocity, r is the radius, ρ_p and ρ_f are the density of the particle and fluid and η is the viscosity. Stokes law describes the settling forces of a particle under a stationary force and the actual sedimentation behavior in time is given by the Mason-Weaver equation, a partial differential equation based on Stokes law and exactly solvable to determine the time evolution of the sedimentation profile. The equilibrium profile can be given by the long time sedimentation profile given by the Mason-Weaver equation or more simply and classically by barometric pressure. It was the observation of the exponential density profile that led Jean Perrin to first deduce Boltzmann's constant and Avogadro's number. For more dense particle concentrations where interparticle interactions must be taken into account, the treatments are more complex and varied.

The sample was placed on the peltier sample stage with thermal paste and the thermocouple and power feedthroughs were connected. The entire stage was attached to the translation stages which sits on top of a goniometer. The CCD camera was placed at a distance of approximately 0.6m from the sample. X-ray energies of 8-11keV are preferrable for the diffraction experiment. The x-rays are incident through the sample in translation geometry. It is possible to determine the location and dimensions of the droplet by looking at the attenuation and refraction of the x-ray beam through the fatty acid. The CCD was placed at the (1 0 4) Bragg angle of Alumina or a 2θ angle of 31.34^o at 9KeV.

In order to maintain reasonable file sizes, a narrow region of interest (ROI) was selected, with a width just large enough to accommodate the width and curvature of the powder ring. The CCD is typically placed close to the horizon and the CCD is rotated such that

the powder ring in approximately vertical and a narrow rectangular ROI may be defined. The angular resolution is determined by the binning of the CCD and the sample-detector distance. With the standard setting of 2x2 binning and a sample to detector of 0.6m, the angular resolution is $80\mu rad$. A time set was chosen in either full frame or kinetics mode and a number of frames was chosen to yield a manageable file size. Care must be taken to manually record the acquisition time of each file because the ST138 controller does not automatically log the acquisition or read out time of the files. To decrease the readout time, the CCD should be mounted such that the readout direction is horizontal. With a narrow ROI, reading out along the short dimension will greatly increase the speed that frames can be read.

For the Kinetics mode data, the exposure time, window size and frame size must be chosen so that the read out time is not longer than the acquisition time for each frame. The ensures that there are no missing lag times because data from adjoining frames can be used to calculate lag times longer than the exposure time multiplied by the number images per frame. The lower statistics of times longer than the number of images multiplied by the exposure time is such that only times within a single frame of data is valid.

Due to the sedimation profile, the 8% volume fraction in the droplet is only an average and the height of the sample is chosen such that there is a reasonable density of diffracting particles. Very low in the droplet, the density is too high to isolate the motion individual particles and too high in the droplet, there are too few particles that the time to find a particle makes the expriment prohibitive. The optimal height is where there are 4-8 diffracting particles in the ROI. This corresponds to the 8% volume fraction which is the packing fraction of the original solution.

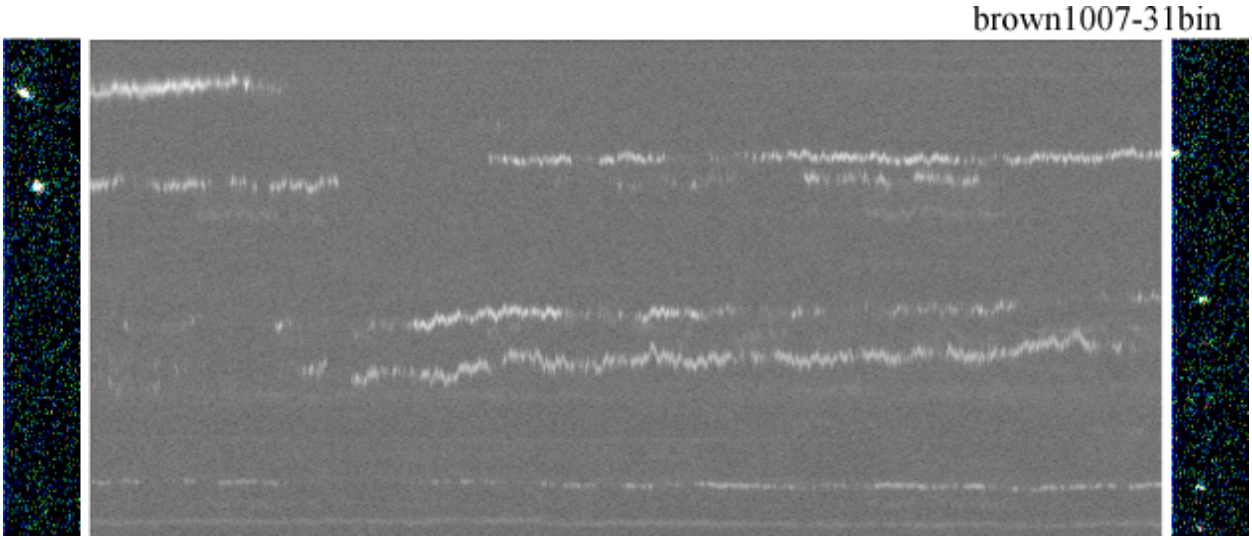

Figure 3.9: Example of raw and plotted Full Frame data. The raw data, right and left, is Bragg diffraction intensity along the powder ring. The raw data is binned accross the powder ring and each frame corresponds to a single column in the plotted data.

3.7 Analysis/Programs

Once the data is obtained, the data is processed so that trajectories can be manually selected for tracking. For full frame data files, the files are binned across the powder ring (x direction) to yield a data set that is 1 x y x frames. This data is then plotted using 2dplot in two-dimensions to obtain an image of angle versus time. A typical data set is shown in figure x. For kinetics mode data, the data must be binned in the x direction in accordance with the window size chosen when the data was obtained. The binned data set then has the time axis running in the negative x direction and it must be flipped in x and then combined with the other frames to obtain the correct trajectory. An example of this procedure is shown in Figures 3.3-3.4. The program which does this is spe_read.c which reads in an SPE file in kinetics mode and produces an sp4 file with the proper inversion of in the x-dimension and combines all the times to create a single image for a kinetics mode data file. The kinetics mode data also has segments of missing data as each frame reads out but that is not accounted for the the initial conversion of the data from SPE to sp4 format.

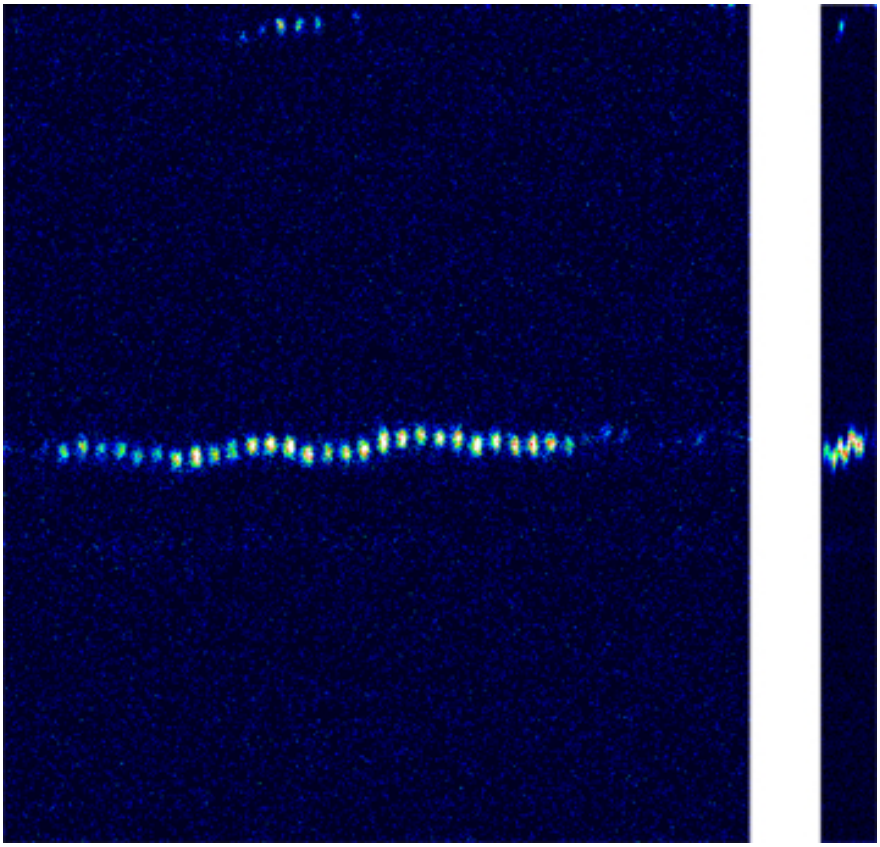

Figure 3.10: Example of raw and binned data for Kinetics Mode data. The above example has a window size of 25 pixels in the horizontal and a frame size of 1000 pixels, giving 40 time steps per frame. The data is binned to obtain a frame 40 pixels wide with the time axis running right to left.

Figure 3.11: Example of plotted Kinetics mode data. The binned frames are inverted so that the time axis runs left to right and are combined to obtain a plot of the data similar to Full Frame data. The readout time of each frame which would contribute 25 empty pixels after every 40 pixels of data are not included in this plot.

Individual trajectories are then chosen from the complete plotted data sets. For the full frame data, the actual particle is identified in the original SPE datafile and a new SPE datafile is created by chosing a region on interest and number of frames which just contains the particle in its trajectory. The much smaller region of interest is again binned in the x-direction but the region must be sufficiently large that the center of mass off the particle is at least 2 pixels away from an edge. The cropping serves to eliminate noise and interfering diffraction from other particles which may be at a slightly different 2θ but the same position on the powder ring. These particles are at a different positions along the incident beam and thus diffract at a slightly different angle. Suitable trajectories are ones which contain at least 500 trackable positions with a large percentage of adjoining data points and do not have stray diffraction which cannot be eliminated by cropping.

For kinematic mode data, the trajectory is isolated not by creating a new SPE file but rather by cropping the sp4 file to the dimensions of the trajectory. In image editor software, the bounds of the trajectory in y and time can be found. By then using the 2dcrop program, a new sp4 file with those dimensions is created. That sp4 file is then plotted to obtain an image which can be compared to the tracked trajectory and tracked using the tracking programs.

The programs can manage missing data so the chosen trajectories can include particles which rotate out of diffraction for some frames. The new SPE files are then replotted to check the y-dimension and frames. The new SPE files are tracked using brownian11. Brownian11 takes ASCII data which is created by using the SPE to ASCII conversion tool in Winview. In the options window, it is important to preserve the x/y/frame dimension value and that the delineator is a comma. The tracking programs begins by manually chosing an intensity cutoff for particle intensities by finding the lowest intensity pixel of a user chosen percentage. This serves to allow the handling of noisy data by only considering particles having greater than a certain intensity. Using a percentage is preferable than a numerical intensity cutoff because datasets will vary depending on the intensity of the incident beam, noise from scattering

through different samples and other experimental factors.

The program then considers the sum of five adjacent pixels in each frame and chooses the center pixel of the grouping of five as the position of the particle. If the summed total intensity is greater than five times the cutoff intensity chosen, then the position of that frame is considered. Otherwise, there is no tracked position for that frame. The cutoff intensity should be individually chosen for each trajectory though 20 is typically a good starting value. A suitable cutoff intensity is determined by both the noisiness of the data but also by the size of the image. A large image where the maximum displacement of the particle is large will have more background pixels than an image of a trajectory where the particle does not have a large maximum displacement. A few iterations are typically necessary to yield a good tracking result. The time steps are the sum of the exposure time and the readout time.

The kinetics mode data is tracked using the same tracking algorithm but tracks the .sp4 format data instead of an ASCII file. In addition, segments of missing data are included to account for the readout time of each frame once a threshold is found. To compare with the trajectory which does not have the missing data, a version of the tracking program which does not have the gaps is used - track4. The number of missing data points per segment is calculated by dividing the readout time by the sum of the exposure time and shift time per image. Track3 is the final program used to create the datafile of tracked points which will be used by the program used to calculate the MSD.

The tracked image is then checked and select points may be deleted that correspond to strong stray intensity from other particles. The MSD

$$MSD = \frac{1}{N-\tau} \sum_{i=1}^{N-\tau} (\theta_i - \theta_{i+\tau})^2 \tag{3.3}$$

of the trajectory is then calculated by a program that checks that if there is are position data points at the time lag of interest. For example, for a lag time of 3 time steps, for the 56th point, the program would check to see if there is a valid data point at the 59th time

step. If there is, the angular displacement is incorporated into the MSD calculation. The program also keeps track of the number of valid lag time pairs so it can divide by the correct number of pairs. Long lag times, ie lag times which are a large fraction such as 1/3 or 1/4 of the total time of the dataset, will have poor statistics that make the MSD displacement data invalid. The more data points, the more accurate the MSD will be.

3.8 Calculating $G(\omega)$ and the viscosity

The calculation of $G(\omega)$ from the MSD versus time data for a particle or set of particles is outlined in section 1.5 for linear motion. The angular calculation is analagous with the substitution of angular MSD in radians for linear MSD. The units are The local power law expansion about a certain frequency is local due to the the derivative of the signature of the power function, given by $\alpha(\omega)$. The numerical derivative is calculated only over a local interval about the time delay or frequency of interest. The derivative algorithm we use is the native derivative algorithm of Origin given by

$$\frac{1}{2}\left(\frac{y_{i+1}-y_i}{x_{i+1}-x_i}+\frac{y_i-y_{i-1}}{x_i-x_{i-1}}\right) \tag{3.4}$$

so only the two adjacent points are considered in the expansion. Once $G(\omega)$ is obtained, the steady state viscosity η_0 can be quickly read off by taking the low frequency limit of $G''(\omega)/\omega$ This method is demonstrated for the data published in [32] for angular MSD versus time.

In purely viscous theory, the viscosity is derived from the slope of the MSD vs lag time curve to get the diffusion constant which is a function of particle size and viscosity. The slope must be taken at times longer than the ballistic regime and there is no storage component or frequency dependence.

Chapter 4

Results

The rotational motion of tracer particles suspended in a fluid studied by x-ray diffraction consists of trajectories that resemble random walks, quickly and slowly diffusing particles with continuous trajectories and stationary particles. These behaviors can be seen in the following plots of angle versus time in figure 4.2 and 4.3. The motion observed is the rotation of a single crystal around the z axis which is normal to the scattering plane, defined as the plane containing the incoming and outgoing wavevectors k_i and k_f which in figure 4.1 is the plane of the page. The rotations around the x axis correspond to movement across the powder ring and rotations around the y axis cannot be observed by diffraction as that motion is perpendicular to the momentum transfer vector. The plots shown have axes of angle (vertical) vs time (horizontal). The angular range determined by the detector size and distance is 5.2^o with an angular resolution of $80\mu rad$, proportional to the angle of scattered light incident on one pixel of the detector. For figures 4.2-4.14 there are a total of 2000 frames or time steps and the time resolution is 0.6sec per frame which includes detection time and readout.

A rigid, ideal particle has 6 degrees of freedom, 3 translational and 3 rotational. The conventional probe of three dimensional Brownian motion may be considered a linear superposition of one dimensional Brownian motion and we will assume that to be true for these particles where there is not a preferred direction of rotation. This ultilization of equipartion is analagous to projecting out the height in translational single particle tracking which is a well established microrheology technique. By design of the experiment, we explicitly exclude the translational degrees of freedom because x-ray diffraction with a parallel beam is not

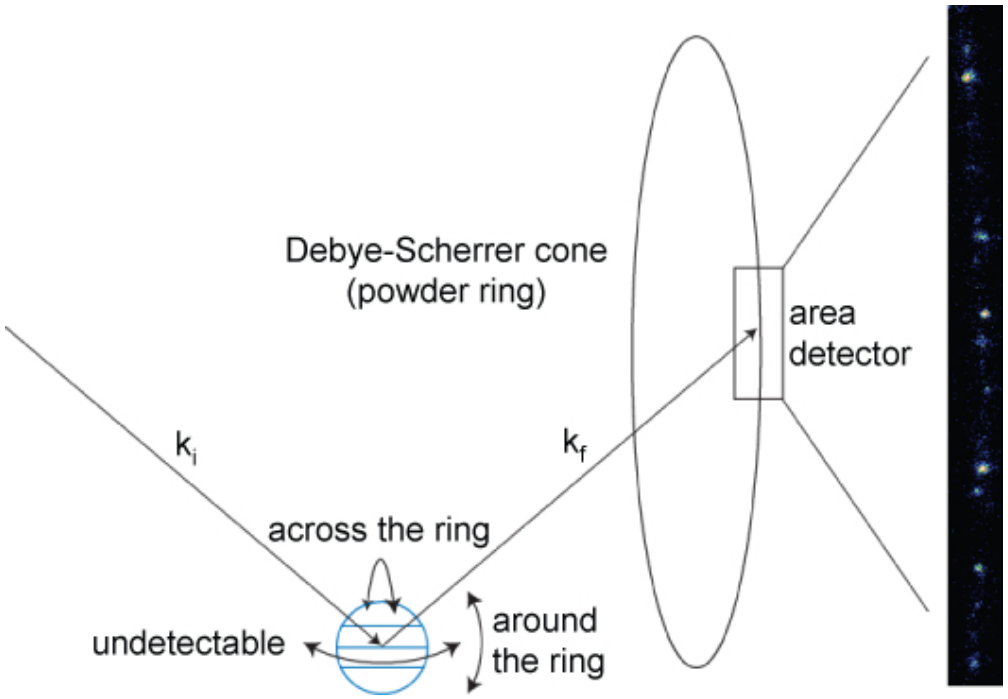

Figure 4.1: The scattering diagram for the experimental setup at 34ID-C. The incoming and outgoing wavevectors k_i and k_f define the scattering plane. The motion around the powder ring which is studied corresponds to the rotation of the crystal about the axis perpendicular to the page. An area detector records the movement of the Bragg intensity at an angle determined by Bragg's law.

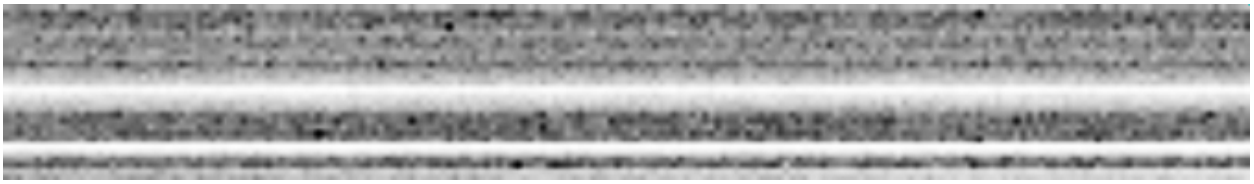

Figure 4.2: X-ray diffraction of dry $\alpha - alumina$ powder showing that the particles are stationary.

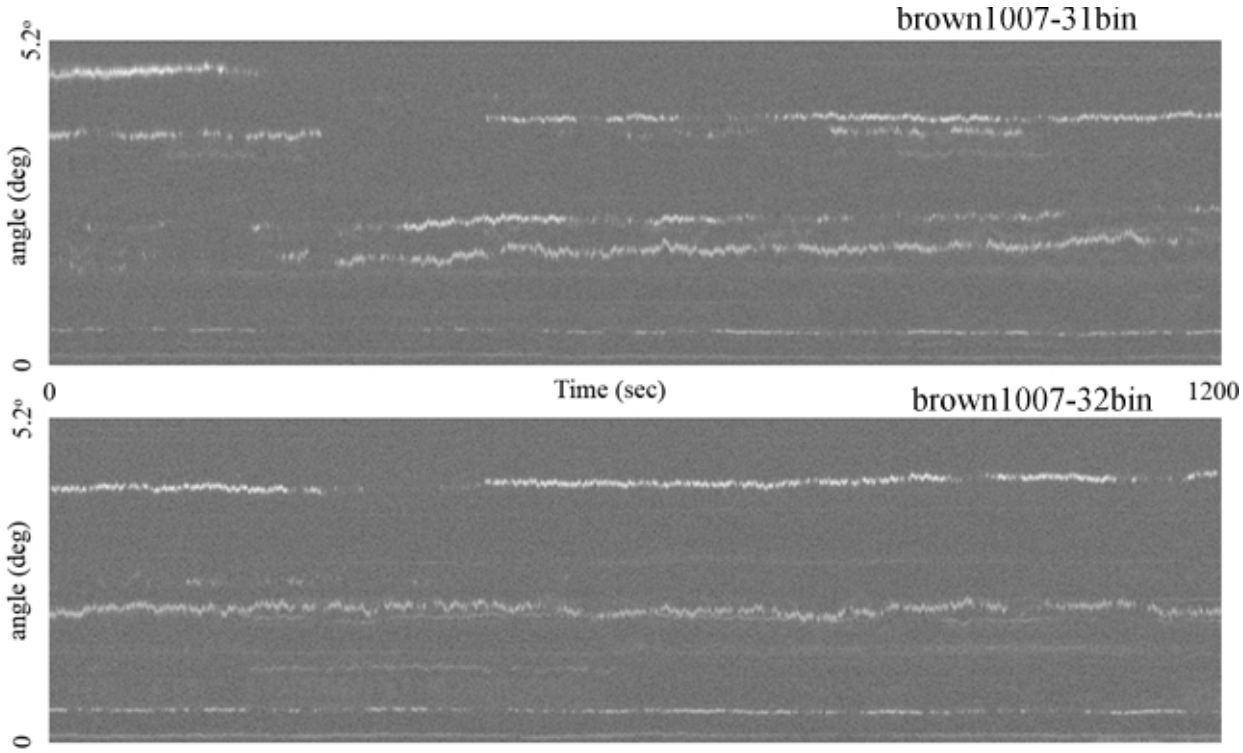

Figure 4.3: Angle vs time random walk behavior in Alumina and Decanoic acid

sensitive to translational motion and although the two are coupled, we assume that equipartition is valid in our system. It has also been seen in previous experiments by Andablo-Reyes [32] that rotational and translational microrheology will yield the same results for the complex shear modulus. Their experiment showed that the $G(\omega)$ of a system of polyacrylamide with optically anisotropic spherical probe particles could be obtained with good agreement for both translational and rotational microrheology.

The Brownian motion behavior in figure 4.2 resembles a one dimensional random walk in both kinetic and full frame mode data. This motion can be identified by the discontinuity of the trajectory which consists of discrete steps in a Bernoulli or 1 dimensional stochastic process. The step sizes depend on the time resolution and are smaller for the kinetic mode data than the full frame data. The rotational step size will also depend on the size of the particle due to the dependence of the MSD on the third power of the particle radius. This can be seen for trajectories with varying step sizes as in figure 4.6. Trajectories with very

large step sizes can be correlated to Bragg diffraction with large but weak Bragg peaks in the raw SPE data which are a product of weakly diffracting particles. These particles are thus much smaller than the majority of particles due to the size inhomogeniety of the alumina powder. The averaged MSD curves only consider particles with similar sizes which can be estimated by the size of the Bragg peak. Particles with similar diffraction sizes may still have different intensities if they do not completely satisfy the diffraction condition and thus it is appropriate to average particles with the same diffraction size but different intensities.

The quickly diffusing particles are particles which have a smooth trajectory for the time that they satisfy the diffraction condition and are in the field of view of the CCD detector. Such particles do not move in discrete angular steps within the resolution of the CCD detector and are typically uni-directional. The trajectories are distinguished from the random walk trajectories by the continuity of the angular motion and cannot be analyzed with viscous or viscoelastic microrheology theory because the motion is not observably stochastic and thus the validity of using the thermal energy at ambient temperature is not known.

The third type of motion is stationary with respect to the specific rotation axis where the angle of the particle does not change in time and is given by a straight line which correlates to a constant orientation over the time of the scan. Such a particle is not determined to be translationally stationary as it can stay in a fixed orientation and stay within the illumination cylinder of the beam and maintain a fixed diffraction intensity and still translate. It is also not known if the particle rotates about the axis parallel to the momentum transfer vector q although equipartion would indicate that it is unlikely that a particle would rotate about one axis and not an alternate axis over a timescale of minutes.

The Brownian random walk data is of most interest because the complex shear modulus which gives the storage and dissipative behavior can be determined from the MSD. Using the analysis technique described in section 3.6, the chosen trajectories of similarly sized particles are isolated and cropped to minimize noise and aid the tracking algorithm, yielding trajectories which are shown in figure 4.4.

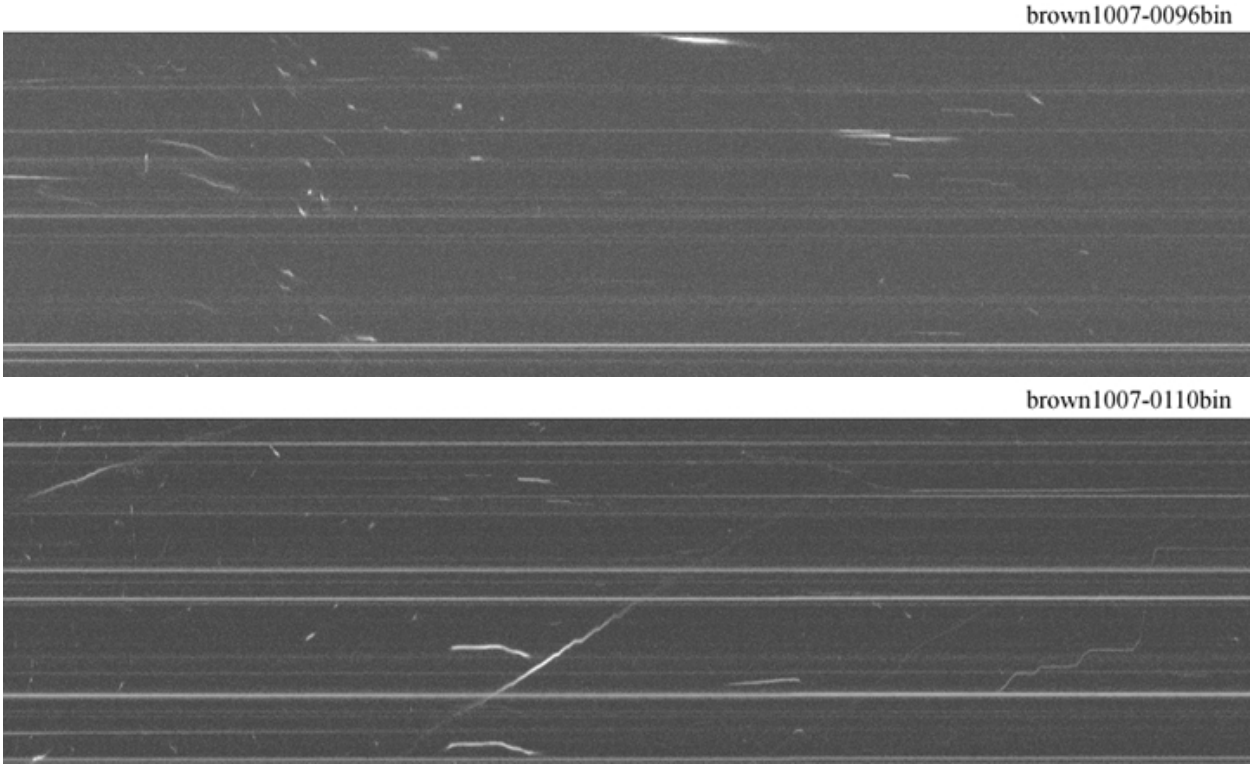

Figure 4.4: Fast diffusion and stationary particles in Alumina and Decanoic acid

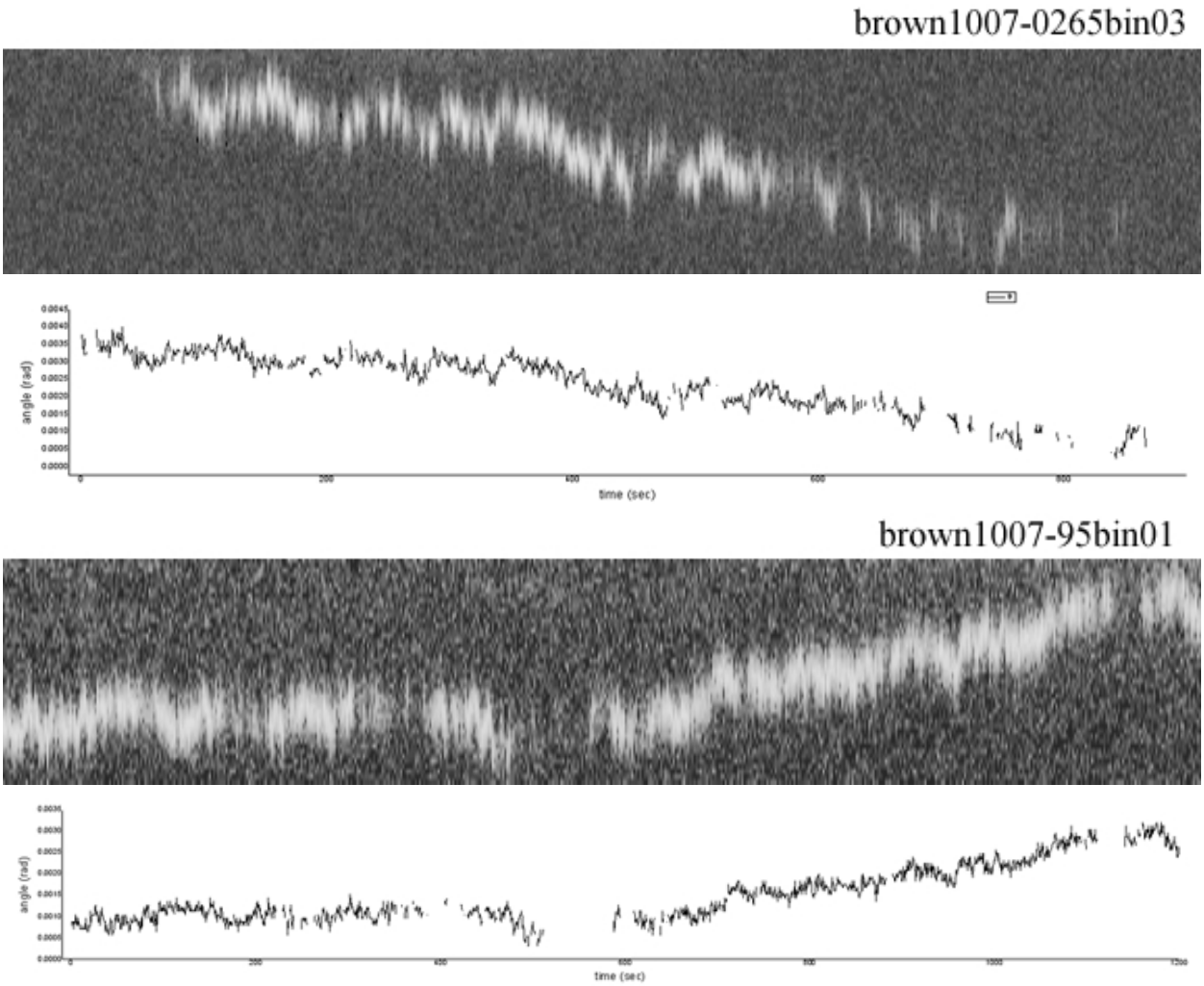

Figure 4.5: Individual trajectories and the tracked data

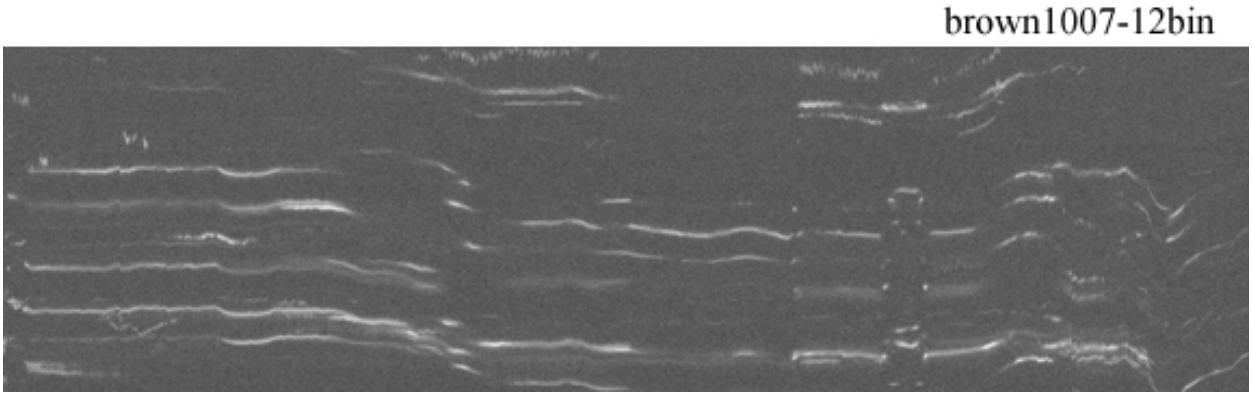

Figure 4.6: 300nm Alumina in Decanoic acid at 31^oC. All particles moving in concert suggests that the convection due to the sample being at the phase transition temperature.

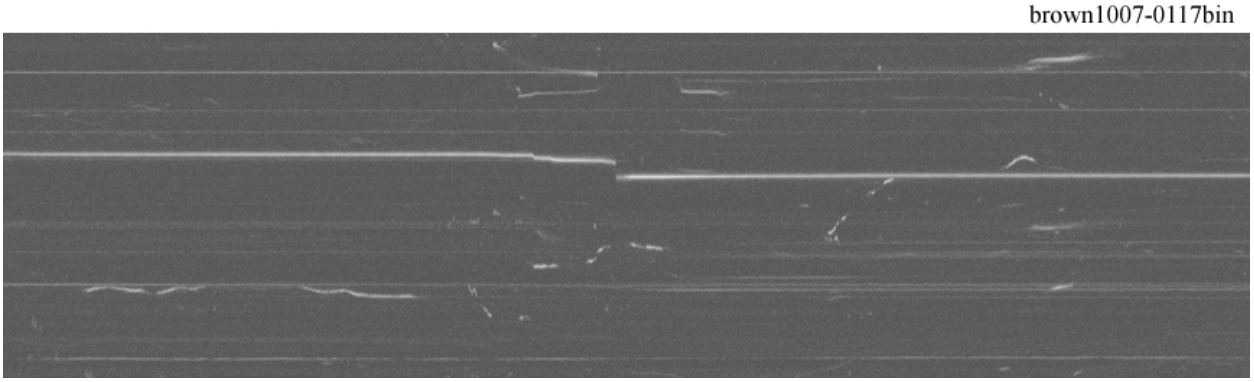

Figure 4.7: 300nm Alumina in Decanoic Acid at 28.1^oC. Abrupt step in motion indicated a collision between particles that causes a rapid change in orientation.

These three types of behaviors: brownian, diffusive, and stationary encompass the vast majority of the particles observed but there are a smattering of exotic behaviors that can be attributed to rare events. Examples of such behaviors are seen below in figure 4.5 and 4.6 and can be attributed to changes in the sample due to the convection caused by heating or statistically rare events such as collisions in a dilute suspension. The observation of the rapid change in orientation due to a collision indicates that in the brownian trajectories which are tracked, there are no collisions which affect the motion of the particles and that the MSD which is calculated is due solely to the energy in the system.

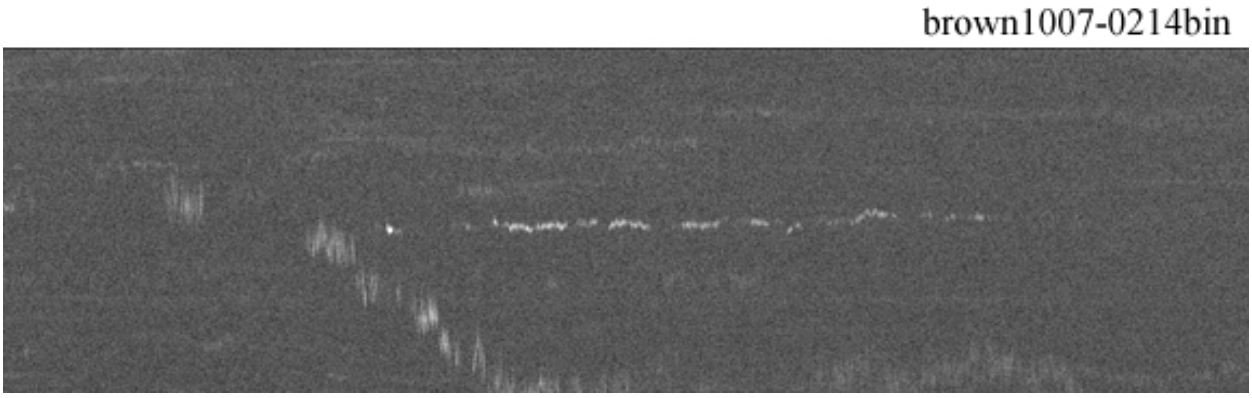

Figure 4.8: 300nm Alumina in Decanoic Acid at 38.4^oC. Example of two particles of different sizes evidenced by the difference in the width and intensity of the diffraction spot. A smaller particle will have a large, less intense diffracted intensity. The two particles thus have different steps sizes even though they both show random walk, Brownian motion

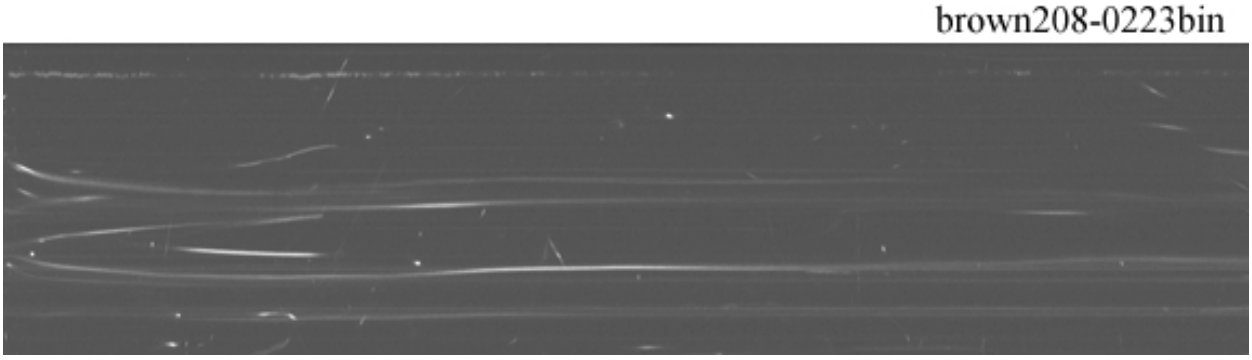

Figure 4.9: 300nm Alumina in Decanoic Acid at 38.4^oC. Slowly moving Alumina particles which are not Brownian in their motion.

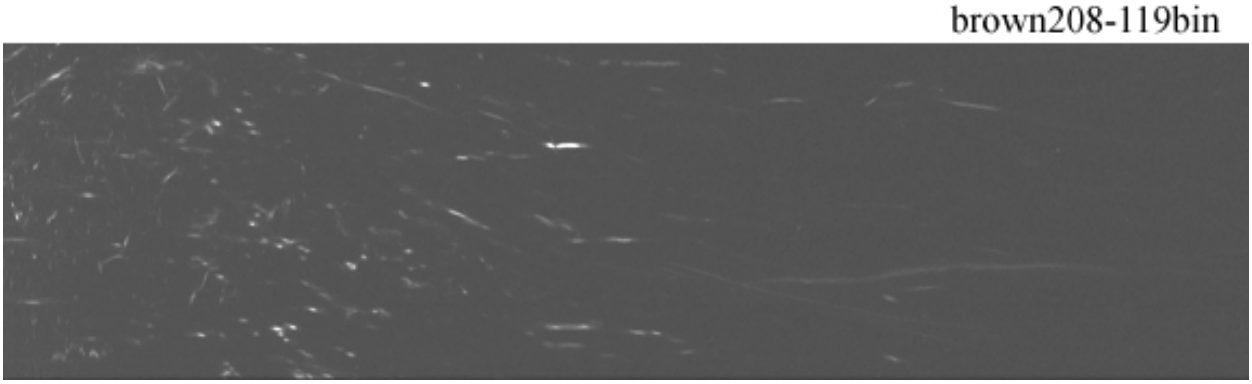

Figure 4.10: 300nm Alumina in Decanoic Acid at 28.1^oC. A common observation is the quick and crowded motion at the beginning of a scan only to have the particles slow in their rotations and become less populous as the scan continues.

4.1 Alumina and Decanoic Acid

The 300nm Alumina and Decanoic Acid sample had the widest variety of behaviors due to the large temperature range acessible because of the glass transition temperature of decanoic acid being conveniently at room temperature. Titanium dioxide particles were an alternate tracer particle candidate, but were not found to be radiation hard and the diffraction patterns grew large and faint with exposure of more than a few seconds, a result of the particles degrading in the beam. The peltier was capable of accessing temperatures from -20^oC to $+50^oC$, though the stability of temperatures at the two extremes was inconsistent. The following are examples of 300nm Alumina and Decanoic acid at various temperatures in the liquid phase. All of the trajectories show brownian type motion and the individual step sizes and angular mobility are not observed to differ greatly between the temperatures.

4.1.1 MSD

The MSD versus time curves for all the trajectories at a given temperature and the averages for the different temperatures are given in figure 4.12. All of the trajectories have the subdiffusive behavior at short times of less than 20-50 sec. This can be seen as a MSD vs time dependence that is not linear or as a slope of less than one on a log-log plot. This

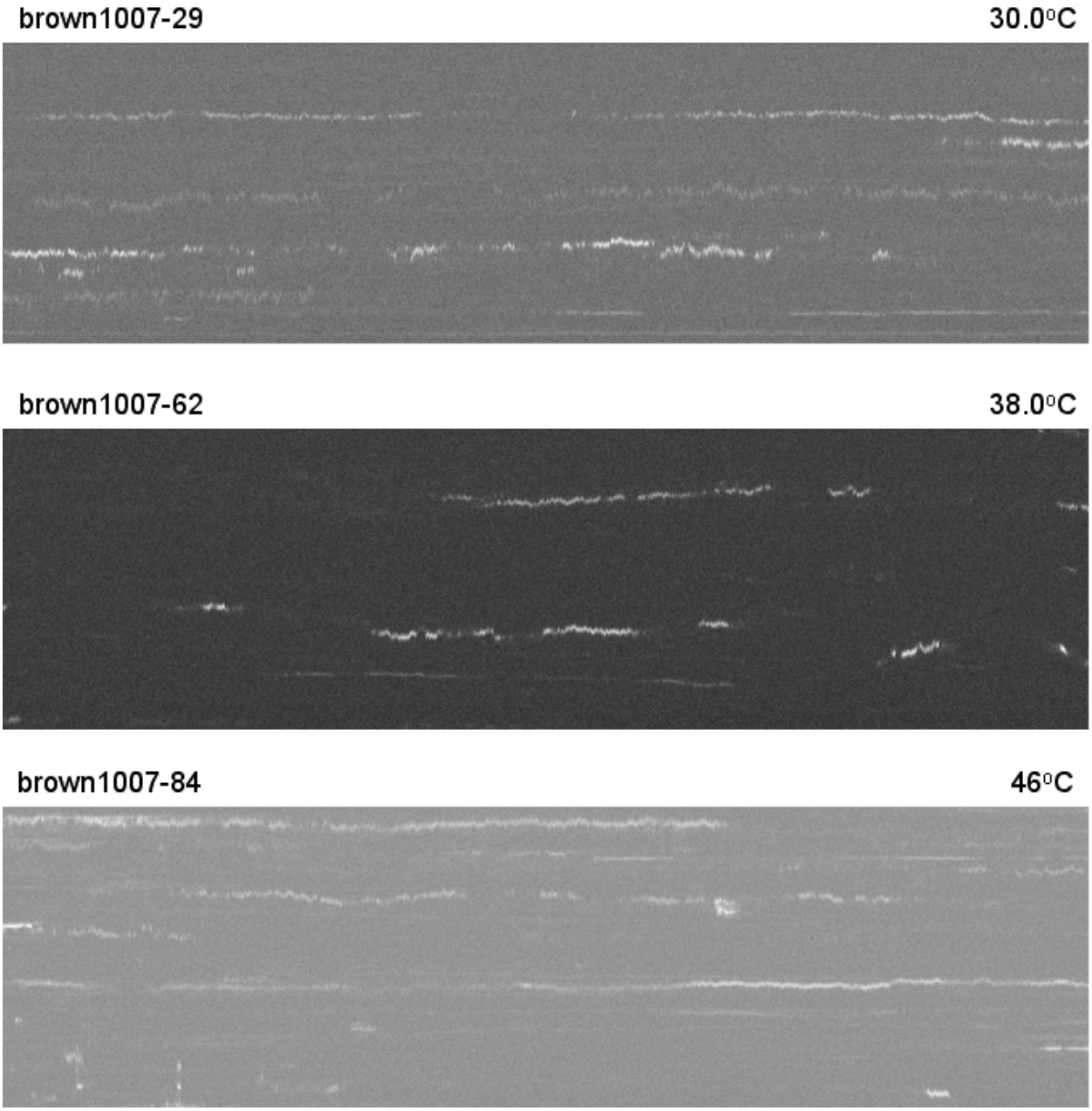

Figure 4.11: Data of 300nm Alumina in Decanoic acids at various temperatures above the glass transition. All the trajectories show Brownian behavior.

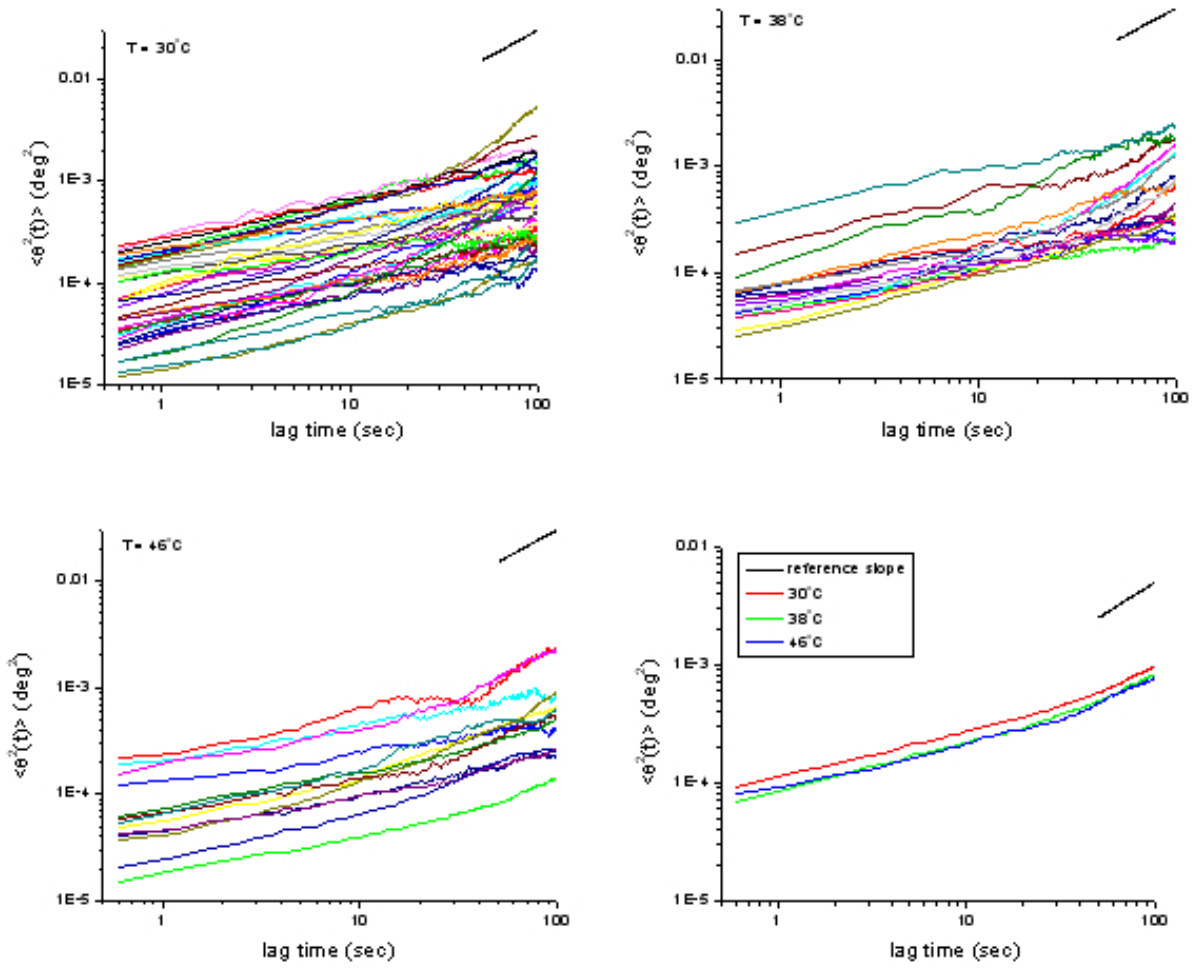

Figure 4.12: MSD versus time curves for particles at three temperatures and the averaged MSD versus time curves for all three temperatures plotted on the same graph.

subdiffusive behavior has an average α value of 0.4 transitioning towards more diffusive but still subdiffusive behavior with an α of 0.79 at longer times. The transition times were found to be between 20-50sec. There is no strong temperature dependence seen between 30^oC and 46^oC for the MSD curves.

The $G(\omega)$ analysis shows that the storage and dissipative modulus are similar for all temperatures across the frequency range and have no strong temperature dependence. The steady state viscosity caluclated from the low frequency limit at $0.05sec^{-1}$is 500cP with an estimated $G''(\omega)$ of $25J/m \cdot sec^3$.

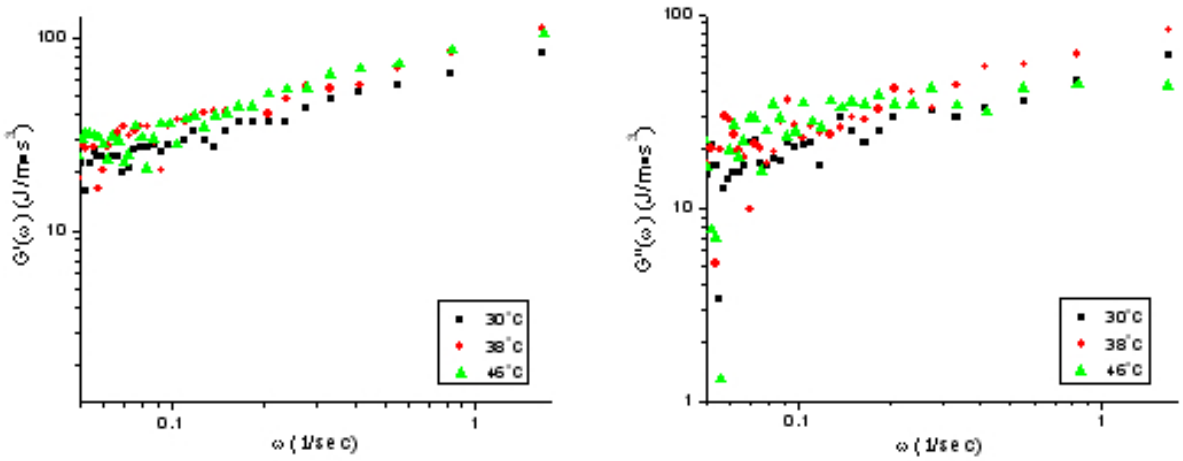

Figure 4.13: The $G'(\omega)$ and $G''(\omega)$ for the averaged MSD vs time curves of the three temperatures.

4.2 Kinematic Mode

Kinematic mode data was also obtained to improve the time resolution of the MSD curves and thus provide a larger range of frequencies. The time delays that were used were 0.02sec and 0.04sec per frame. The trajectories are similar in character to the full frame data except that the step sizes are smaller as expected for a shorter time step. The data is only considered for time lags within a single frame of data which is 40 time steps for the scans taken because the statistics are poor for longer time lags because of the large segments of missing data corresponding to the read out time of a single frame. The MSD vs time results of these scans at 30.6^oC are shown in figure 4.14.

Plotting both time steps on the same graph, we can see that there is good agreeement in the MSD values between the overlap regions of the averaged values and the noise due to insufficient statistics beyond the lag time within a single frame.

The storage and dissipative moduli also show good agreement between the two time steps and gives a steady state viscosity of 500cP for a frequency of $0.02sec^{-1}$ similar to the full frame data.

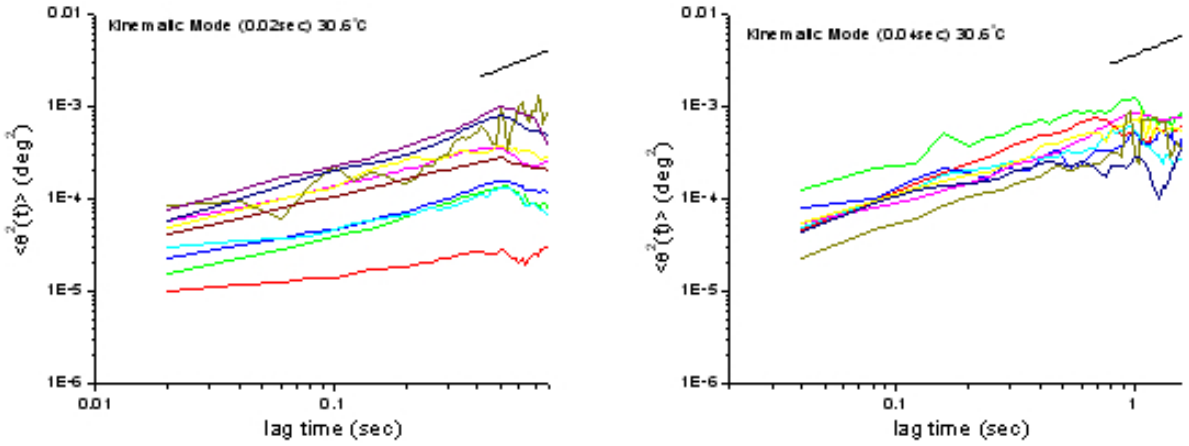

Figure 4.14: All of the MSD vs lag time curves of alumina in decanoic acid at 30^oC.

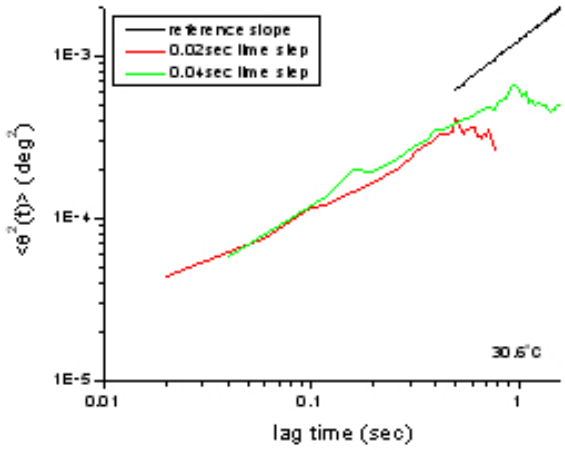

Figure 4.15: Averaged MSD vs lag time curves of alumina in decanoic acid at 30^oC for time steps of 0.02sec and 0.04 sec, showing good agreement in the overlap region.

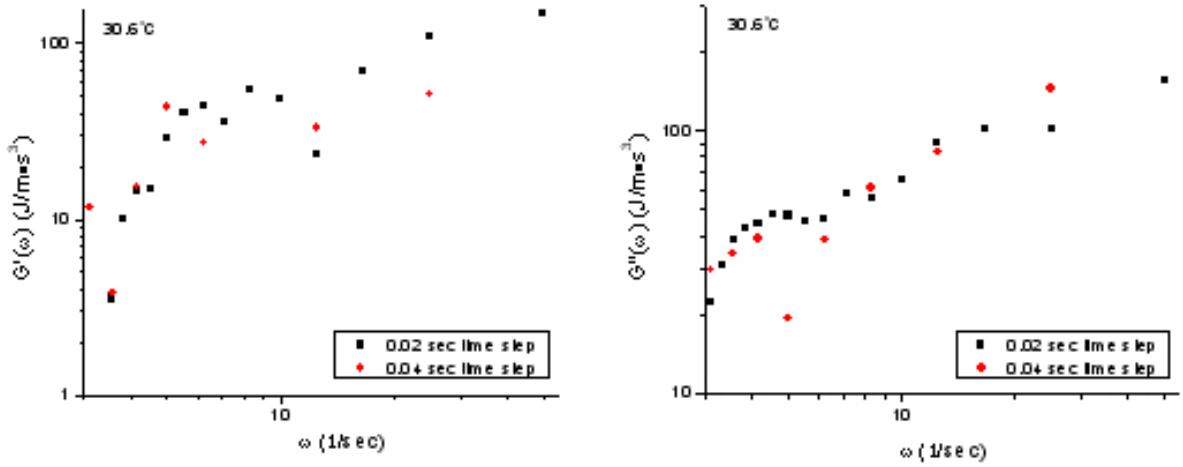

Figure 4.16: The storage and dissipative modulus of alumina in decanoic acid at 30^oC.

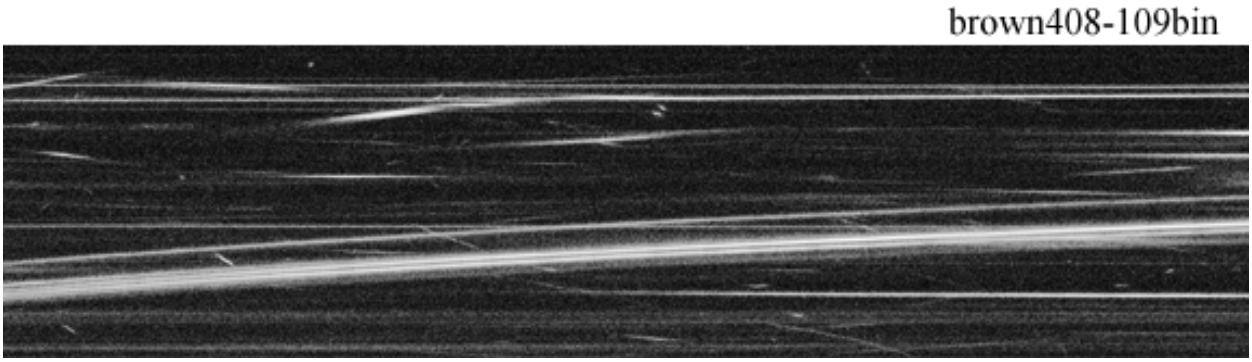

Figure 4.17: 300nm Alumina and Decanoic acid at -15^oC

4.2.1 Solid Phase

The behavior of Alumina in decanoic acid below the glass transition temperature is seen in the following plots. Via an imaging camera above the sample, we can observe the glass transition by the opacity of the sample in addition to knowing the melting point of the decanoic acid (31^oC). There is an abrupt transition between the quickly diffusing behavior in the solid phase to the Brownian, random walk behavior in the liquid phase as the temperature is increased above the glass transition temperature. There is an intermediate phase observed where there is coexistence of the two behaviors.

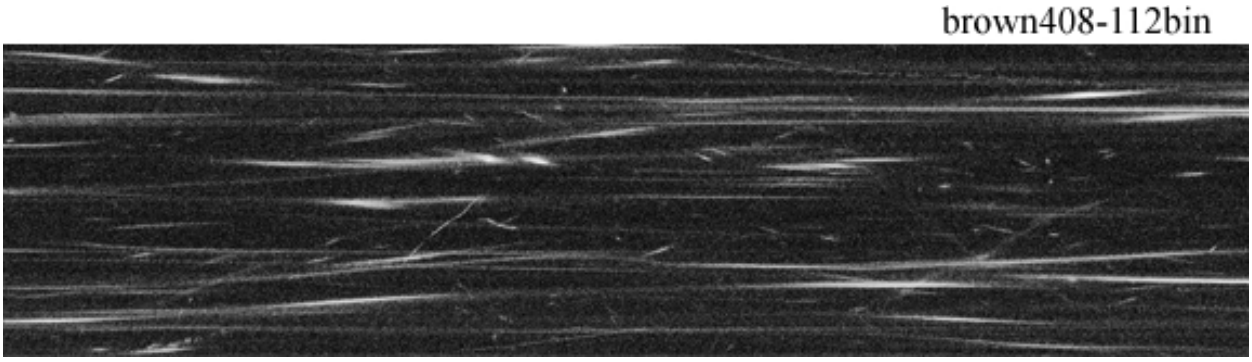

Figure 4.18: 300nm Alumina and Decanoic acid at -7.3^oC

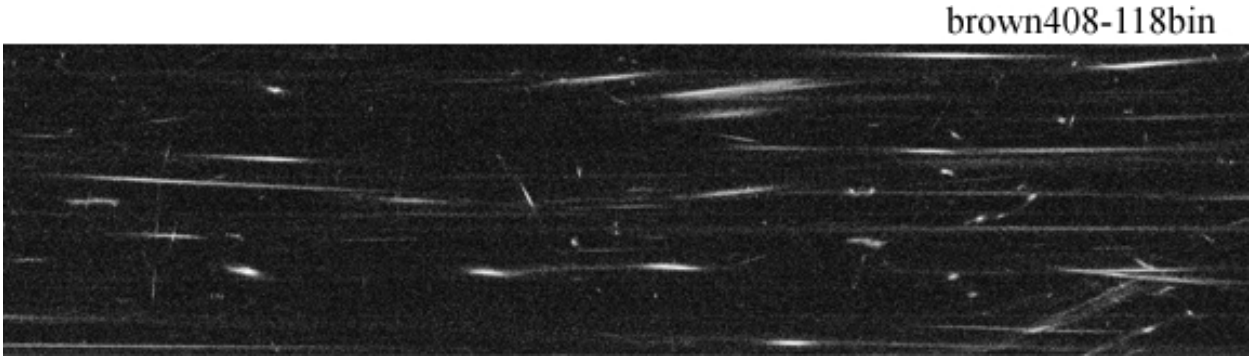

Figure 4.19: 300nm Alumina and Decanoic acid at 3.0^oC

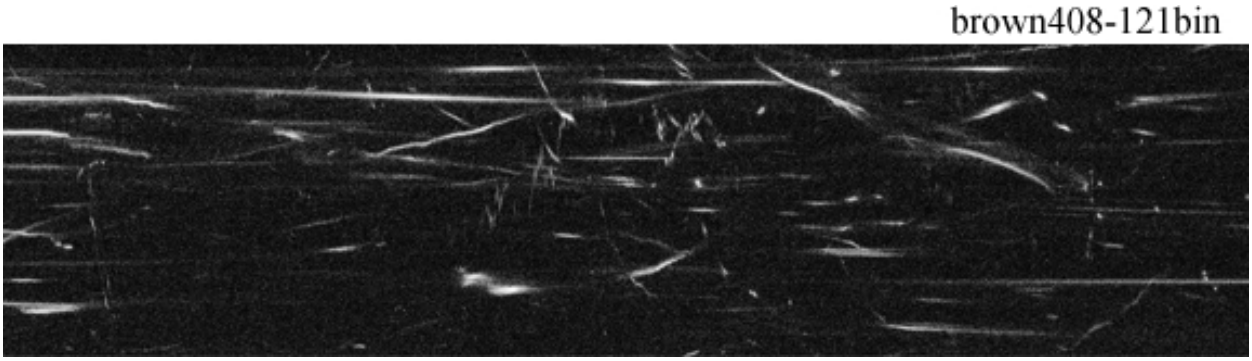

Figure 4.20: 300nm Alumina and Decanoic acid at 12.0^oC

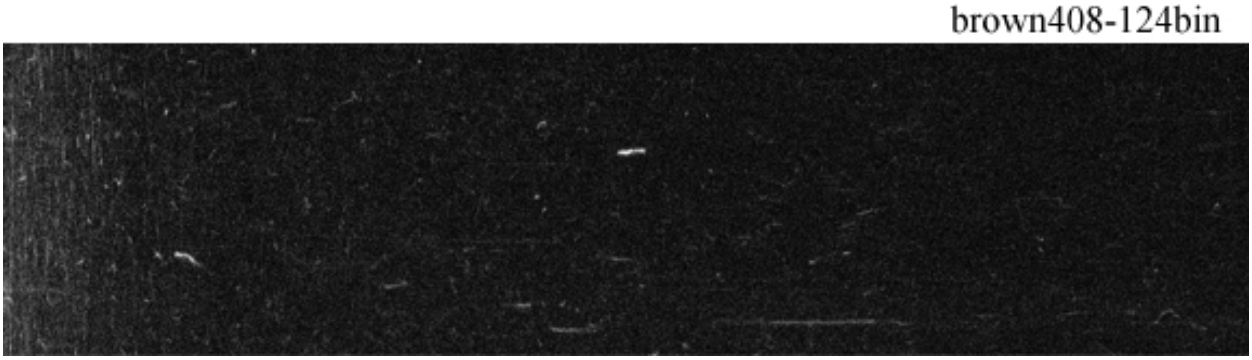

Figure 4.21: 300nm Alumina and Decanoic acid at 25.3^oC

4.3 Alumina and Hydrocarbons

To test the technique of x-ray diffractive microrheology for a different system, we performed preliminary studies on a mixture of alumina and soft paraffin hydrocarbons which are found in petroleum jelly. The results yielded similar trajectories to that of Alumina and fatty acid with sample trajectories and the MSD shown in figures 4.23-4.25 at temperatures above the glass transition temperature of 41.8^oC. At temperatures below the glass transition, the trajectories resemble the diffusive but not brownian motion similar to fatty acids in the solid phase. At higher temperatures in the liquid phase, the trajectories are similar to the random walk trajectories of the liquid fatty acids and can be tracked and analyzed by the same means to determine the storage and loss moduli. The subdiffusive behavior of the alumina-hydrocarbon sample had an α value of 0.344 at short lag times and a diffusive/superdiffusive α of 1.146 at long lag times with a transition time of 5-20 sec.

The temperature dependence of hydrocarbons was studied by analyzing the trajectories taken at various temperatures. These preliminary results did not reveal any strong temperature dependence of the MSD.

The $G'(\omega)$ amd $G''(\omega)$ was also determined and found to result in a steady state viscosity of 1000cP which is 20-4 times literature values of hydrocarbons.

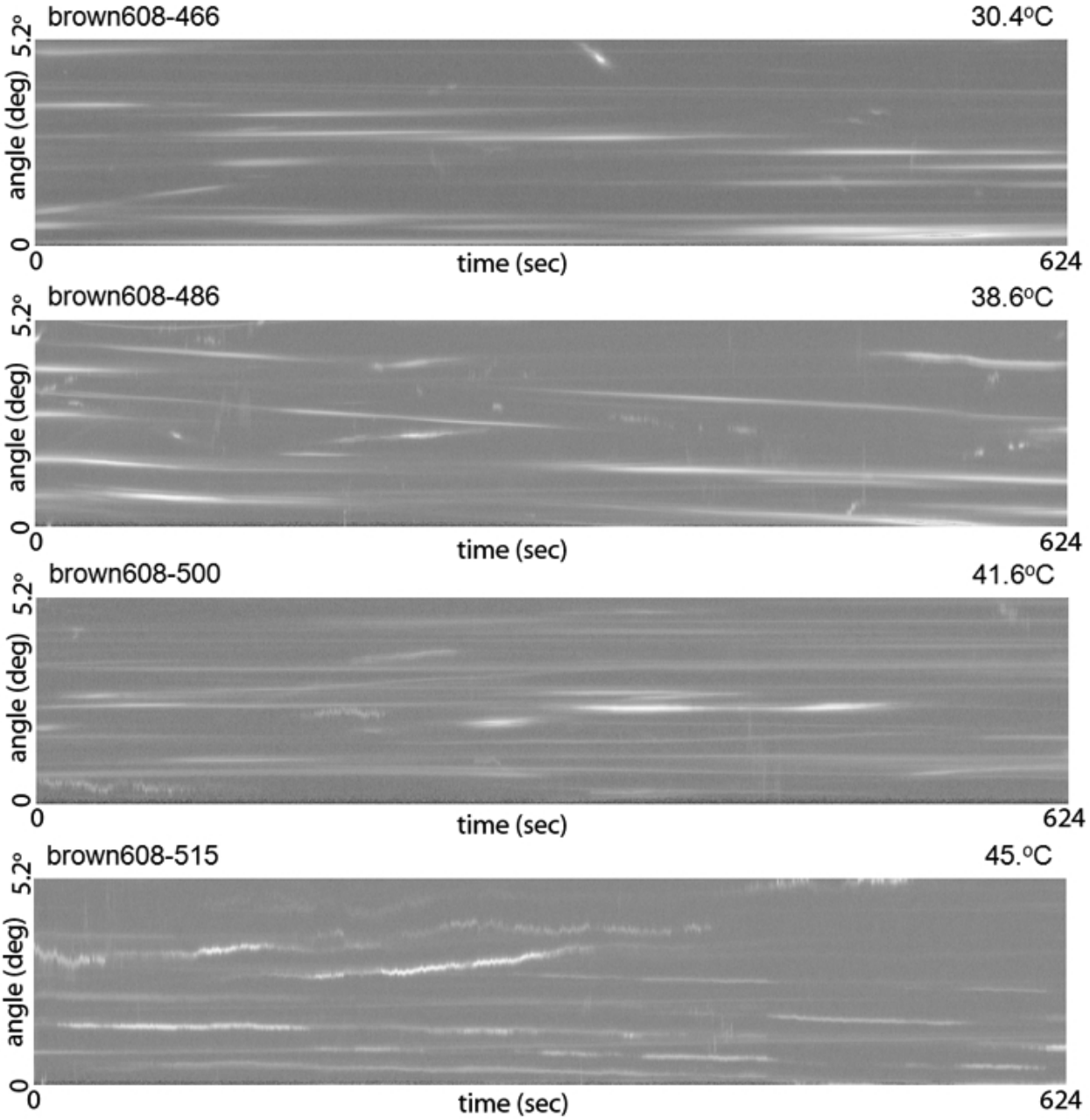

Figure 4.22: Alumina in a solution of hydrocarbons at temperatures below the melting point and slightly above the melting point. At the melting point, brownian type fluctuations begin as can be seen at 45.0^oC

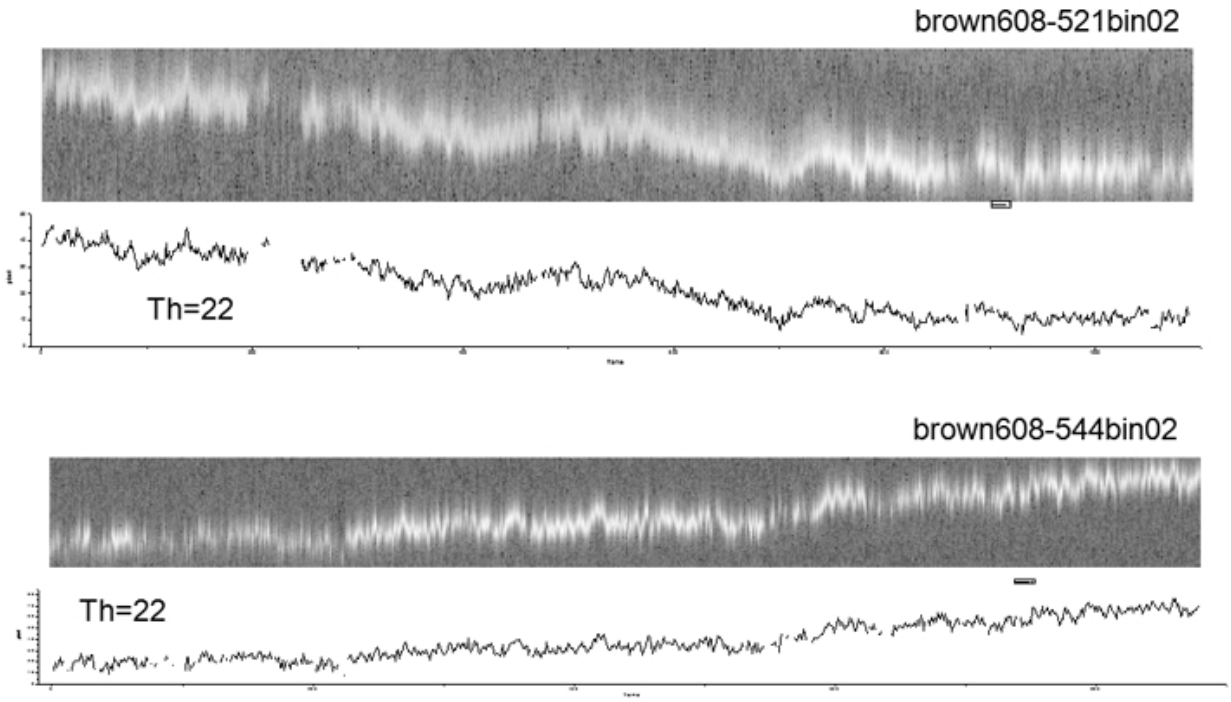

Figure 4.23: Sample trajectories for a mixture of hydrocarbons and alumina at an approximately 8% volume fraction at 50^oC

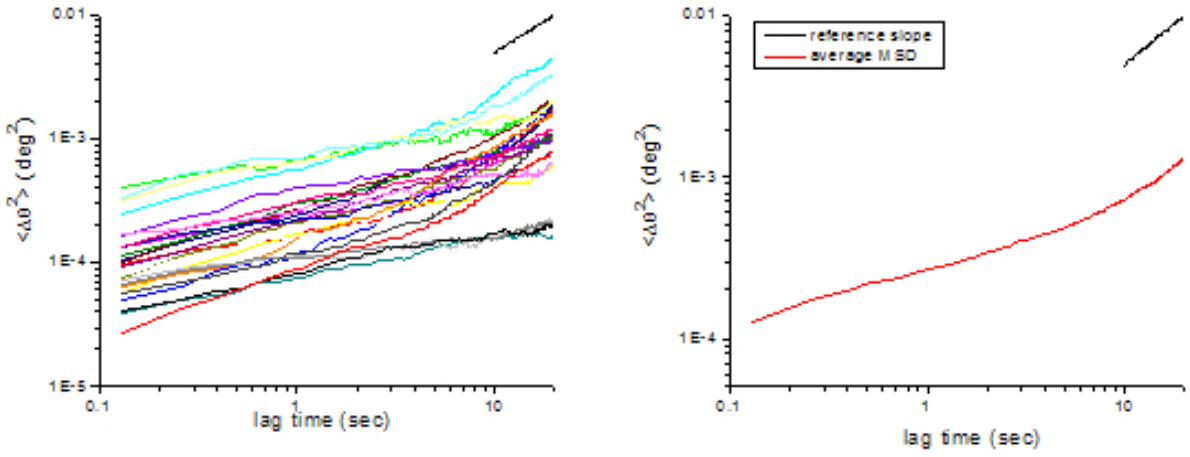

Figure 4.24: The MSD versus time for all the alumina and hydrocarbon trajectories and the average of all the trajectories

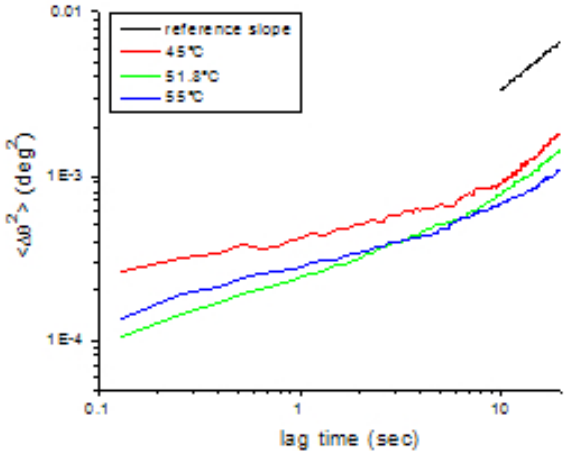

Figure 4.25: temperature dependence of a hydrocarbon and alumina mixture at above the melting temperature of the hydrocarbon

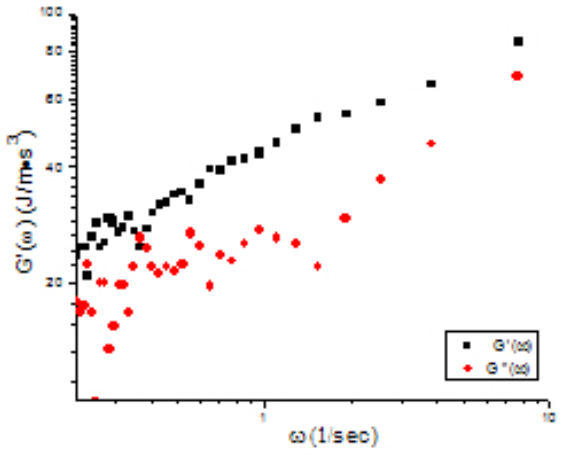

Figure 4.26: The $G'(\omega)$ and $G''(\omega)$ derived from the averaged MSD vs time of a hydrocarbon/decanoic acid solution.

4.4 Radiation Measurements

Radiation effects play a large role in many experiments from damage to heating. Our experiment did not show any changes in the diffraction pattern of the alumina crystals themselves, indicating that no damage was done to the crystals themselves. However, due to the high flux of our focused synchrotron beam and the small sizes of the alumina particles, and that our experiment studies the motion of these tracer crystals, it is important to study the effect of radiation pressure from the incident beam as an external force in addition to the thermal energy which is the only energy that the MSD - $G(\omega)$ considers. To study this effect, we changed the radiation conditions on the particles by attenuating the incident beam or changing the shuttering of the beam.

4.4.1 Attenuation Experiments

Attenuator studies were done by placing a 200micron Al film upstream from the sample, thereby reducing the flux on the sample to 13.5% of the regular beam. In rare instances, the same particle could be studied with and without an attenuator and the radiation effects could be very difinitively determined. Figure 4.27 shows the trajectories of the same particle with and without attenuation.

The MSD of the particles are calculated and plotted in figure 4.28 and show differences in the behavior with the particle illuminated by the attenuated beam showing more subdiffusive behavior than the particle diffracting from the regular beam.

To obtain better statistics, a series of attenuator experiments were done and the average of many particles were taken to see if the trend could be seen for an ensemble of particles. The MSD versus time for all the particles are shown in figure 4.29 and the averages are shown in figure 4.30 for the data taken in full frame mode. The $G(\omega)$ was also calculated and both the storage and dissipative modulus are shown in figure 4.31.

The MSD vs time and $G(\omega)$ graphs for the kinematic mode data with increased time

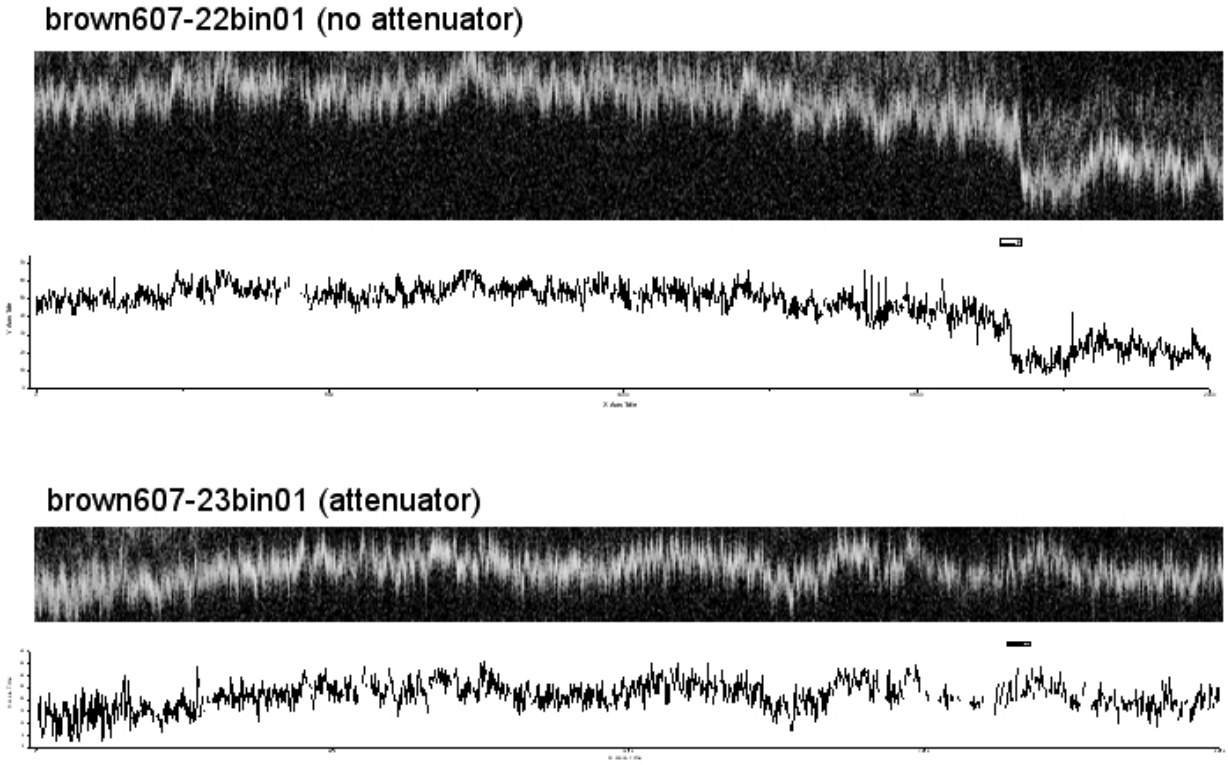

Figure 4.27: Trajectories of the same particle with and without an attenuator upstream of the sample.

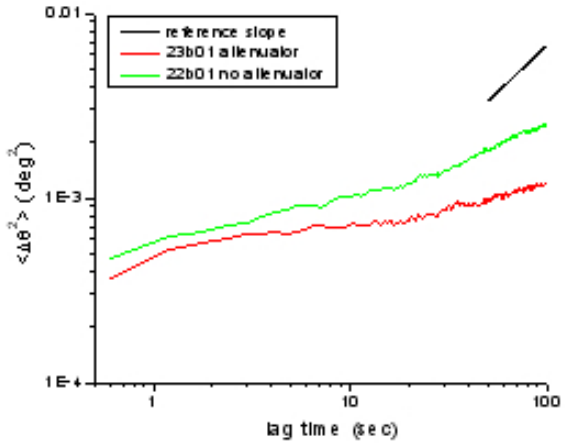

Figure 4.28: The MSD vs time graph for the same particle, with and without attenuation.

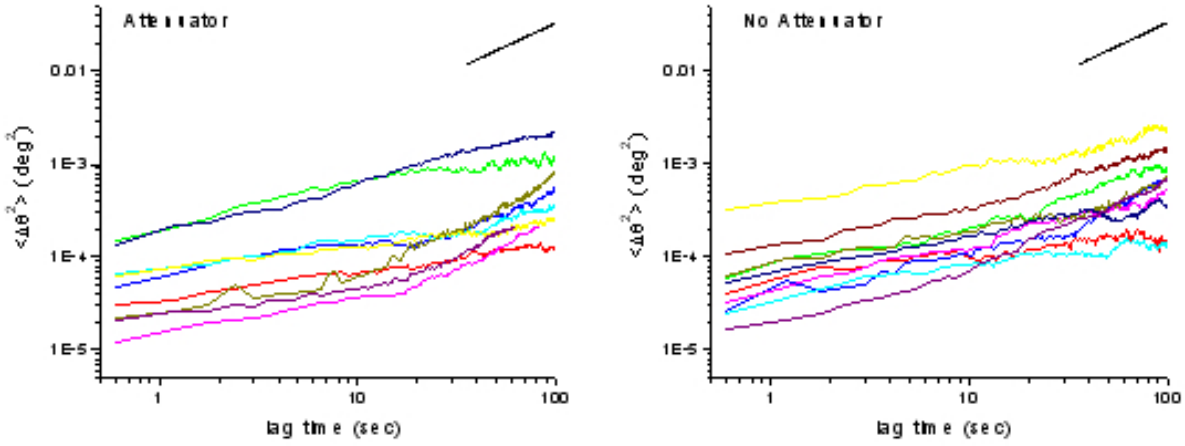

Figure 4.29: The MSD of all of the particles with and without attenuation.

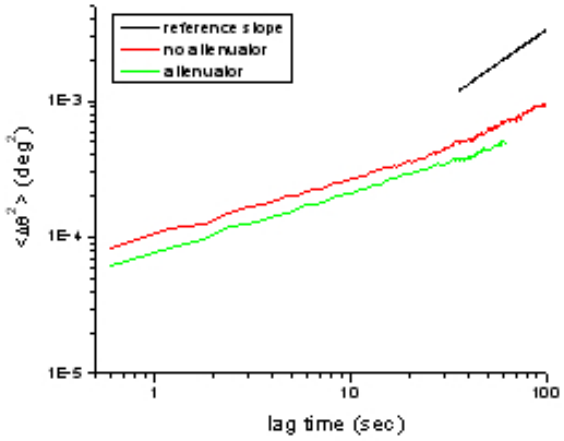

Figure 4.30: The average MSD with and without attenuation

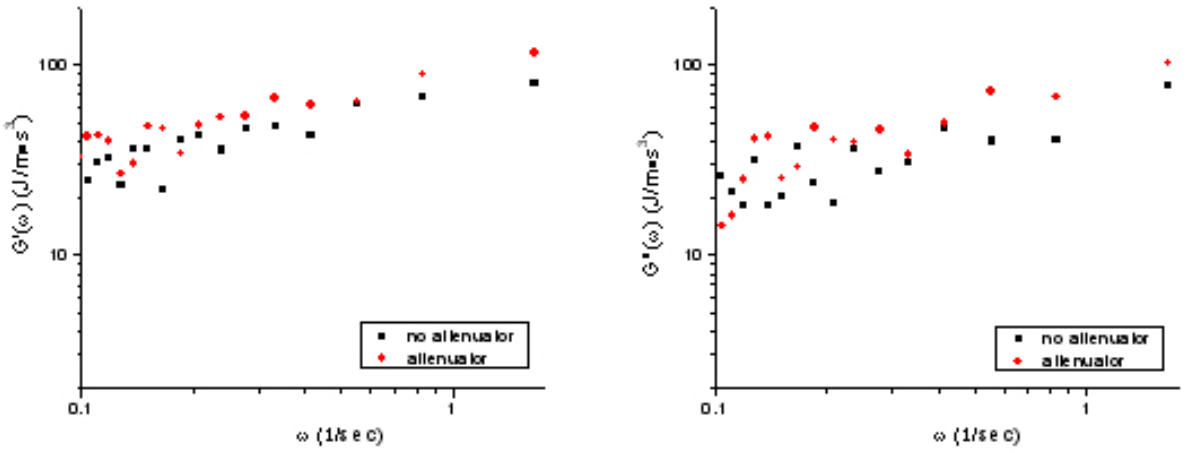

Figure 4.31: The $G'(\omega)$ dissipative and $G''(\omega)$ storage modulus for the averaged MSD with and without attenuation

resolution of 0.04sec are shown below in figures 4.20-4.23 and show a similar difference to the full frame data.

4.4.2 Shuttering Experiments

The effects of radiation can also be studied by changing the shuttering conditions of the incident beam on the sample. Two shuttering modes are possible, one is to shutter the beam incident on the sample and the other is to shutter the scattered beam by closing the an iris directly in front of the CCD. Similar to the attenuator experiments, one can ocassionally study a single particle with the two different shuttering conditions. In the figures below, shuttering refers to shuttering the incident beam. The MSD of the particle with and without shuttering are shown in figure 4.35.

Again, ensemble averages were obtained to improve statistics and the storage and dissipative modulus are calculated and differences are observed between the shuttered and not shuttered trajectories.

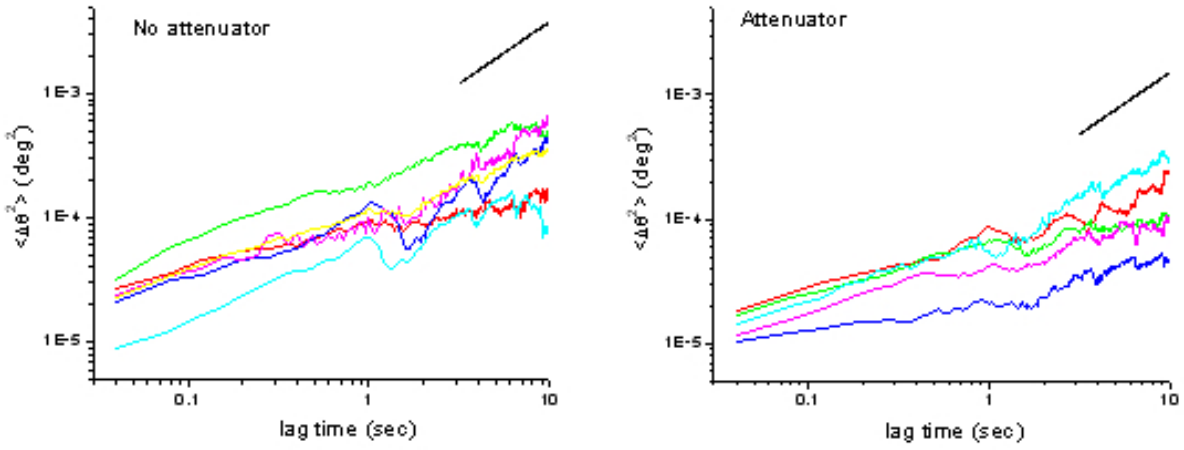

Figure 4.32: The MSD of all of the particles with and without attenuation.

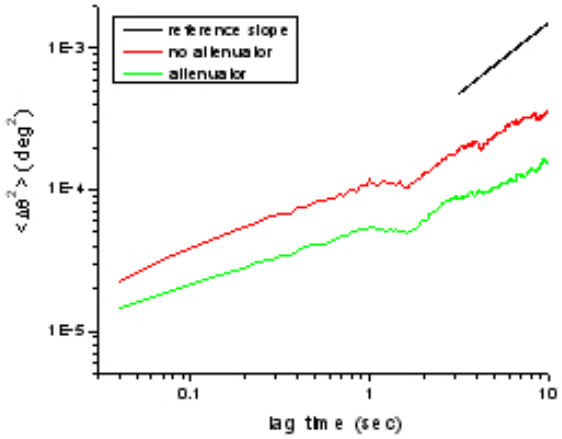

Figure 4.33: The average MSD with and without attenuation

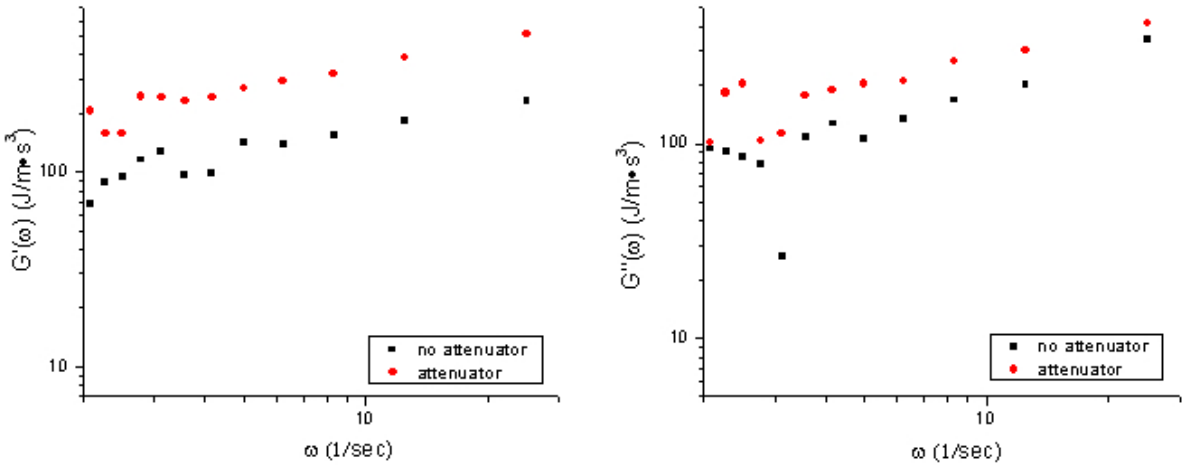

Figure 4.34: The $G'(\omega)$ dissipative and $G''(\omega)$ storage modulus for the averaged MSD with and without attenuation

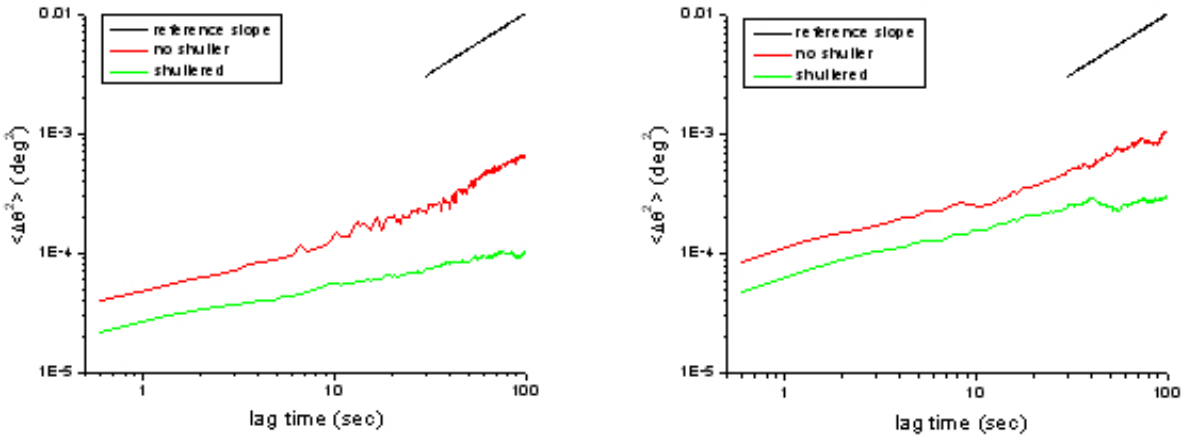

Figure 4.35: The MSD vs time graph for the same particle, shuttering and not shuttering the incident beam.

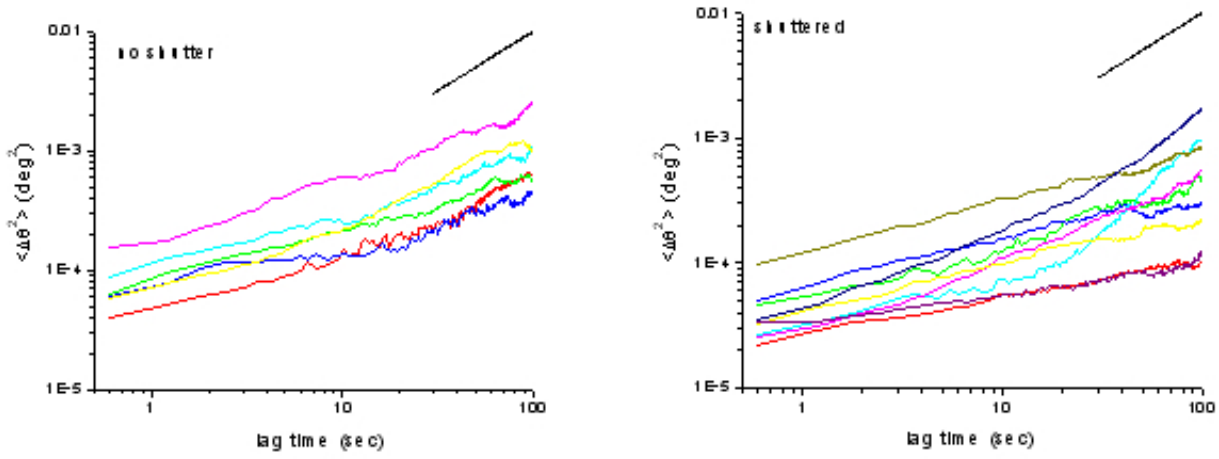

Figure 4.36: The MSD of all of the particles with and without shuttering.

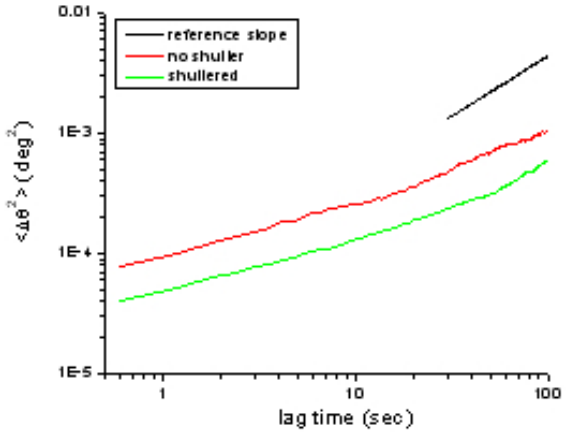

Figure 4.37: The average MSD with and without shuttering

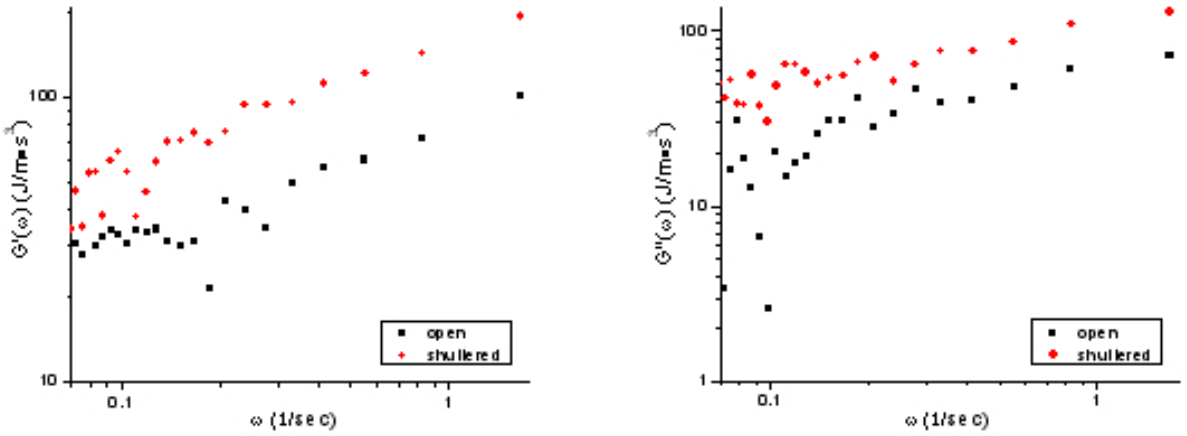

Figure 4.38: The $G'(\omega)$ dissipative and $G''(\omega)$ storage modulus for the averaged MSD with and without shuttering

4.5 Rheology of paints

An unexpected result is the mobility of pigment particles seen in dried paint. Dried paint with single crystal TiO_2 as the white pigment particles were placed in reflection geometry and the diffraction from the titania was observed. The diffraction intensity was found to be mobile even for dried paint no matter the drying time. Acrylic paints were studied after drying times of over 10 hours while oil paints were allowed to dry for over 36 hours.

The paints were then baked in an oven for 45min at 200^oC after the recommended drying time for each type of paint. None of the baked paints showed rotationally mobile pigment particles.

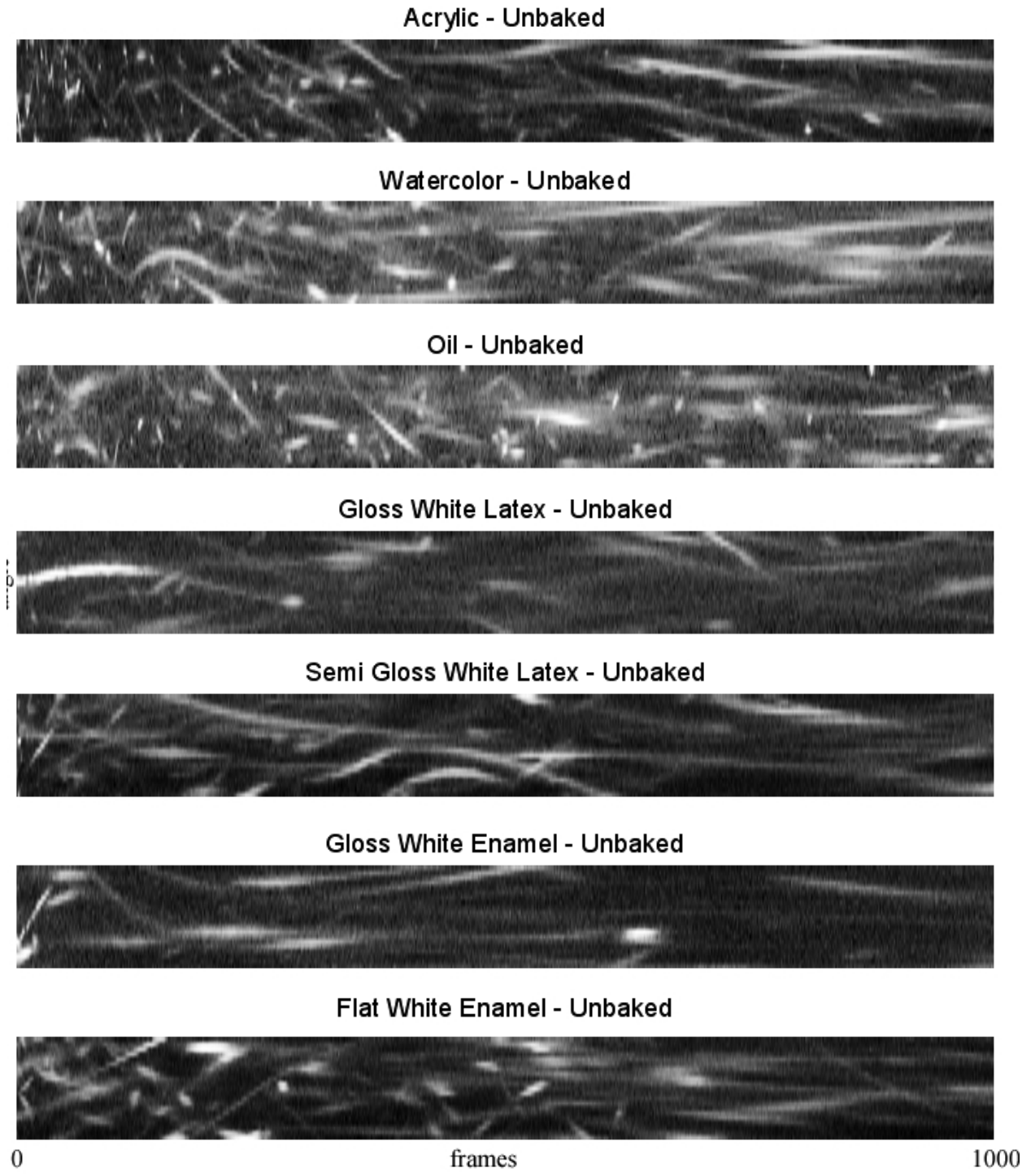

Figure 4.39: Unbaked paints of several varieties all showing mobile pigment particles after drying for over 10 hours

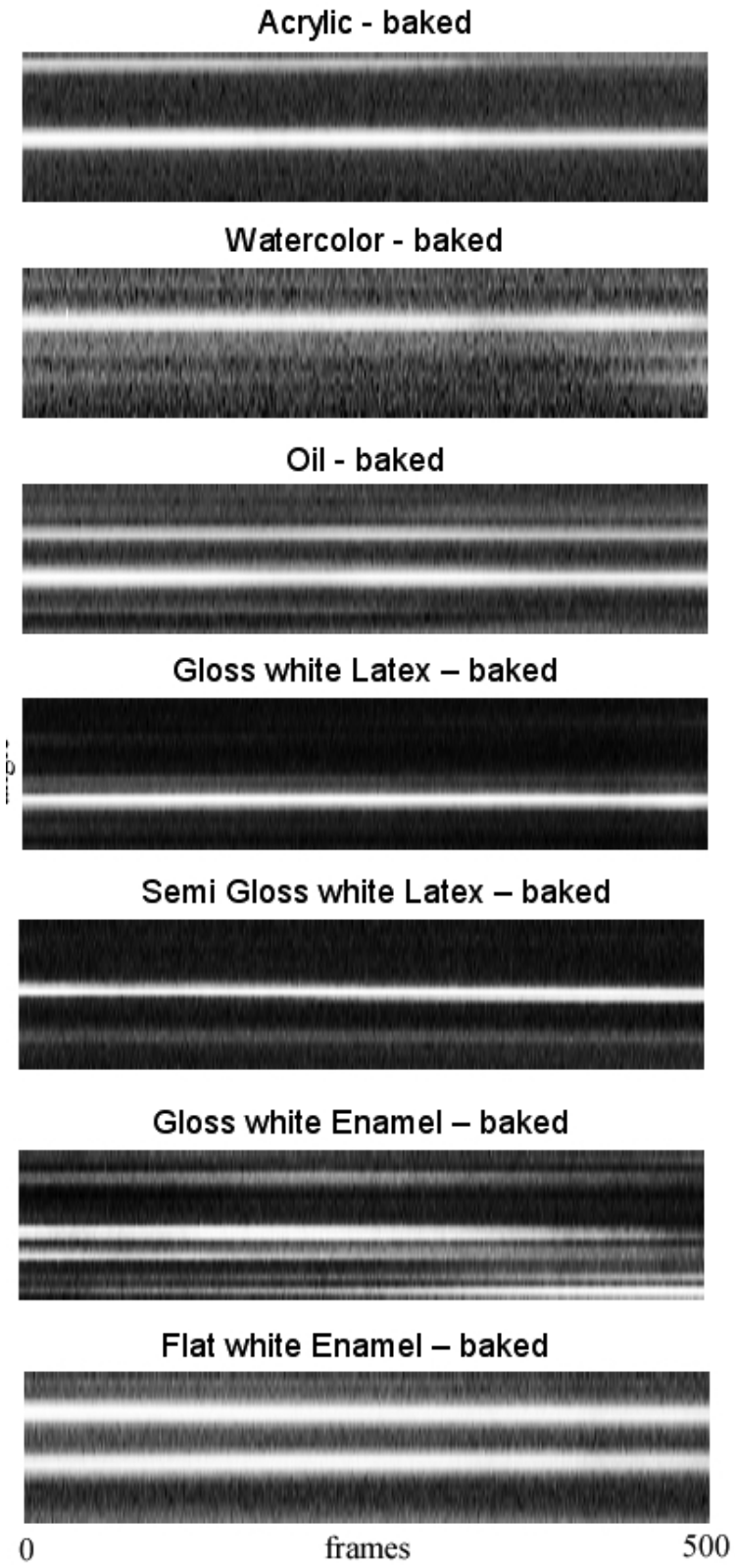

Figure 4.40: Baked paints of several varieties with the motion stopped after baking for 45min at 200^oC.

Chapter 5

Discussion

5.1 MSD and viscosity

For the MSD vs time curves, there is some variation for different particles which produces different values for the complex shear modulus that would be calculated given. This has been previously seen in the work of f-actin by Gardel and Weitz [4] where they looked at the translational motion of particles in glycerol and f-actin networks. They, too, observed variations in the MSD vs time curves for all particles and attributed it to statistical variances and inhomogeniety in their sample. Our sample, in addition to statistics and variations that could be due to a temperature gradient in the sample from the ambient air temperature to the temperature of the peltier, has inhomogeniety in the size and shape distribution of the Alumina. It is thus most accurate to only consider the complex shear modulus of the averaged MSD vs time plots for a single experimental condition.

For the Alumina and fatty acid in the liquid phase at all of the temperatures the long time limit gives the steady state viscosity which can be compared with literature values. The literature value for the Kinematic viscosity is 6.9018cSt for decanoic acid at 40^oC [37] measured by glass capillary kinematic viscometry. Using a density of $0.893gm/cm^3$ for the density of decanoic acid at 40^oC, this gives a dynamic viscosity of 61.6cP. If the low frequency limit ($0.5sec^{-1}$) of the dissipative modulus is estimated to be $25J/m \cdot s^3$, the value we obtain for the steady state viscosity is 500cP, an order of magnitude higher. This limit is defined by the noise of the $G(\omega)$ because at very long times, it there are not enough statistics to obtain an accurate MSD value. This is indicative of an unknown physical effect which is not

yet known about the system.

5.2 Subdiffusive behavior

The transition from subdiffusive with an α of 0.4 to more diffusive with an α of 0.79 can be seen in the change in slope in the log-log plots of MSD vs time and occurs at approximately 20-50sec. This indicates there is an effect which hinders the rotational motion greatly at short times but lessens in affect at longer times. One possibility is a physical rotational caging mechanism where the cages are not stationary but form and break up at the characteristic transition time. The existence of physical cages which have a lifetime of 20-50sec in our system would be analogous to van Zanten's work[33]. In his system, the cages were wormlike micelles caused by the self assembly of CTAB which have a lifetime which corresponds to the transition time between subdiffusive and diffusive behavior.

It is also possible that there are physical cages which are stationary but the coupling mechanism between the alumina particles and the cages has a time scale of 20-50 seconds. Such an mechanism could be the timescale for adsorbtion and desorbtion of the fatty acids on the alumina. The fatty acids which adsorb onto the Alumina may be connected to a cage or network formed by the bulk fatty acid via the coulombic forces which cause self assembly. In this case, the adsorbtion and desorbtion of the fatty acids could be the timescale which govern the rotational mobility which cause the subdiffusive behavior. Self assembly has not been seen in pure fatty acid solutions without additional solvents or salts but a system such as ours with alumina particles as local impurities has not been investigated from a self assembly standpoint. There has been evidence of impurities catalyzing self assembly in system such as DNA[39].

5.3 Temperature dependence in the Liquid Phase

The temperature studies of alumina and decanoic acid in the liquid phase indicate there is no strong temperature dependence in the temperature range studied. This is consistent with the static kinematic viscosity studies which show that the viscosity does not change greatly over that temperature range. The kinematic/dynamic viscosities for decanoic acid at 40^oC are 6.9018cSt/61.6cP and are 5.2488cSt/46.9cP at 50^oC. In addition to no dependence of the steady state viscosity on temperature, there is also an inconclusive dependence of the subdiffusive behavior on temperature. Neither the transition time from subdiffusive to diffusive or the subdiffusive exponent is observed to depend on temperature. This indicates that the caging mechanism of physical cages or coupling between the cages and the adsorbed layer of fatty acid is also temperature independent in this range.

5.4 Effective radius

The adsorbtion of decanoic acid and hydrocarbons onto alumina indicates that the alumina particle has a different effective radius that interacts with the fluid than the physical radius of the particle. This is the radius that should be used to determine the storage, dissipative moduli and fluid viscosity in the MSD analysis but alternatively, this effective radius can also be determined if the viscosity is known for the fluid. In this latter case, assuming the viscosity of the decanoic acid to be 6.9018cSt, the effective radius of the probe particle would be 948nm which means that there is an additional 648nm of effective radius which are attributed to the fatty acid adsorbate layer. For a decanoic chain length of 8 Angstroms, that would indicate that a layer of 800 fatty acid chain lengths is adsorbed onto the surface of an Alumina particle.

Adsorption is a temperature dependent effect with adsorption density increasing with increasing temperature. This would lead to a larger effective radius as a function of temperature. Increased temperature would also cause the viscosity of the liquid to decrease and

the local temperature which controls the thermal driving force to increase. A combination of both these effects, the underestimation of the radius in the $G(\omega)$ calculation would lead to an overestimation of the $G'(\omega)$ and $G''(\omega)$ as well as the steady state viscosity and the underestimation of the local temperature would lead to underestimation of the driving thermal term. The size dependence would have a greater effect on the $G(\omega)$ calculation due to the size to the third power dependence and this may explain why no clear temperature dependence is observed. The adsorbate layer thickness of fatty acids on alumina has not been studied to predict what thickness is appropriate to estimate an effective radius.

5.5 Solid Phase

The motion of particles at temperatures below the glass transition shows that the particles are mobile in the solid phase in a manner different from the random walk motion in the liquid phase. Since the MSD analysis is not applicable due to diffusive nature of the motion where there are not discrete steps, one must interpret the mobility of the particle in some other manner. One method is to qualitatively look at the lifetime of the particle. This lifetime is the period of time that the particle orientation lies within a solid angle given by the size of the detector and the spectral resolution of the monochromater. This solid angle is the 5.2^o in the size of the detector at our sample to detector distance of 0.6m. The spectral resolution of the monochromator is approximately 1eV at 9KeV which corresponds to a powder ring of width 0.145^o. This would correspond to 31 pixels for our experimental setup which is consistent with the appearance of the powder ring.

The temperature series below the glass transition temperature in figures 4.9-4.14 show that the lifetime of the particles increases as the temperature decreases. This would be consistent with the particles having less thermal energy at lower temperatures. This effect supports the theory that the particles are coupled to the liquid above the glass transition temperature but in the solid phase, the particles decouple and are allowed to freely rotate.

At the glass transition temperature, the motion changes abruptly from diffusive to Brownian and there is a condition where we observe both behaviors. There is convection at this transition point where the temperature gradients in the liquid cause movement in sections of the sample causing clusters of particles to move in concert as in Figure 4.6. There is also a combination of diffusive and brownian motion as there are phase separated domains of both solid and liquid. The area illuimated by the beam is large enough to encompass regions of both and hence the observation of trajectories that resemble both the liquid and solid phase behavior.

5.6 Hydrocarbons and Alumina

Alumina tracer particles in Hydrocarbons show much of the same behavior seen in alumina crystals in decanoic acid. In the solid phase, the motion is diffusive while brownian behavior is seen above the glass transition. The liquid phase shows subdiffusive behavior that also seems to transition to diffusive at long times. For the literature values for density and kinematic viscosity, the dynamic viscosity is 55-230cP. The $G(\omega)$ values at low frequencies of $0.2sec^{-1}$ is $20J/m\cdot s^3$ giving a steady state viscosity of 1000cP, again an order of magnitude difference in steady state dynamical viscosity. This dispartity can similarly be explained by an adsorbed layer due to previously seen adsorption on alumina and the order of magnitude again corresponds to approximately 648nm of adsorbed hydrocarbon. A 30 carbon chain length hydrocarbon of length 24Åwould give 270 layers of adsorbed hydrocarbon.

Unlike the fatty acid solution, hydrocarbons are seen to transition from subdiffusive behavior ($\alpha = 0.344$) to purely diffusive or even superdiffusive ($\alpha = 1.146$) at long times with a shorter transition time than the fatty acids. While the fatty acids, even at long times, still show some sign of rotational caging, the hydrocarbons are completely diffusive at long lag times. Also, the characteristic time of these dynamics, be they desorbtion or the breaking up of physical cages, is on a shorter timescale.

5.7 Radiation Pressure

One important factor due to the large flux of the source and the small size of the particle is the effect of radiation pressure on the motion of the alumina. The radiation pressure of a reflective surface is twice that of an absorbing media and the particle is assumed to be a highly reflective surface with the radiation pressure given by

$$P_{rad} = \frac{2n_p\hbar\omega}{c} \tag{5.1}$$

Previous studies [Sasaki APL] have determined that the radiation pressure on a 50nm gold particle with unfocused white beam synchrotron radiation at SPRING 8 to be of order $10^{-15}N$. Their studies experimentally determined this pressure by finding the constant drift velocity of a gold nanoparticle attached to a protein using a similar particle tracking / MSD analysis as our experiment.

Our focused monochromatic beam has the same order of magnitude photon flux as the corresponding unfocused white beam at SPRING-8. Our particles are an order of magnitude larger with a lower atomic number indicating less scattering and thus less radiation pressure per unit volume if considering that scattering is from the electrons in a material. We therefore conclude that our particles experience comparable radiation forces to Sasaki's gold particles. The forces are of the same order as gravitational forces on the particle and should affect the particles mainly in translation. Any effect on the rotation is due to a gradient in beam intensity which would cause a torque on the particle. There is a Gaussian beam profile in the focused beam which, if assumed to be a standard normal distribution with a fwhm of 2 microns would cause a difference of radiative insensity of 10% across a 300nm particle. For forces determined from Sasaki's experiments, this would give a torque of $3^(- 22)N \cdot m$ for the alumina tracer particles.

Radiation pressure effects on the particles were experimentally investigated by attenuation and shuttering the x-ray beam with results shown in figures 4.28-4.38. A 200um Al

attenuator was used to decrease the flux to 13.5% of its original value. The differences in the MSD vs time values of the attenuated and unattenuated beam indicate that the radiation of the beam increases the mobility of the particle. This can be due to radiation pressure given more kinetic energy of the particle itself. It can also be due to local heating of the sample in the vicinity of the particle which would increase local temperature of the liquid and thus the thermal energy which is the driving force of the brownian motion.

Shuttering experiments were also performed where the camera is shuttered instead of the incident beam providing a constant illumination source or a periodic illumination condition which corresponds to the shuttering rate of the scan. There is also a difference in the total radiation dose on the sample because time that the shutter is closed during readout, especially in the full frame data, can be a significant portion of the total scan time. For the full frame data, the readout is dependent on the orientation of the CCD. If the camera is oriented with the readout direction along the x, the readout time is 0.03sec, if the CCD is oriented with the readout direction along the y, the readout time is 0.5sec. Thus the shuttered sample gets 23% less illumination in the former case and 83% less illumination in the latter.

5.8 Paints

The results of seeing mobile behavior in the pigment particle of dried paints is similarly unexpected. There are two possibilities for the motion, one that it is radiation caused and is a side effect of the imaging technique, similar to charging from the electron beam in a Scanning Electron Microscope. The other is that the particles are suspended in a manner such that the thermal energy is enough to cause rotational motion. In the former case, the mobility of the particles may be explained by an insulating surfactant layer which does not evaporate as the paint dries. Radiation can cause the charging of insulators due to the production of free radicals in a material. If a TiO_2 particle were encased in such a charged

surfactant layer, coulombic forces could cause the mobility which is seen since the motion does not appear to be a stocastic processes which would be caused by random thermally driven forces. It is also possible that the titanium dioxide itself is charging but a previous experiment with silver nanocubes which are conductive and would thus not charge showed a similar effect. Similar behavior was seen in silver nanocubes which were coated with a PMMA surfactant layer used in their synthesis. Deposition of the silver nanocubes onto a substrate and allowing them to dry evaporatively still resulted in seeing motion in the Bragg diffraction from the crystals.

When the paints are baked at 200^oC for 45 min, the particles are found to be stationary. Yet again the silver nanocube sample also showed a similar effect. If the motion is due to a surfactant layer, the change after heating is likely due to the decomposition of the surfactant at high temperatures. In the case of silver nanocubes, where there was a regular shape which could be studied with coherent x-ray diffraction imaging, a stationary diffraction pattern was also correlated with a change in the coherent diffraction pattern of the nanocyrstal, indicating that heating had melted the crystal. Titanium dioxide particles have a very high melting point, 1870^oC of TiO_2 but have been seen to decrystallize in the focuses synchrotron beam from the broadening and weakening of the diffraction intensity. This change of the Bragg intensity was not seen in the paint pigments, however, and is thus more likely due to the decomposition of a surfactant layer. Due to the complex makeup of paints, it is difficult to pinpoint the constituent which may be the cause of the motion.

Chapter 6

Conclusions and Future Work

6.1 Summary

In conclusion, we have performed rotational microrheology using X-ray diffraction by observing the rotational motion of nanocrystals in a variety of materials via tracking the diffracted intensity of crystals in Bragg diffraction. In doing so, we have extended the viscosity range accessible to passive microrheology by taking advantage of the inverse size to third power dependence for rational motion. X-ray diffraction from tracer crystals is a technique which is sensitive to the orientation of an isotropic particle because the crystal planes provide a inherent orientational marker. X-ray diffraction from synchrotron sources also have the advantage of imaging smaller particles than optical microscopy because of the high flux of 3rd generation sources which further increases the viscosity range of liquids which may be studied.

The bahaviors of tracer particles were observed to take on many forms, from the stochastic behavior of thermally driven Brownian motion to fast diffusion which has no observable discrete rotational steps within the resolution of the detector. The rotational motion is observed by suspending tracer crystals of Al_2O_3 in decanoic acid and a mixture of hydrocarbons. A focused x-ray beam is incident on a droplet of this mixture in transmission geometry, illuminating particles in a volume of the focused beam size multiplied by the diameter of the droplet. A CCD detector records the position of diffracted intensity around the powder ring as a function of time, giving a one dimensional rotational trajectory which can be tracked and analyzed to obtain information about the fluid, such as the viscosity and the storage

and dissipative behavior of viscoelastic fluids.

For a system of decanoic acid and 300nm alumina nanocrystals in the dilute limit, both types of motion were observed. Alumina in liquid decanoic acid showed brownian behavior with trajectories which could be tracked to determine the MSD versus time dependence. The MSD versus time graphs show subdiffusive behavior which may indicate a rotational caging mechanism at times less than 30sec, transitioning to purely diffusive behavior at longer times. If caging is the cause of the subdiffusive behavior the short time caging can be attributed to physical cages with a lifetime that correlates to the subdiffusive-diffusive transition or stationary cages which couple and decouple to the bulk with that characteristic timescale.

From the MSD curves, the storage and dissipative modulus were found using passive rheology theory and a steady state viscosity was extracted to compare with literature values. The calculated values were determined to be an order of magnitude larger than literature values with an α of 0.4 at short times and 0.79 at long lag times with the transition time being between 20-50sec. Being that fatty acids have been seen to adsorb onto the surface of almina nanoparticles, this difference in calculated viscosity could mean that the effective size of the alumina particle which is used to probe the liquid is larger than the diameter of particle. It would require multilayer adsorption of 800 fatty acid chain lengths to account for this effective size disparity.

Decanoic acid in the solid phase was also studied and the results were unexpected in that there was motion seen in the solid phase. The motion was of a diffusive nature instead of the brownian random walk nature and the rotational mobiity as qualitatively determined by the length of time that a crystal stayed in diffraction over the angular range of the detector. The trend of the mobility on temperature indicates that the motion is at minimum partly determined by the thermal energy of the system. Because the motion is rotational and not translational, the voids created by the alumina acting as an impurity do not hinder the rotational motion. If the adsorbed layer of fatty acid were to decouple from the bulk,

the particle would then be free to rotate unhindered, driven only by the ambient thermal energy. Because the translational motion is confined, however, it would be important to study whether the rotational motion takes a larger fraction of the thermal energy of the system.

Similar results were seen in the hydrocarbon and alumina sample, brownian motion above the glass transition and diffusive motion in the solid phase. The alumina again showed subdiffusive behavior with an α of 0.344 at short lag times and 1.146 at long lag times, indicating that the motion changes from subdiffusive to diffusive or even superdiffusive with a transition time between 5-20sec. The storage and dissipative components were again determined and found to yield a steady state viscosity value an order of magnitude larger than the literature value for the dynamical viscosity. Because hydrocarbons have also been seen to adsorb onto alumina, a larger effective radius may also be the cause of this difference.

Radiation studies were performed to quantify the effect that the radiation pressure or heating had on the motion of the alumina crystals. It was found that for both attenuation and shuttering experiments, the MSD and $G(\omega)$ calculations found less subdiffusive behavior for the unattenuated/unshuttered trajectories than the attenuated/shuttered leading to a lower storage and dissipative modulous and thus a lower steady state viscosity value. This effect may be explained by radiation pressure which has been observed in previous systems or because of local radiation heating in the fluid.

The final study was on commercially obtained paints to determine the rotational mobility of titanium dioxide pigment particles. Surprising, the crystals were found to be mobile even when the paint was dried according to standard application instruction. The motion was diffusive and found to stop once the paint was baked at 200^oC for 45 min. The motion may be due to coulombic forces due to charging of a surfactant layer in the x-ray beam or due to a solvent which does not evaporate at ambient temperatures which provides a liquid like environment for the particle to rotate in. It may also have a similar explanation to the motion found in the solid phase of both fatty acids and hydrocarbons.

6.2 Future Work

The use of X-ray Diffraction Rotational Microrheology to study viscoelastic fluids has shown much promise, especially in the high viscosity limit. In order for it to become a reliable technique, the deviations from steady state viscosity values must be explained. To this end, the adsorbate layer thickness of fatty acids and hydrocarbons on alumina must be determined to determine the exact role that the different in particle size and effective size plays in the calculation of the storage and dissipative moduli and in turn, the steady state viscosity. The exact nature of local heating which both decreases the viscosity of the liquid due to viscosity - temperature dependence, increases the thermal driving force in the particle, and increases the adsorbate layer thickness must also be determined. Previous studies indicate that the radiation pressure due to a synchrotron beam does not greatly affect the motion of a small crystal of comparable size but our studies indicate that there is an effect. Whether this effect is due to heating or pressure should be investigated further.

The technique of rotational microrheology using x-ray diffraction is most suitable for high viscosity liquids that cannot currently be studied using passive microrheology due to the lower limit of observable particle sizes and the difficulty of observing rotations of tracer particles with good resolution. High viscosity polymers are a material of interest that would be accessible to our technique but is beyond the viscosity range of current passive microrheology.

Also of interest are particles with voids or microstructure which may hinder the translational motion of tracer particles. For these systems, there is both a bulk and local viscosity. The viscosity is determined, in the former case, by particles which diffuse across the walls defining the microstructure, and in the latter case, particles which diffuse only within a single pore. Rotational microrheology is a useful tool for determining the local viscosity, especially for materials where the pore size is small and a particle would not be likely to translate without exploring neighboring cells.

The solid phase behavior is of interest because rotational motion across the glass transition has not been studied. The abrupt change in the nature of the rotational behavior across this phase transition, from a stochastic driving force to one that is more continuous needs further investigation. The existence of rotational motion of particles in the solid phase should be studied in other systems and over a larger range temperatures below the glass transition. Of particular interest is the question of equipartition and whether translational confinement impacts the rotational energy of a particle. This can only be studied by simltaneously observing the transational and rotational motions of tracer particles which may be accomplished by concurrent imaging with confocal microscope or suitable light microscope for a transparent glass.

The application of X-ray Diffraction rotational microrheology to paints alludes to the applicability of this technique to commercial as well as research areas. Commercial grade titanium dioxide can be easily imaged with x-ray diffraction and is a component of numerous products such as cosmetics, plastics, paper, food, medical products and many others. Characterization of the rheological properties of many immediately applicable materials is thus possible with this technique.

References

[1] J.D. Ferry, *Viscoelastic Properties of Polymers* (Wiley, New York 1980)

[2] P.M. Chaikin and T. Lubensky, *Principles of Condensed Matter Physics* (Cambridge University Press, Cambridge 1995)

[3] T.G. Mason and D.A. Weitz, Phys. Rev. Lett. **74**, 1250 (1995)

[4] M.L. Gardel, M.T. Valentine and D.A. Weitz *Microrheology*

[5] W.M. Gelbart and A. Ben-Shaul, J. Phys. Chem. **100**, 13169 (1996)

[6] T.G. Mason, K. Ganesan, J.H. van Zanten, D Wirtz, and S.C. Kuo, Phys. Rev. Lett. **79**, 3282 (1997)

[7] N.G. McCrum, C.P. Buckley, C.B. Bucknall, *Principles of Polymer Engineering* (Oxford University Press, New York 1988)

[8] B.J. Berne and R. Pecora, *Dynamic Light Scattering with Applications to Chemistry, Biology, and Physics*, (Wiley, New York 1976)

[9] J. McConnell, *Rotational Brownian Motion and Dielectric Theory*, (Academic Press, New York 1980)

[10] J.A. Dantzig, C.L. Tucker, *Modeling in Materials Processing* (Cambridge University Press, Cambridge 2001)

[11] O. Reynolds, Phil Trans Royal Soc London **177**, 157 (1886)

[12] E.N. da Andrade Phil. Mag. **17**, 497 (1934)

[13] M.L. Williams, R.F. Landel, and J.D. Ferry, Journal of the American Chemical Society, **77**, 3701 (1955).

[14] G. Maret and P.E. Wolf, Z. Phys. B **65**, 409 (1987)

[15] D.J. Pine, D.A. Weitz, P.M. Chaiken, and E Herbolzheimer, Phys. Rev. Lett. **60** 1134 (1988)

[16] D.J. Pine, D.A. Weitz, J.X. Zhu, and E Herbolzheimer, J. Phys. (Paris) **51**, 2101 (1990)

[17] C.J. Behrend, J.N. Anker, and R. Kopelman, Appl. Phys. Lett. **84**, 154 (2004)

[18] Z. Cheng, P.M. Chaiken, T.G. Mason, Phys. Rev. Lett. **89**, 108303 (2002)

[19] Z. Cheng, T.G. Mason, Phys. Rev. Lett. **90**, 018304 (2003)

[20] Y.C. Sasaki, Y. Suzuki, N. Yagi, S. Adachi, M. Ishibashi, H. Suda, K. Toyota, M. Yanagihara, Phys. Rev. E **62**, 3843 (2000)

[21] Y.C. Sasaki, Y. Okumura, S. Adachi, H. Suda, Y. Taniguchi and N. Yagi, Phys. Rev. Lett. **87**, 248102 (2001)

[22] D. Weihs, T.G. Mason, and M.A. Teitell, Phys. of Fluids, **19**, 103102 (2007)

[23] D. Sayre, Imaging Processes and Coherence in Physics, Springer Lecture Notes in Physics Vol 112 (Springer-Verlag, Berlin, 1980)

[24] R.W. Gerchberg and W.O. Saxton, Optik (Stuttgart) **35**, 237-246 (1972)

[25] J.R. Fienup, Applied Optics **21**, 2758-2369 (1982)

[26] J. Miao, P. Charalambous, J. Kirz, and D. Sayre, Nature (London) **400**, 342-344 (1999)

[27] I. K. Robinson, I. A. Vartanyants, G. J. Williams, M. A. Pfeifer and J. A. Pitney, Physical Review Letters **87**, 195505 (2001)

[28] H-J Youn, J. W. Jang, I-T Kim, and K.S. Hong, J. Colloid Interface Sci., **211**, 110 (1999)

[29] N.S. Bell, M.E. Schendel, and M. Piech, J. Colloid Interface Sci., **287**, 94 (2005)

[30] K.I. Slovetskaya, Russian Chemical Bulletin, **49**, 1369 (2000)

[31] Y-Z Li, X.L. Deng, and W.L. Yu, Chinese Science Bulletin **43**, 125 (1998)

[32] E. Andablo-Reyes, P. Diaz-Leyva, and J. L. Arauz-Lara, Phys. Rev. Lett. **94**, 106001 (2005)

[33] J.H. van Zanten and K.P. Rufener, Phys. Rev. E, **62**, 5389 (2000)

[34] M.T. Valentine, P.D. Kaplan, D. Thota, J.C. Crocker, T. Gisler, R.K. Prud'homme, M. Beck and D.A. Weitz, Phys. Rev. E **64** 061506 (2001)

[35] N.W. Ashcroft, and N.D. Mermin *Solid State Physics* (Thomson Learning, 1976)

[36] B.E. Warren *X-ray Diffraction* (Dover Publications, New York 1969)

[37] D. Valeri and A.J.A. Meirelles, JAOCS **74**, 10 (1997)

[38] T.H. Gouw, J.C. Vlugter, and C.J.A. Roelands, JAOCS **43**, 433 (1966)

[39] R. Lambourne, *Paint and surface coatings - theory and practice* (Halsted Press, New York 1987)

[40] C.-Y. Lee, H.E. Canavan, L.J. Gamble, and D.G Castner, Langmuir **21**, 5134 (2005)

[41] M. Wisniewska, J. American Ceramic Soc. **90**, 3608 (2007)

[42] T.J. Hu, J. Gao, and C. Wu, J. Phys. Chem. B **106** 9815 (2002)